Politecnico di Milano

SCHOOL OF INDUSTRIAL AND INFORMATION ENGINEERING

Master of Science – Chemical Engineering

Microgravity droplet pyrolysis of asphaltenes

Relatore

Prof. Alessio FRASSOLDATI

Co-Relatore

Prof. Tiziano FARAVELLI

Candidate

Sirio Adonai Damiano BRUNIALTI – 920667

Academic Year 2019 – 2020

Ringraziamenti

Vorrei dedicare l’inizio di questo trattato alle persone che con il loro supporto mi hanno concesso di concludere il mio percorso di studi.

Innanzitutto, ringrazio il professor Frassoldati e il professor Faravelli che non solo mi hanno concesso di svolgere questo lavoro di tesi ma sono anche stati un’immensa fonte di ispirazione e conoscenza. Il loro supporto mi ha concesso di crescere sia personalmente che professionalmente.

Ringrazio Paolo Guida per l’importantissimo supporto tecnico e per essere stato un prezioso consigliere in scelte professionali.

Dedico un ringraziamento anche al professor Mani Sarathy che ha supportato lo svolgimento di questo lavoro e mi ha aperto grandi porte per il futuro.

Tutti i miei sforzi sarebbero stati vani se non fosse per l’enorme supporto morale fornitomi dalla mia famiglia e dai i miei amici. Di questi vorrei in particolare ringraziare i miei genitori Paola e Orlando e i miei compagni di viaggio Elia, Davide, Stefano e Mauro.

Sommario

Preoccupazioni riguardanti l'inquinamento e il surriscaldamento globale stanno spingendo i principali paesi sviluppati ad aumentare l'uso di fonti di energia rinnovabili a scapito dei combustibili fossili. Ciò nonostante, oggi il petrolio continua ad essere la fonte principale nel mercato energetico globale e continuerà a rimanere una risorsa essenziale per l'economia mondiale ancora per decenni. Le riserve di greggio leggero sono state le prime ad essere sfruttate e con il tempo si stanno lentamente esaurendo. Per questo motivo il petrolio sta diventando sempre più pesante e questo andamento continuerà nel futuro. Uno degli effetti di questo fenomeno è l'aumento di disponibilità di frazioni pesanti, ottenute come sottoprodotto della separazione delle frazioni più leggere e pregiate, come benzina e gasolio. Queste frazioni pesanti vengono introdotte nel mercato sotto forma di miscele chiamate Heavy Fuel Oils (HFO), tipicamente utilizzate come combustibili in impianti di produzione di energia elettrica, fornaci e per il trasporto marittimo. Gli HFO sono disponibili in grandi quantità ed economici, rendendoli adatti per utilizzi industriali. D'altro canto, la elevata viscosità, bassa volatilità, l'elevato contenuto di zolfo e azoto e il loro basso rapporto H/C comportano serie difficoltà nell'ottenere una combustione pulita di questi carburanti; elevate produzioni di SO_X e NO_X accompagnate da problemi di sporcamento sono tipici di apparecchiature che impiegano oli combustibili pesanti. Preoccupazioni riguardanti l'inquinamento dovuto all'impiego di HFO stanno sorgendo, un esempio può essere visto nella decisione dell'Organizzazione Marittima Internazionale (IMO) di ridurre il limite massimo di quantitativo di zolfo nei combustibili ad uso marittimo dal 3.5% in peso allo 0.5% in peso a partire dal 2020. In molte applicazioni passare all'uso di combustibili più leggeri non è economicamente sostenibile a causa del maggiore costo a parità di energia, inoltre ciò comporterebbe ad un surplus di HFO. Per queste ragioni lo sviluppo di nuove tecnologie per l'upgrade e combustione pulita di HFO stanno diventando di sempre maggior interesse. A questo scopo è necessario avere una buona comprensione dei comportamenti ad alta temperatura di questi composti. Ad oggi poco si sa riguardo i fenomeni di combustione di questi idrocarburi e solo recentemente sono stati fatti sforzi per descrivere la pirolisi in fase liquida. Nel lavoro qui presentato uno schema cinetico

semplificato è stato implementato in un modello monodimensionale di goccia in microgravità per la simulazione di pirolisi di gocce isolate. Si è deciso di investigare il comportamento ad alta temperatura di gocce perché gli oli pesanti vengono bruciati o gassificati tramite l'utilizzo di spray, quindi una buona conoscenza dei fenomeni legati alla goccia è di grande utilità per la lo sviluppo di futuri modelli per la simulazione di apparecchiature. I componenti degli oli combustibili pesanti possono essere separati in quattro frazioni diverse in funzione della loro polarità: i saturi, gli aromatici le resine e gli asfalteni. Queste sono anche chiamate le frazioni SARA. Nel modello cinetico adottato ognuna delle frazioni SARA dell' HFO viene rappresentata con una miscela di pseudo composti, poi una reazione lumped semplificata viene definita per descrivere la pirolisi in fase liquida di ognuno dei pseudo composti. Questo lavoro si è concentrato esclusivamente sulla frazione asfaltenica degli HFO in quanto è la causa principale della formazione di inquinanti e residuo carbonioso. Il primo passo di questo lavoro è lo sviluppo di una metodologia per la predizione delle proprietà termofisiche delle specie coinvolte, difatti i surrogati degli asfalteni sono specie complesse delle quali non si hanno valori sperimentali delle proprietà. A questo scopo un insieme di metodi di contributo di gruppo e di correlazioni per la predizione di proprietà di idrocarburi pesanti è stato selezionato, e tali correlazioni sono state arrangiate in modo tale da ottenere un sistema che è in grado di restituire tutte le proprietà necessarie richiedendo la sola conoscenza della struttura molecolare dello pseudo composto. I valori ottenuti da questo metodo sono da considerarsi come valori approssimati, non è possibile ottenere predizioni più accurate senza adoperare appropriate valutazioni sperimentali e nemmeno è di particolare interesse in questa fase iniziale dello sviluppo del modello. Il passo successivo di questo lavoro consiste nello sviluppo di un modello per la simulazione di pirolisi di gocce di asfalteni. Questo modello è stato sviluppato tenendo in conto le problematiche relative alla presenza di idrocarburi estremamente pesanti. In particolare, si è prestata attenzione agli aspetti numerici in quanto difficoltà sorgono dalla presenza degli asfalteni dati i valori estremi di alcune loro proprietà, come la viscosità e la tensione di vapore. Le simulazioni hanno evidenziato la necessità di un modello matematico più sofisticato che sia in grado di considerare la formazione di bolle nella fase liquida, fenomeno che viene osservato negli esperimenti. Difatti tensioni di vapore elevate vengono predette all'interno della goccia dovute ai composti leggeri che, formati a seguito del degrado termico degli asfalteni, non

sono in grado di diffondere all’esterno della fase liquida abbastanza velocemente quando la goccia viene riscaldata. Lavori futuri continueranno relativamente allo sviluppo del codice di calcolo rendendo possibile, quando fenomeni complessi come la nucleazione e il collasso delle bolle verranno approfonditi tramite sperimentazioni, implementare i modelli in grado di descrivere la formazione di bolle e la precipitazione di solido.

Abstract

Concerns about pollution and global warming are leading the major developed countries to increase the usage of renewable energy sources at the expense of fossil fuels. Despite that, nowadays oil still plays the major role in the global energy market and it will remain an essential resource for the world economics for decades to come. Reserves of light crude oils were the first being exploited, and with the time they are slowly depleting. This implies that oil is becoming increasingly heavier, and this trend will keep going in the future. One of the effects of this phenomena is the increase of availability of heavy fractions, obtained as side product in the extraction of lighter, most valuable fuels like gasoline and diesel. These heavy fractions hit the market as blends called Heavy Fuel Oils (HFO), as the name implies, they are intended to be used as fuels for power plants, furnaces and maritime transportations. HFOs are greatly available and cheap, thus making them suitable for heavy duty applications. On the other hand, their high viscosity, low volatility, high sulfur and nitrogen content and their low H/C ratio imply major challenges in obtaining clean combustion of these fuels. Production of great amounts of SO_X and NO_X and problems related to fouling are typical of units that employ heavy fuel oils. Major concerns are arising regarding the pollution related to the usage of HFOs as it can be seen in the actions taken by the International Maritime Organization (IMO) that reduced the maximum limit of sulfur content in maritime fuels from 3.5% wt to 0.5% wt in 2020. Switching to lighter, cleaner fuels often is not economically viable due to the increase of cost per energy, moreover it will lead to a surplus of HFOs. For these reasons, development of new technologies for the upgrade and clean combustion of heavy fuel oils are gaining increasing interest. In order to develop such technologies however, understanding the high temperature behavior of such compounds is mandatory. Today little is known about the combustion of this family of hydrocarbons and only recently efforts for the description of the liquid phase pyrolysis have been made. In this work a simplified kinetic scheme is implemented in a one-dimensional microgravity droplet model for the simulation of pyrolysis of isolated droplets. It was decided to investigate the high temperature behavior of droplets because the combustion and gasification of HFOs is done by the use of sprays, hence a good understanding of the droplet is extremely

useful for developing future models for real units. The species that compose the heavy fuel oils can be separated in four different fractions according to their polarity: saturates, aromatics, resins, and asphaltenes. These are also called SARA fractions. In the adopted kinetic model, each one of the SARA fractions of the HFO is represented as a mixture of reference species, then a simplified lumped reaction for the liquid phase pyrolysis of such reference species is defined. Of all the SARA fractions, this work focused exclusively on the asphaltene fraction of the HFOs because it is the major cause of coke formation and pollutant emission. The first step of this work is the development of a methodology for the prediction of the thermophysical properties of the involved species, in fact the asphaltenes reference species are complex species for which experimental evaluations of the main properties are not available. For this purpose, a set of group contribution methods and correlations for the prediction of properties of heavy hydrocarbons was selected and arranged in such a way that all the required properties can be computed only knowing the molecular structure of the reference species. The predictions obtained by this methodology are to be considered as approximate values, obtaining more accurate evaluations is not possible without appropriate experimental evaluations, nor it is of particular interest in this early stage of the model development. The second step of this work is the development of a software based on the numerical model for the simulation of the pyrolysis of asphaltenes droplet. The development of such model took into account all the issues related to the presence of extremely heavy hydrocarbons. More precisely, particular attention was paid to the numerical aspect of the model in order to cope with the issues generated by the extreme values of some asphaltenes' properties, like viscosity and vapor pressure. Simulations highlighted the need of a more sophisticated mathematical model capable of taking in account the formation of bubbles in the liquid phase, phenomena observed in experimental setups. Indeed, very high values of vapor pressure inside the droplet can be observed due to the light compounds generated by the pyrolysis of asphaltenes that are not able to diffuse out of the droplet fast enough when the droplet is heating. Future works will build upon the software obtained so far, bubble formation and solid precipitation could be implemented when experimental evaluations will provide the necessary data for a better understanding of complex phenomena such as nucleation and bubble disruption.

Contents

Ringraziamenti I

Sommario II

Abstract V

List of figures X

List of tables XI

1 Introduction 1

1.1 Aim and structure of the thesis 2

2 HFO Characterization 5

2.1 HFO overview 5

2.2 SARA characterization 6

2.2.1 Saturates 7

2.2.2 Aromatics 7

2.2.3 Resins 8

2.2.4 Asphaltenes 8

2.3 Reference species definition 10

2.4 Sample characterization 16

3 Kinetic model 17

3.1 Products definition 17

3.2 Parameters evaluation 18

4 Prediction of surrogate properties 20

4.1 Introduction 20

4.2 Methodology 21

4.3 Correlations 26

4.3.1 Normal boiling point 26

4.3.2 Critical properties 27
4.3.3 Vapor pressure 27
4.3.4 Liquid viscosity 28
4.3.5 Gas heat capacity 29
4.3.6 Enthalpy of formation 29
4.3.7 Gibbs free energy of formation 30
4.3.8 Standard entropy 30
4.3.9 Liquid density 31
4.3.10 Heat of vaporization 32
4.3.11 Acentric factor 32
4.3.12 Liquid heat capacity 33
4.3.13 Liquid thermal conductivity 33
4.3.14 Surface tension 33
4.3.15 Lennard-Jones potential parameters 34
4.3.16 Gas viscosity 34
4.3.17 Gas thermal conductivity 35
4.4 Validation 36
4.5 Computed properties 37
4.6 Char properties 37
4.7 Liquid mixture properties 39
4.7.1 Heat capacity 39
4.7.2 Thermal conductivity 40
4.7.3 Viscosity 40
4.7.4 Density 40
4.8 Gas mixture properties 40
4.8.1 Heat capacity 40

4.8.2 Thermal conductivity 41
4.8.3 Viscosity 41
4.8.4 Density 41
5 Numerical model 42
5.1 Assumptions 43
5.2 Mathematical model 44
5.2.1 Center of the droplet 45
5.2.2 Liquid phase 46
5.2.3 Interface 48
5.2.4 Gas phase 50
5.2.5 Outer boundary 51
5.3 Numerical implementation 51
5.3.1 Spatial discretization 51
5.3.2 Numerical algorithm 53
6 Simulations 55
6.1 Surface char accumulation 55
6.2 Evaporation simulation 67
7 Conclusions and outlooks 72
8 Appendices 74
8.1 Appendix A – Methodology validation 74
8.2 Appendix B – Reference species properties 84
9 Bibliography 94

List of figures

Figure 1.1: World energy consumption by energy source 1
Figure 2.1: Heavy fuel oil 6
Figure 2.2: SARA fractioning methodology 7
Figure 2.3: Proposed molecular structures for asphaltenes.. 10
Figure 2.4: Example of criteria for the selection of surrogate reference species atomic composition 13
Figure 2.5: Characterization of out-of-bounds samples 14
Figure 2.6: Surrogate reference species for the asphaltenes fraction 15
Figure 4.1: Morphology of the methodology's correlations network. 24
Figure 4.2: Species used for validation. 36
Figure 5.1: Polar coordinate system 44
Figure 5.2: Representation of droplet discretization 52
Figure 6.1: Temperature and char mass fraction profiles 57
Figure 6.2: Droplet shrinkage and relative liquid-surface velocity at the interface 59
Figure 6.3: Average droplet density over time 59
Figure 6.4: Sieve model 61
Figure 6.5: Mass fraction of char, benzene, and reference species 63
Figure 6.6: Effective Char-C_6H_6 diffusion coefficient 65
Figure 6.7: Concentration diffusion vs. friction diffusion 65
Figure 6.8: Char mass fraction, and uphill diffusion 66
Figure 6.9: Temperature and char mass fraction profiles - No C_6H_6 evaporation 67
Figure 6.10: Vapor pressure of methylnaphthalene and Asph1 69
Figure 6.11: Asph1 and $C_{10}H_7CH_3$ mass fractions 69
Figure 6.12: Temperature profile 70
Figure 6.13: Mixture vapor pressure 71

List of tables

Table 1: Properties of the reference species 16
Table 2: Pyrolysis reactions..... 19
Table 3: Required properties 20
Table 4: Simplified kinetic scheme 56
Table 5: Evaporation simulation operative conditions..... 68
Table 6: Properties of reference species and methylnaphthalene..... 68

1 Introduction

Growth in world population and world GDP are leading to an ever-increasing need of energy. Worldwide energy consumption in 2019 was around 160'000 TWh and it is deemed that it will increase to around 200'000 TWh by 2050. Nowadays the vast majority of the energy is supplied by fossil fuels, represented by coal, oil and natural gas. Of the fossil fuels, oil is the most exploited representing 39% of the total non-renewable energy production, against 32% of coal and 29% for natural gas [1]. Concerns about pollution and climate change are driving the major developed countries to limit their consumption of fossil fuels in favor of renewable sources, however the transition to green energy is proceeding at a slow pace and most probably will not be able to completely replace the other, cheaper, energy sources in the near future. For these reasons it is deemed that oil will still play a significant role in the energy market for several years to come, especially in the transportation sector, where liquid fuels are predominant [2].

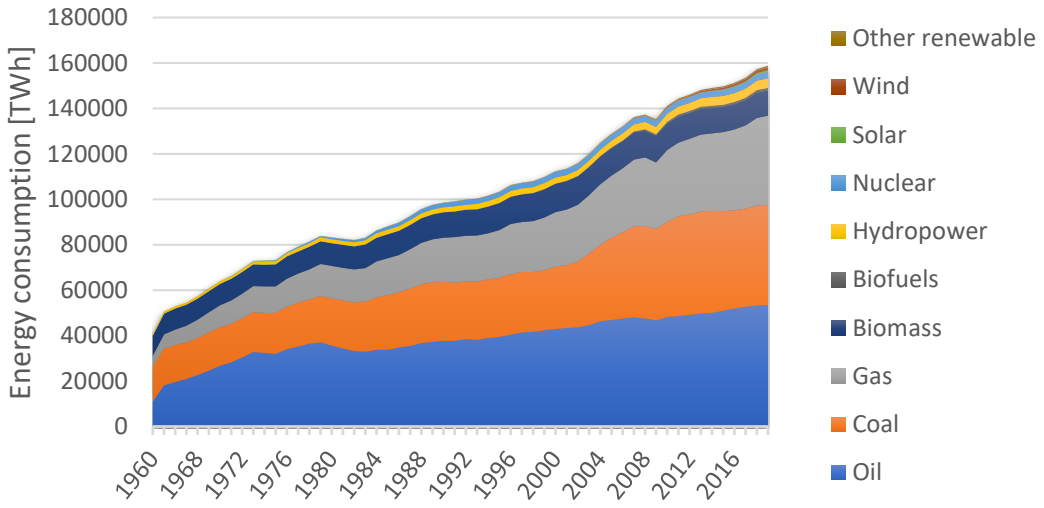

Figure 1.1: World energy consumption by energy source [1]

Due to their grater economical value and ease of extraction, lighter crude oil reserves were the first to be exploited; over time they are depleting, and the extraction is shifting over heavier oil reserves. The availability of heavier crude oil in conjunction with the transport industry's need for light fuels, led the refineries to adopt oil upgrading

technologies capable of converting heavy hydrocarbons into lighter ones. The side effect of such techniques is the increase of heavy fractions, obtained as side products. Such high carbon content streams are the main component of refinery blends called heavy fuel oils (HFO), sold as cheap energy sources for naval transportations, power plants, and heavy-duty boilers.

Heavy fuel oils cause concerns because of the emissions related to their combustion, the high content of sulfur and nitrogen lead to the production of SO_X and NO_X pollutants. The International Maritime Organization (IMO) standard entered into force in 2020, set the limit of maximum sulfur content for ocean-going vessels fuels to 0.5% wt lowering it from the previous limit of 3.5% wt. Moreover, the high carbon content combined with the low volatility are the cause of the formation of solid carbonaceous residues. Besides causing the emission of fine dusts this also entails major challenges in the design of the combustion units due to the formation of fouling. All these reasons are pushing the industry into developing new ways for upgrading heavy fuel oils. The research is mainly focused on desulphurization processes, and development of more efficient combustion solutions that lead to lower solid residue production.

1.1 Aim and structure of the thesis

In order to reach these goals, understanding the phenomena involved in heavy fuel oils high temperature processes is critical. At the moment, due to the complexity of such phenomena and the difficulties in the characterization of complex mixtures as heavy oil fractions, little progress was made by the scientific community in this field, the composition of HFOs and their pyrolytic behavior still remain mostly unknown. The work discussed in this thesis is part of the recently started project of the CRECK Modeling Group and KAUST University that aims to the development of a model for the description of pyrolysis and combustion of heavy fuel oils. In the work of E. Colombo [3] a methodology for the characterization of HFOs is proposed coupled with a simplified pyrolysis kinetic mechanism. This work involves the separation of the sample into 4 four fractions: saturates, aromatics, resins and asphaltenes. This separation technique is also called SARA fractioning, and the obtained fractions are called SARA fractions. Recently E. Colleoni improved both the characterization method and the kinetic mechanism [4].

Simulations of HFO thermogravimetry obtained in his work reached good agreement with experimental data. In this thesis the kinetic model developed by Colleoni is implemented inside a 1-D model for the simulation of pyrolysis of isolated droplets. It was decided to focus exclusively on the asphaltene fraction composing the HFO, this choice was done because asphaltenes are the heavy hydrocarbon species that generate more interest in the field, in fact they are deemed to be the main cause of the problems related to HFO combustion, as solid deposit and sulfur emissions.

The choice of the numerical model fell on a droplet model because HFOs, due to their low volatility, are always used as sprays in burners and gasifiers. The droplet is considered isolated in order to simplify the overall system description and to have a clearer view of the involved phenomena, without considering the interactions of neighboring droplets.

In the next chapter the technique used for the characterization of the HFOs is presented. The heavy fuel oils and the SARA fractions are described more in depth, with particular attention to the Asphaltenes fraction. The reference species used for the characterization of the asphaltenes fraction are shown and the criteria used for their definition are explained.

In Chapter 3 a brief explanation of the adopted kinetic mechanism for the pyrolysis of the asphaltenes reference species is shown. All the simplifications and assumptions made for the definition of the reactions and kinetic constants are listed.

Chapter 4 focuses on the methodology developed for the prediction of the reference species thermophysical properties. The assumptions the methodology is built upon and all the used correlations for the prediction of the properties are shown. In this chapter the reader is invited to consult Appendix A, where the accuracy of the methodology is evaluated, and Appendix B where the computed properties of the reference species are presented.

In Chapter 5 a detailed description of the mathematical model of isolated droplet is shown, all the assumptions and simplifications are discussed. A brief description of the numerical implementation is also presented.

In Chapter 6 the model is exploited to understand some of the phenomena involved in the pyrolysis of heavy fuel oils. In particular the accumulation of heavy compounds on the droplet surface is studied. Moreover, the limitations of the proposed model are highlighted and the aspects of the code that require future developments are identified.

2 HFO Characterization

Heavy fuel oils are composed by an extremely high number of different complex species that can reach values as high as 10^6, therefore a characterization based on molecular composition is unfeasible, nor it is practical for the development of a kinetic model [5]. Hence, simplified methods for the characterization of such mixtures are required. E. Colombo [3] recently proposed a methodology for the characterization of HFOs and for the development of a simplified pyrolysis kinetic scheme. Such methodology relies on the definition of a set of reference species whose blends are used for emulating the SARA fractions of the feedstock, then a kinetic scheme for the liquid phase pyrolysis is generated for each one of the surrogates. An improved version of this methodology developed by E. Colleoni [4] was used in this work.

2.1 HFO overview

HFOs are oil fractions obtained as residues of refinery and petrochemistry processes, like distillation and cracking. They are black, viscous, tar-like blends, mostly used as a cheap source of energy for furnaces or ship propulsion. Being residues of the crude oil fractioning and processing, they are composed mainly by aromatic hydrocarbons, so their H/C ratio is low, moreover they contain relevant quantities of heteroatoms, especially sulfur (up to 4.5% in mass), oxygen, nitrogen, and metals such as nickel, vanadium, iron, and copper. While originally HFOs were mostly residues of the atmospheric distillation of crude oil, nowadays, due to the increasing interest in raising the yields of light fuels in refineries, they are mainly formed by vacuum residues and cracking residues, for this reason HFOs are becoming heavier over time.

Figure 2.1: Heavy fuel oil

Commercially distributed HFOs can be found as they are, or they can be blended with lighter compounds in order to decrease their viscosity, they can have a broad variety of compositions including hydrocarbons with number of carbons as low as 20 up to 50 or more [6], their average molecular weight was calculated to be around 750 g/mol and due to the variability of composition their boiling point can span from 160°C up to 650°C [7].

2.2 SARA characterization

The most used methodology for the characterization of oil heavy fractions is the so-called SARA characterization firstly introduced by Jewell et. Al [8] in 1974. This technique involves the separation of the fuel into four smaller fractions, more precisely Saturates, Aromatics, Resins and Asphaltenes (the name SARA derives from the initial letter of the fractions). The separation exploits the different solubility and adsorption properties of the four mixtures mostly due to difference in polarity, and therefore it is performed by solvent extraction and chromatography. SARA fractioning does not follow a standardized procedure, and different methodologies are proposed in the literature; in Figure 2.2 the steps involved in a SARA fractioning following the procedure suggested by Statiev et al. [9] are shown.

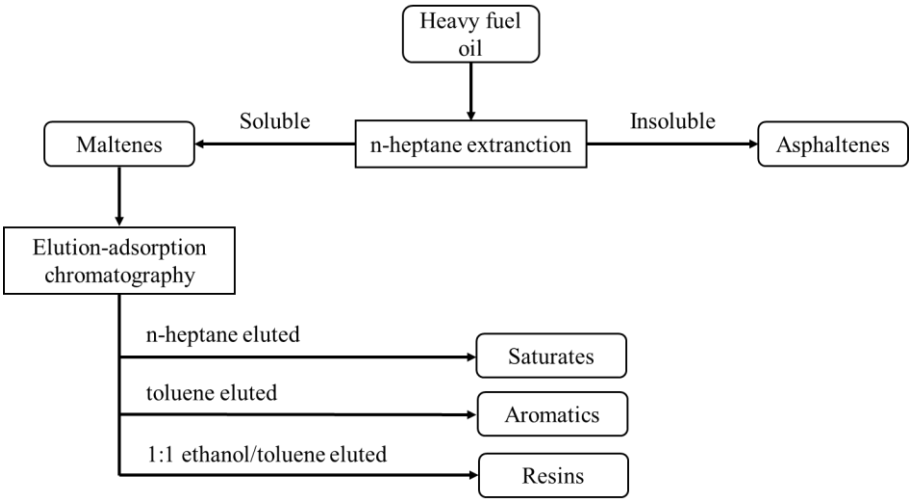

Figure 2.2: SARA fractioning methodology [9]

A brief description of the SARA fractions is presented.

2.2.1 Saturates

Saturates are the lighter molecules, mostly paraffinic as suggested by the H/C ratio ranging between 1.8 and 2.0, experimental evaluations suggests that the molecular weight falls in the range of 360 ÷ 860 g/mol [9]. They affinity towards n-heptane is explained by their non-polarity and mostly linear structure. This fraction is deemed to be free of heteroatoms and it appears as a translucent, low viscosity liquid.

2.2.2 Aromatics

Aromatics are heavier hydrocarbons with H/C ratio between 1.4 and 1.7. The lower H/C ratio is due to presence of naphtenic rings and especially aromatic rings (thus explaining their affinity with toluene). However, aliphatic chains are still present in the molecules. In the literature it is suggested that the molecular weight of such fraction is in the range of 450 ÷ 1080 g/mol [9]. Heteroatoms can be detected in trace, but this fraction is largely composed by pure, non-polar, hydrocarbons. The aromatic fraction is a viscous reddish liquid.

2.2.3 Resins

The resin fraction is a viscous dark-brown liquid, its H/C ratio is in the range of 1.3 ÷ 1.7 and molecular weight is suggested to be between 775 and 2780 g/mol [9]. In this fraction there is a relevant quantity of heteroatoms, the atomic analysis of resins fraction separated by several samples of HFOs and crude oils showed that the average mass fractions of the most relevant heteroatoms are: 0.73% N, 2.6% O and 3.6% S [3]. This fraction is more polar than the previous ones explaining the affinity to ethanol.

2.2.4 Asphaltenes

The asphaltenes fraction appears as a dark brown to black amorphous solid at room temperature, though crystallinity has been observed in certain circumstances [10, 11], indeed from the precipitation in n-heptane a black powder is obtained. The H/C ratio of such species varies between 1.0 and 1.3 thus suggesting molecular structures with poly-condensed aromatic rings.

The study of the molecular structure of the species contained in asphaltenes fractions has been a challenge for more than 70 years. It has been proven that such species contains condensed aromatic cores with aliphatic branching and bridges and heteroatomic moieties. Nitrogen, oxygen and sulfur can be found above 1% mass and in some cases they can reach values as high as 10% [12, 13, 14], study of several samples showed that the mean mass fractions of these elements are: 1.3% N, 2.6% O and 4.2% S. Relevant quantities of metals can also be found, especially nickel (up to 430 ppm) and vanadium (1580 ppm) [15]. Due to the presence of heteroatoms this SARA fractions show a moderate polarity. Despite the efforts, the chemical nature of the asphaltene fraction is not yet fully understood mainly because of the following reasons:

- The compounds of the mixture are widely different one from another.
- The larger molecules easily form aggregates, thus making it difficult to distinguish individual molecules from aggregates.
- During the separation process, while precipitating, the asphaltene fraction could form microporosities that can enclose smaller molecules of other fractions.

Because of the tendency of forming aggregates, the evaluation of the molecular weight of the involved species is not trivial; in the literature values spanning from 100 up to 80000 Da can be found [16, 17, 18], the bigger values are mainly due to the inability of some involved techniques to avoid the formation of big molecules' clusters. More recently, high-resolution mass spectroscopy techniques coupled with effective ionization methods (such as electrospray ionization and atmospheric pressure chemical ionization) suggested molecular weights distributions in the range of 400 – 1500 g/mol with a peak in the range of 600 – 850 g/mol [19, 20, 21]. The specific efforts of such methodologies to ensure the isolations of the single molecules make their results suitable as reference values for the generation of surrogate species.

Different models were proposed for both the prediction of asphaltenes molecular structures, and the mechanisms involved in their aggregation. Nowadays two models prevail for the description of the molecular structures, the continental model, and the archipelago model. The continental model states that the molecules in the asphaltene fraction are mainly composed by a big flat core of poly-condensed aromatic rings and naphtenic rings with some short aliphatic chains extending outwards. On the other hand, the archipelago model describes the asphaltenes as more flexible molecules made of small, condensed-rings groups linked together by a grid of aliphatic chains. Examples of molecules following the two models are shown in Figure 2.3. Recent studies support the validity of the former model over the latter [22]. It is unclear whether the asphaltenes molecules are dissolved or dispersed in the crude oil and HFOs, discording opinions can be found in the literature and it is not to be excluded that (due to the high variability in composition of different feedstocks) both phenomena can occur, and one can be predominant over the other depending on a per-case basis. Nevertheless, asphaltenes aggregation and precipitation under certain circumstances are well-observed phenomena.

The Yen-Mullins model [23] for the description of asphaltene molecules and their aggregation is one of the more accredited. Such model proposes molecular structures that follows the continental model with molecular weight in the range of 750 g/mol and dimensions in range of ~1.5 nm. The formation of aggregates is supposed to occur in 2 stages, as a first step, the molecules stack one over the other forming nanoaggregates of about 2 nm, this is done by the layering of the polycyclic cores like in graphite, such aggregates are composed by more or less 6 molecules. In the second step the

aforementioned nanoaggregates form clusters of about 8 elements whose overall dimension is in the range of 5 nm. Unlike other models, Mullins's group concluded that resins do not interact with the asphaltenes molecules nor their aggregates, hence they do not act as surfactant for the formation of asphaltenes' micelles.

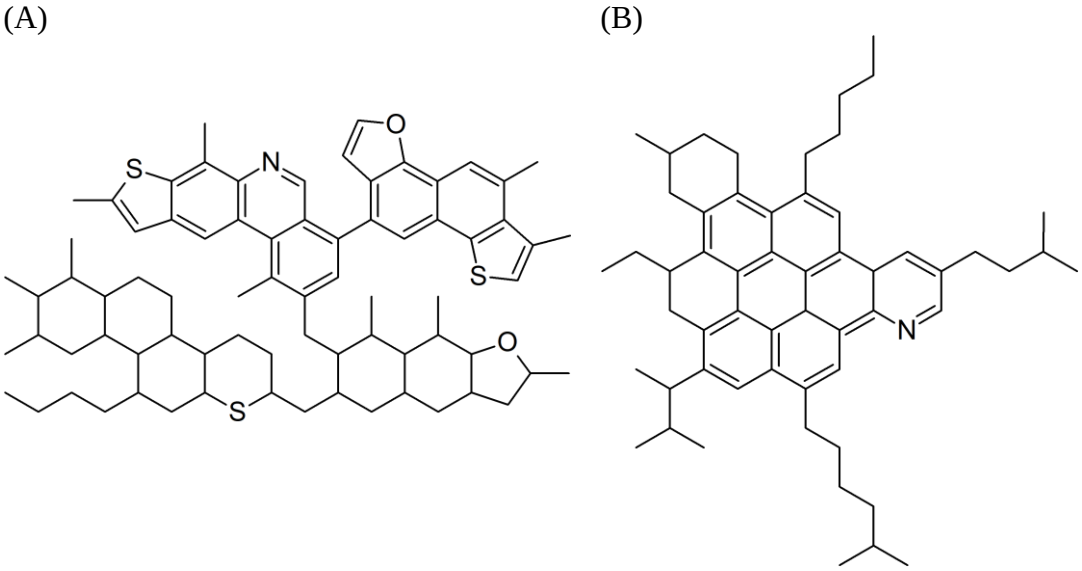

Figure 2.3: Proposed molecular structures for asphaltenes. (A) archipelago model, (B) continental model.

2.3 Reference species definition

The SARA fractioning is a powerful tool for the characterization of heavy fuel oils, especially for evaluating the distribution of the compounds based on their molecular weight and aromaticity. Despite that, this technique alone does not provide enough data for building a proper kinetic scheme, hence the methodology proposed by E. Colombo [3] suggests characterizing each of the SARA fractions as surrogate mixtures. The surrogates are mixtures made up of theoretical molecules, called reference species, generated with the purpose of representing at best the family of molecules present in the fraction to characterize. While the work of E. Colombo focused mainly on mimicking the chemical characteristics of the real mixtures, E. Colleoni [4] recently generated a set of reference species aiming also at representing the thermophysical characteristics of the real molecules. Because this thesis work is focused exclusively on the asphaltenes

fraction, only the methodology for the generation of the reference species of such fraction will be shown.

The reference species of the asphaltenes fraction are defined in such a way that the atomic composition of the fraction to characterize can be matched by a proper mixture of the reference species. This means that the following system of equations must be satisfied.

$$\begin{cases} \omega_i^{Asph} = \sum_{j=1}^{NS} \omega_j^{MIX} \omega_i^j \\ \omega_{i+1}^{Asph} = \sum_{j=1}^{NS} \omega_j^{MIX} \omega_{i+1}^j \\ \dots \\ \omega_{NE}^{Asph} = \sum_{j=1}^{NS} \omega_j^{MIX} \omega_{NE}^j \end{cases} \tag{2.1}$$

Where ω_i^{Asph} is the mass fraction of the *i-th* element in the asphaltene sample with i ranging from 1 to the total number of present elements NE, ω_j^{MIX} is the mass fraction of the *j-th* reference species in the surrogate mixture used for representing the sample, with j ranging from 1 to the total number of reference species NS, ω_i^J is the mass fraction of the *i-th* element in the *j-th* reference species. Once the atomic compositions of the sample and of the reference species are defined, the system is solved in order to find the vector of mass fractions of reference species in the surrogate mixture $\boldsymbol{\omega^{MIX}}$.

It is desirable to have only one solution that satisfies the system, meaning that there is one and only one mixture of reference species that matches the atomic composition of the sample. This is ensured by satisfying the following constraints:

- The number of adopted surrogates' reference species must be equal to the number of different elements in the sample.
- Each element present in the sample must appear in at least one reference species.
- The vectors $\boldsymbol{\omega^j}$ representing the atomic fractions of the reference species must be all linearly independent one from the other.

This means that the following conditions must be satisfied:

$$NS = NE \tag{2.2}$$

$$\boldsymbol{\omega^j} \neq k\boldsymbol{\omega^z} \;\; j = 1, \dots, NS; \; z = 1, \dots, NS; j \neq z; \; k \in \mathbb{R} \tag{2.3}$$

For the sake of simplicity, it is assumed that the asphaltene fraction contains only carbon, hydrogen, nitrogen, oxygen and sulfur atoms, other heteroatoms and metals are neglected. This assumption allows to define only one set of reference species that can be used for every asphaltene fraction to characterize, otherwise a different set of surrogate species should be defined if a different number of elements are detected by the atomic analysis of the sample. Furthermore, due to the low concentrations of heteroatoms other than the considered ones, their contribution to the physicochemical properties of the overall mixture is deemed to be negligible. Under this assumption only 5 reference species have to be defined for the asphaltenes fraction.

All these conditions ensure that there is a mathematical solution to the algebraic system (2.1), the next step is to guarantee that the solution is physically correct, thus meaning that all the mass fractions ω_j^{MIX} must be between 0 and 1.

$$0 \leq \omega_j^{MIX} \leq 1 \tag{2.4}$$

This means that the atomic composition of the surrogates species must be properly defined in such a way that the range of composition of their mixtures fully includes the range of possible compositions of the samples. In figure Figure 2.4 a graphical representation of the problem is shown, in order to facilitate the visualization, it is depicted a case in which only 3 elements are present in the samples.

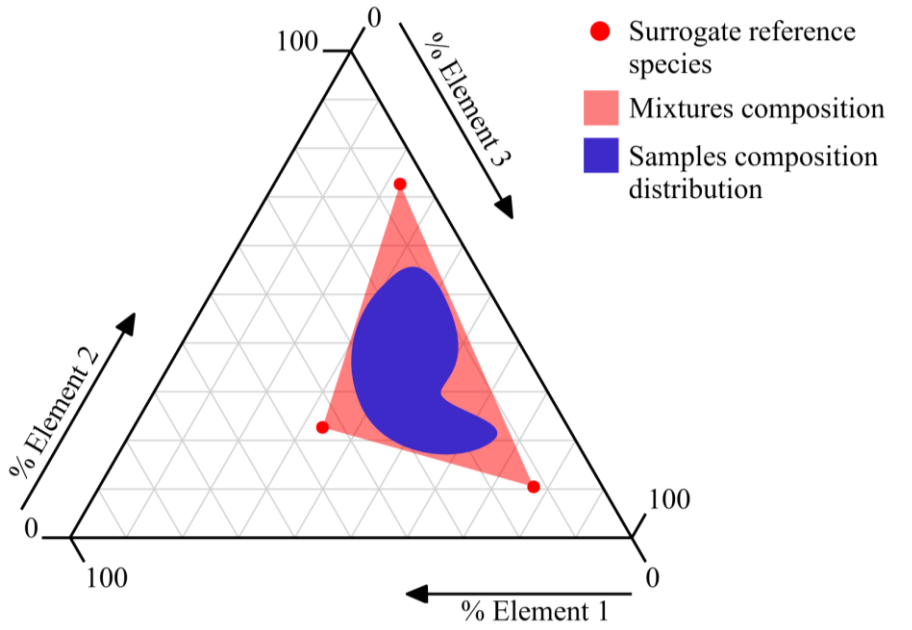

Figure 2.4: Example of criteria for the selection of surrogate reference species atomic composition

The first step is to identify the distribution of compositions of the asphaltene fraction, in the work of E. Colombo this was done by analyzing more than 200 experimental data about asphaltenes fractions' atomic composition. The large number of data and the broad variation in nature and location of extraction of the feedstock the asphaltenes sample were extracted from, should ensure that almost all the future analyzed samples will fall inside the bounds of the distribution. Due to the stochastic nature of the composition of the samples it is possible that some sample will have a composition non representable with a mixture of the defined reference species, in this case the mixture with the closer composition will be used as shown in figure Figure 2.5.

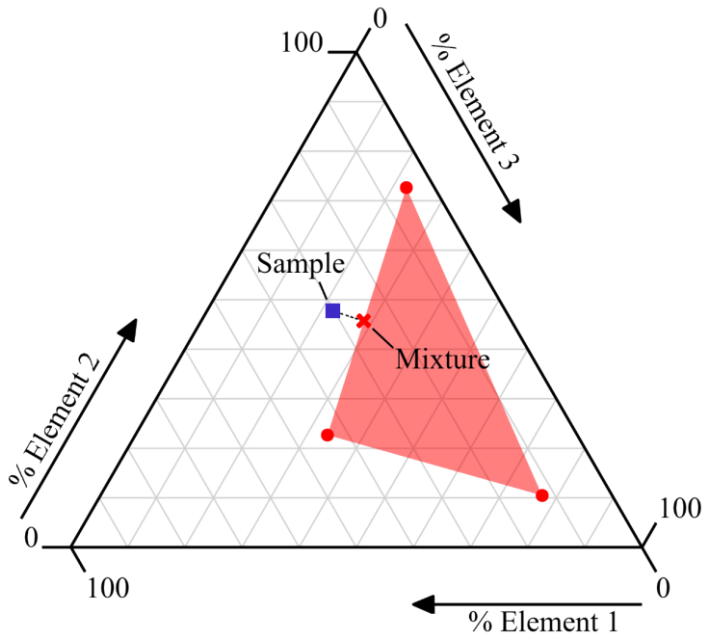

Figure 2.5: Characterization of out-of-bounds samples

In order to simplify both the definition of the surrogates species and their kinetic mechanisms, it was decided to have surrogates' reference species with at most one heteroatom. This condition combined with the constraint that all the surrogates reference species must be hydrocarbons leads to reference species with the following characteristics:

- Two reference species present only C and H atoms.
- One reference species shows only C, H and S.
- One reference species is composed only by C, H, and O atoms.
- The last reference species has only C, H and N atoms.

The last constraint used for the definition of the surrogates is that the reference species must have a molecular structure similar to the one of the molecules composing the fraction to characterize. As stated before, the structure of the asphaltenes is still subject of discussion in the scientific community, E. Colleoni defined the reference species for the asphaltenes fraction following the Yen-Mullins model [23]. Following criteria defied by this model are:

- Molecular weight in the range of ~750 g/mol.
- Molecular structure follows the continental model.
- The aromatic core is composed by ~7 condensed rings.
- The hydrocarbons' unsaturation is exclusively due to aromatic groups, no olefinic groups are present.

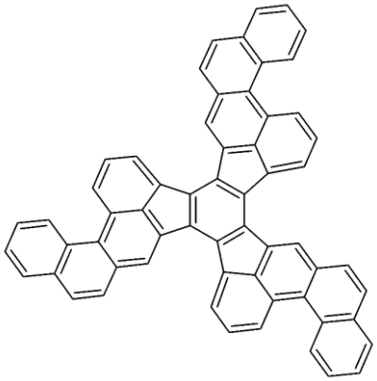

Asph1

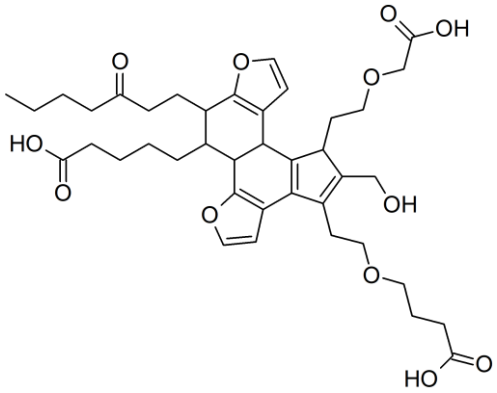

Asph2

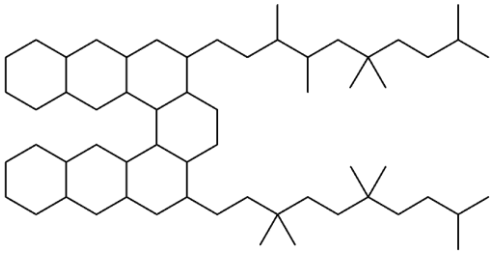

Asph3

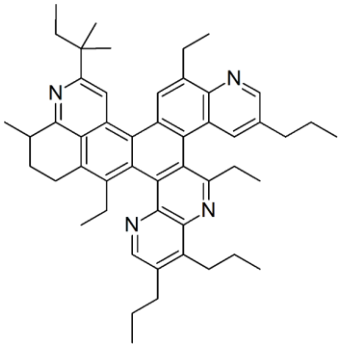

Asph4

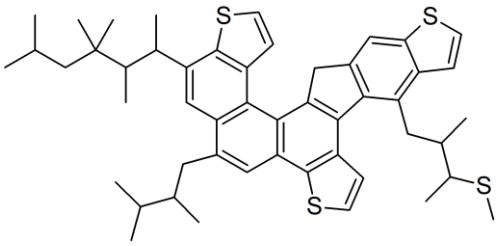

Asph5

Figure 2.6: Surrogate reference species for the asphaltenes fraction

Moreover, the selection of the functional group the heteroatoms are in must be representative of the real asphaltenes' molecules. Experimental analysis showed that oxygen forms both C–O and C=O bonds, with a prevalence of the former [24], carboxylic acid are also identified [25]. Sulfur forms mainly thiophene groups, lower quantities of sulfides, sulfoxides and sulfates are also measured [24, 26], however, sulfoxides and sulfates cannot be represented because of the hypothesis of reference species containing only one type of heteroatom. Nitrogen is present almost exclusively in aromatic rings. The five reference species obtained by E. Colleoni are shown in Figure 2.6.

Table 1: Properties of the reference species

	Formula	MW [g/mol]	% wt C	% wt H	% wt O	% wt N	% wt S
Asph1	$C_{60}H_{30}$	750.9	96.0	4.0	-	-	-
Asph2	$C_{40}H_{52}O_{12}$	724.8	66.3	7.2	26.5	-	-
Asph3	$C_{60}H_{108}$	829.5	86.9	13.1	-	-	-
Asph4	$C_{50}H_{60}N_4$	717.0	83.6	8.4	-	8.0	-
Asph5	$C_{50}H_{60}S_4$	789.3	76.1	7.7	-	-	16.2

2.4 Sample characterization

In order to characterize a sample, its atomic composition must be experimentally measured. Once the mass fractions of the 5 considered elements are known (C, H, O, N, S) the composition of the mixture of reference species that mimic the sample can be easily evaluated solving the algebraic linear system (2.1), that using the species proposed by E. Colleoni becomes:

$$\begin{cases} \omega_C^{sample} = 0.960\ \omega_{Asph1}^{MIX} + 0.663\ \omega_{Asph2}^{MIX} + 0.869\ \omega_{Asph3}^{MIX} + 0.836\ \omega_{Asph4}^{MIX} + 0.761\ \omega_{Asph5}^{MIX} \\ \omega_H^{sample} = 0.040\ \omega_{Asph1}^{MIX} + 0.072\ \omega_{Asph2}^{MIX} + 0.131\ \omega_{Asph3}^{MIX} + 0.084\ \omega_{Asph4}^{MIX} + 0.077\ \omega_{Asph5}^{MIX} \\ \omega_O^{sample} = 0.265\ \omega_{Asph2}^{MIX} \\ \omega_N^{sample} = 0.080\ \omega_{Asph4}^{MIX} \\ \omega_S^{sample} = 0.162\ \omega_{Asph5}^{MIX} \end{cases} \quad (2.5)$$

The resulting mixture should be a good approximation of the sample; indeed, it mimics both the atomic composition and the molecular structure of the real mixture.

3 Kinetic model

The kinetic model for the pyrolysis of the surrogates proposed by E. Colleoni was used in this work [4]. The model was developed under the hypothesis that the reference species do not interact one with another during the thermal decomposition. Clearly, this assumption is not true, indeed radicals produced by the thermal decomposition of a species can abstract atoms from another species, and the products generated by the pyrolysis of a surrogate's species change the overall mixture composition, thus changing the activity of species involved in the kinetics of the other reference species. Despite that, recent works based on such hypothesis showed good agreement with experimental data demonstrating that the interactions, although they are present, are of little importance to the overall pyrolysis process [3, 27]. The hypothesis of non-interaction allows for greatly simplified kinetic models; indeed, the overall kinetic scheme is obtained by simply merging the reactions of thermal decomposition of the single reference species, and no other reactions have to be added in order to take into account the interactions between surrogate's species.

The liquid phase pyrolysis of heavy hydrocarbons is an extremely complex phenomenon, involving a large number of reactions and species, including radicals. Many of these mechanisms are complicated and not fully understood, hence, at the moment, it is not possible to develop a detailed kinetic mechanism for the surrogates' liquid phase pyrolysis. The thermal decomposition of each of the reference species is modeled as a single first-order irreversible reaction with an Arrhenius law kinetic, whose task is to approximate the overall kinetic scheme.

3.1 Products definition

As stated before, pyrolytic processes produce a multitude of different species, trying to represent each of them leads to a kinetic scheme of overwhelming complexity. For this reason, similar species were lumped into a single product. For example, all the C6 paraffins are represented as a single C_6H_{14} product without making a distinction between

different isomers. This technique proved to be a useful tool to greatly simplify kinetic schemes at cost of a slight loss of accuracy [28].

The formation of solid carbon residue is a phenomenon well known to occur in asphaltenes' high temperature processes [29]. Such residue, also known as char, is a complex structure mainly formed by polycondensed aromatic rings. The actual molecular structure is extremely complex, and its definition is outside of the scope of this work, on the other hand, an accurate prediction of the mass yield of such residue is crucial since its formation is the cause of the main problems encountered in HFO combustion, as fouling and fine dust emission. In the kinetic model char is represented as the sum of the species CHAR, $CHAR_H$, $CHAR_O$, $CHAR_N$, and $CHAR_S$, these species represent the atoms of C, H, O, N, and S respectively that are part of the char molecules.

Experimental analysis of the gaseous products generated from asphaltenes' pyrolysis showed that the quantities of light hydrocarbons containing heteroatoms are negligible for oxygen and nitrogen, hence it is assumed that the only products containing such elements are CO, CO_2, and HCN. On the other hand, appreciable quantities of sulfur containing hydrocarbons are detected, all these species are lumped together and represented as benzothiophene, while the remaining sulfur forms H_2S.

3.2 Parameters evaluation

The stoichiometric coefficients and the kinetic constants were evaluated by fitting experimental data of pyrolysis products distribution and mass loss rates in asphaltenes' thermogravimetric analyses and pyrolysis experiments. Some constraints were set based on some considerations on the surrogate structure, for example reference species rich in aliphatic chains attached to the aromatic core were deemed to have higher production of light compounds at low temperature due to the lower activation energy of the beta-scission reaction for alkyl chains attached to aromatic rings. The sulfur containing surrogate's species was also considered to be fast reacting at low temperature due to the low energy of the C-S bonds.

The reactions proposed by E. Colleoni and their kinetic constants are shown in Table 2.

Table 2: Pyrolysis reactions

	k_0 [1/s]	E_{att} [cal/mol]
Asph1 → 8.62 H_2 + 3 CH_4 + 0.006 C_6H_6 + 0.031 C_7H_8 + 0.01 XYLENE + 0.01 $C_6H_5C_2H_5$ + 0.01 $C_6H_5C_2H_3$ + 0.019 $C_{10}H_7CH_3$ + 56.289 CHAR	$5.0 \cdot 10^{13}$	58000
Asph2 → 1.5 CO + 2 CO_2 + 2.434 CH_4 + 0.3 C_2H_4 + 1.385 C_2H_6 + 0.292 C_3H_8 + 0.074 C_3H_6 + 0.2 C_4H_{10} + 0.044 C_4H_8 + 0.738 C_5H_{12} + 0.344 C_5H_{10} + 0.639 C_6H_{14} + 0.256 C_6H_{12} + 0.012 CYC_6H_{12} + 0.05 C_6H_{10} + 0.025 $C_{10}H_{20}$ + 0.009 C_6H_6 + 0.044 C_7H_8 + 0.015 XYLENE + 0.015 $C_6H_5C_2H_5$ + 0.015 $C_6H_5C_2H_3$ + 0.026 $C_{10}H_7CH_3$ + 16.21 CHAR + 1.074 $CHAR_H$ + 6.5 $CHAR_O$	$2.5 \cdot 10^{11}$	46000
Asph3 → 0.5 H_2 + 4.2 CH_4 + 2 C_2H_4 + 1.843 C_2H_6 + 0.46 C_3H_8 + 0.8 C_3H_6 + 0.276 C_4H_{10} + 0.317 C_4H_8 + 1.068 C_5H_{12} + 1.378 C_5H_{10} + 0.921 C_6H_{14} + 0.987 C_6H_{12} + 0.01 CYC_6H_{12} + 0.36 C_6H_{10} + 0.04 $C_{10}H_{20}$ + 0.003 C_6H_6 + 0.014 C_7H_8 + 0.005 XYLENE + 0.005 $C_6H_5C_2H_5$ + 0.005 $C_6H_5C_2H_3$ + 0.008 $C_{10}H_7CH_3$ + 15.344 CHAR + 1.17 $CHAR_H$	$2.5 \cdot 10^{11}$	46000
Asph4 → 0.04 HCN + 1.22 CH_4 + 0.9 C_2H_4 + 0.832 C_2H_6 + 0.225 C_3H_8 + 0.8 C_3H_6 + 0.098 C_4H_{10} + 0.4 C_4H_8 + 0.798 C_5H_{12} + 0.6134 C_5H_{10} + 0.607 C_6H_{14} + 0.693 C_6H_{12} + 0.065 CYC_6H_{12} + 0.15 C_6H_{10} + 0.012 $C_{10}H_{20}$ + 0.001 C_6H_6 + 0.006 C_7H_8 + 0.002 XYLENE + 0.002 $C_6H_5C_2H_5$ + 0.002 $C_6H_5C_2H_3$ + 0.003 $C_{10}H_7CH_3$ + 23.807 CHAR + 0.515 $CHAR_H$ + 3.96 $CHAR_N$	$3.0 \cdot 10^{11}$	48000
Asph5 → 0.8 H_2S + 0.03 C_8H_6S + 1 CH_4 + 0.9 C_2H_4 + 0.014 C_2H_6 + 0.038 C_3H_8 + 0.924 C_3H_6 + 0.082 C_4H_{10} + 0.2 C_4H_8 + 0.551 C_5H_{12} + 0.394 C_5H_{10} + 0.339 C_6H_{14} + 0.38 C_6H_{12} + 0.075 CYC_6H_{12} + 0.13 C_6H_{10} + 0.083 $C_{10}H_{20}$ + 0.091 C_6H_6 + 0.124 C_7H_8 + 0.42 XYLENE + 0.281 $C_6H_5C_2H_5$ + 0.281 $C_6H_5C_2H_3$ + 0.281 $C_{10}H_7CH_3$ + 17.06 CHAR + 0.148 $CHAR_H$ + 3.17 $CHAR_S$	$1.0 \cdot 10^{10}$	41200

4 Prediction of surrogate properties

4.1 Introduction

In order to be able to simulate mass and energy transport phenomena, the knowledge of the main thermophysical properties of the involved species is mandatory. More precisely, Table 3 shows the set of the physical properties needed by the droplet model.

Table 3: Required properties

Symbol	Property
MW	Molecular weight
T_C	Critical temperature
P_C	Critical pressure
ρ_C	Critical density
T_{NBP}	Normal boiling point
p	Dipole moment
ω	Acentric factor
ΔH_f^0	Standard enthalpy of formation
S^0	Standard entropy
ϵ_{LJ}	Lennard-Jones self-collision diameter
σ_{LJ}	Lennard-Jones well depth
$P_{ev}(T)$	Vapor pressure
$\Delta H_{ev}(T)$	Heat of vaporization
$c_{pL}(T)$	Liquid heat capacity
$c_{pG}(T)$	Gas heat capacity
$k_L(T)$	Liquid thermal conductivity
$k_G(T)$	Gas thermal conductivity
$\mu_L(T)$	Liquid viscosity
$\mu_G(T)$	Gas viscosity
$\rho_L(T)$	Liquid density
$\sigma(T)$	Surface tension

The selected pyrolysis products (Table 2) are common species extensively studied in the past, so all the required properties can be found in the literature. In this work the data for such species were taken from "The Yaws Handbook of Physical Properties for Hydrocarbons and Chemicals" [30], from the data publicly shared by the National Institute of Standards and Technology, and from the ChemSep database [31].

On the other hand, the reference species for asphaltenes surrogates are complex molecules theoretically generated, they are not physically available, hence experimental evaluation of their properties is not possible, moreover such data are not available on the literature neither. For these reasons, a methodology for the prediction of the surrogates' properties had to be developed.

4.2 Methodology

The only data available for the reference species are the ones that can be inferred from the molecular structure of the reference species. They are:

- The molecular structure itself
- The molecular weight
- The atomic composition

All the other properties have to be derived from these data. This was accomplished by defining a set of correlations able to establish a relationship between each one of the required data and the known properties mentioned above. Unfortunately, correlations able to directly relate the results with the molecular structure are available only for a small set of properties, all the remaining properties have to be computed exploiting relationships with the other predicted properties. The indirect correlation of a property to the known data using relations with one or more predicted properties is not desirable because it involves error propagation. However, in some cases it was the only viable way, and with the correct precautions this issue can be curbed.

The methodology was developed under some assumptions. First of all, the asphaltenes aggregation phenomena were neglected, the reference species were assumed to be extremely viscous liquids at room temperature. This simplification is necessary due to the complexity and lack of understanding of the phenomena involved in the asphaltenes

aggregation. This assumption should lead to marginal errors mostly because the main focus is on studying the pyrolysis of the asphaltenes, and experimental observations show that asphaltenes are in the liquid state at the temperatures at which pyrolytic phenomena occur [32], so the physical interactions that leads to aggregation are deemed to be negligible in such conditions. It was also supposed that the properties of the pure reference species can be approximated with the properties of mixtures of hydrocarbons of similar nature. This hypothesis was set in order to overcome the lack of proper correlations, indeed, when suitable correlations for pure hydrocarbons were not available, correlation for similar petroleum fractions were used instead.

Three different kind of correlations were used for the computation of the properties: group contribution methods, theoretical correlations and empirical correlations.

Group contribution methods

Group contribution methods exploit the dependency of a species' property on its molecular structure, in particular they lay on the hypothesis that each group composing the molecule has a specific contribution to such property [33]. These methods work by identifying a set of functional groups that can be used to compose all the molecules of the target family of compounds, then, once the groups are defined, their contribution to a specific property is computed through statistical correlations using experimental data provided by databases. The used algorithms span from multilinear regressions to Artificial Neural Networks [34], and their performances deeply depend on the number and quality of the used experimental data, on the type of the chosen fitting function and on the number and type of functional groups defined. The advantage of group contribution methods is that they can extract as much information as possible from the molecular structure, and they suit at best situations where experimental data about the species are not available, moreover, exploiting the increase of computational power and increased availability of experimental data, they improved considerably their performance in properties prediction in recent years. For the aforementioned reasons, these methods, when available, were the go-to choice for the computation of the surrogates properties. The disadvantages of these methods are the need of extensive databases, and the numerical complexity of the statistical correlations used for their development.

Theoretical correlations

Theoretical correlations are equations that correlates two or more properties of a species so that knowing all the involved properties but one allows to compute the remaining one. These correlations are obtained theoretically developing a model that relies on specific assumptions and hypotheses. These correlations return extremely accurate predictions when all their hypotheses are met. On the other hand, they rely heavily on the accuracy of the input data and rarely correlations of such kind are available for liquid phase properties due to the complexity of the description of condensed state interactions.

Empirical correlations

Empirical correlations are similar to the theoretical correlations, they define the dependency of one property on a set of other properties, the difference lies on how they are obtained, in fact empirical correlation are deducted by fitting experimental data about the target family of species. Their availability and simplicity of use made these correlations especially popular in the oil industry for the prediction of refinery streams' properties, but usually their accuracy is acceptable only in a limited range of composition and properties values and their availability for heavy fuel oils is limited to a small number of properties.

As mentioned before group contribution methods are the better suited for our scope but well performing ones are not available for all the required properties shown in Table 3, so empirical and theoretical correlations had to be used for computing the missing properties.

The methodology for the prediction of the reference species' properties starts with the computation of all the properties for which a suitable group contribution method exists, since for such task only the known molecular structure is required. Once this set of properties is defined, they are fed to a net of interconnected theoretical and empirical correlations arranged in such a way that the output property of a correlation can be used as input for another correlation that requires the knowledge of such property. Figure 4.1 shows a scheme describing the connections between all correlations and group contribution methods, and the predicted physical properties.

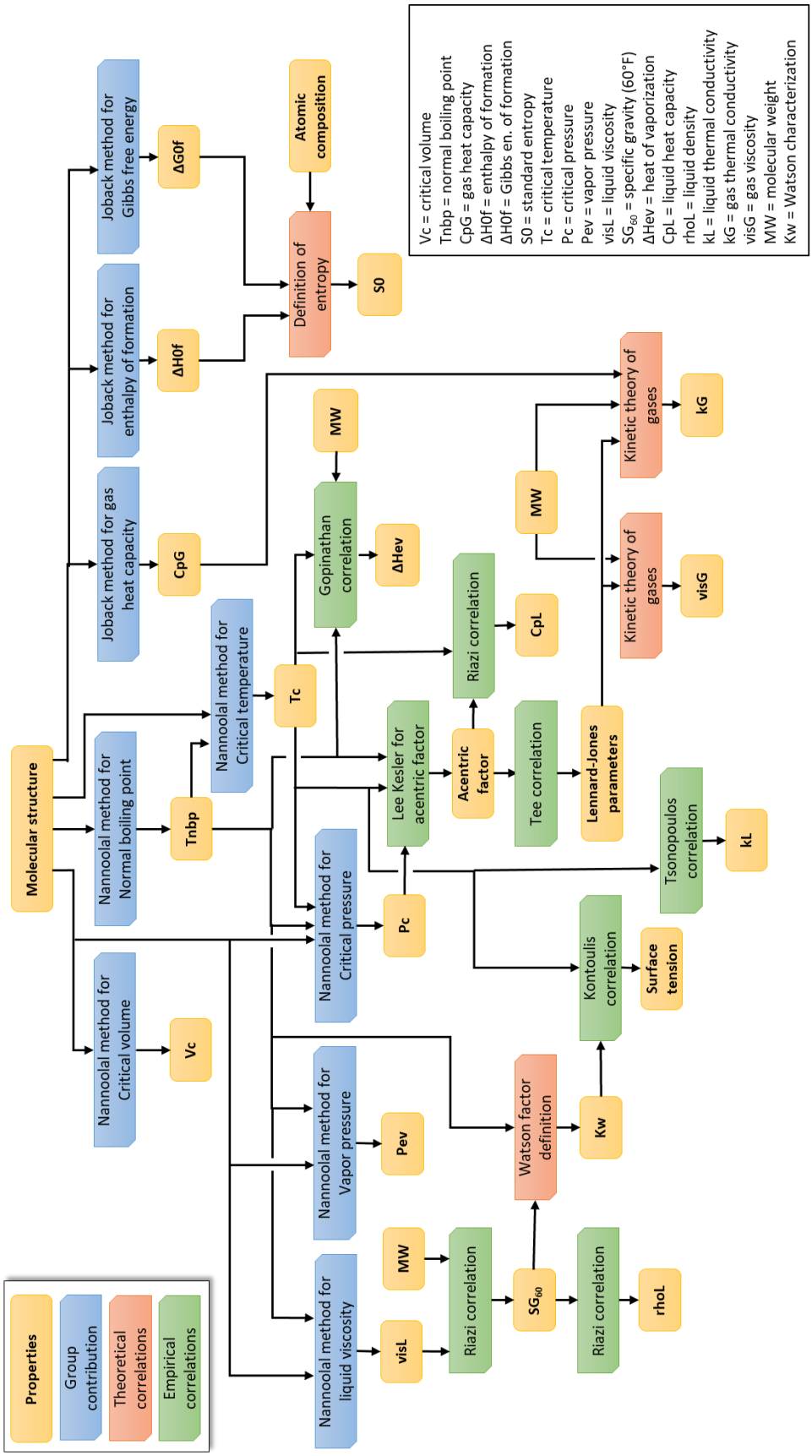

Figure 4.1: Morphology of the methodology's correlations network.

In order to limit the error propagation, particular attention was paid to the morphology of the correlations' net, indeed for some properties, multiple correlations were available, and each of them lead to a different configuration of the overall scheme. The best accuracy of the methodology is reached when each property is linked to the molecular structure using the least possible number of correlations, maintaining however good performing correlations. In an attempt of finding the best methodology, a large number of different configurations and correlations were tested, and the results were compared to experimental data.

During the development of the methodology, it was observed that an accurate prediction of normal boiling point and critical properties is fundamental for an overall good prediction of the species' properties. Indeed, these properties define the limit values of many other properties like vapor pressure and heat of vaporization. For this reason, particular attention was paid to the evaluation of these properties. In order to get the best accuracy for the critical values and normal boiling point, a group contribution method for their computation was searched. This was done in order to avoid correlating these properties to any other predicted property, thus eliminating error propagation. Several different group contribution methods were tested, and their accuracy was compared with experimental data. The group contribution method proposed by Nannoolal et al. [35, 36] showed to be the best performing by far, hence it was adopted.

Fortunately, accurate group contribution methods for other properties were found in the literature. This is useful for reducing the number of properties that have to be expressed as a function of other predicted values. On the other hand, the remaining properties have to be evaluated correlating their values with the predictions of the group contribution methods. This clearly implies that the error of the group contribution methods also affects the estimation of the other properties that are correlated to their predicted values. This problem was limited in the first place by selecting group contribution methods that give the least error possible. Then several different types of correlations were tested for each property, and their predicted values were compared to experimental data in order to select the correlation that is least affected by the error propagation.

A strength of this methodology is the capability of accepting known experimental data if any. Indeed, if some properties of the analyzed species are known, their values can be fed

to the system replacing the predicted data, thus removing the uncertainties related to the respective correlation. Introducing known values, also improves the accuracy of all the predicted properties that depends on such values, thus the more known data there are the more accurate the methodology becomes. The flexibility of the methodology makes it suitable for both the prediction of all the properties of an unknown species and for filling the few missing properties of a well-studied molecule.

4.3 Correlations

Here the correlations used in the methodology are listed and briefly explained.

4.3.1 Normal boiling point

The critical temperature was computed using the group contribution method proposed by Nannoolal et al. [36]. This is part of a series of group contribution method for the prediction of the properties of pure non-electrolyte organic compounds. The large amount of experimental data used for the estimation of the groups contributes (~2850 species), and the wide selection of groups make this methodology one of the best group contribution method available to date. This method takes also into account the contribution due to the interactions between the functional groups of the molecule. Accuracy of the predicted values is on average much better than all other equivalent methodologies, and a wide variety of different species can be represented thanks to the inclusion of a large number of functional groups. This method needs only the knowledge of the molecular structure, making it perfectly suitable for the task.

The proposed equation for the computation of the normal boiling point is:

$$T_{NBP} = \frac{\sum_i N_i C_i + GI}{n^{0.6583} + 1.6868} + 84.3395 \qquad (4.1)$$

Where T_{NBP} is the nomal boiling point of the species in [K], N_i is the number of *i-th* groups in the molecule, C_i is the contribution of the *i-th* group, and GI is the total contribution due to the functional groups' interactions. More information about the definition of the groups and their contributes can be find in the work of Nannoolal [36].

4.3.2 Critical properties

For the critical properties Nannoolal group contribution methods were used [35]. This is part of the work of Nannoolal for the estimation of pure organic compounds properties. The methodology used for the development of these correlations is similar to the one used for the prediction of the normal boiling point. Comparable performances are also achieved.

$$T_C = T_{NBP}\left(0.699 + \frac{1}{0.9889 + (\sum_i N_i C_i + GI)^{0.8607}}\right) \tag{4.2}$$

$$P_C = \frac{MW^{-0.14041}}{0.00939 + (\sum_i N_i C_i + GI)^2} \tag{4.3}$$

$$V_C = \frac{\sum_i N_i C_i + GI}{n^{-0.2266}} + 86.1539 \tag{4.4}$$

Where n is the total number of atoms in the molecule except hydrogen. T_C and T_{NBP} are expressed in [K], P_C in [kPa], and V_C in [m^3/mol].

4.3.3 Vapor pressure

The dependence of the vapor pressure on the temperature is predicted using Nannoolal group contribution method [37].

$$P_{ev}(T) = 10^{(4.1012+dB)\frac{T_{rb}-1}{T_{rb}-\frac{1}{8}}} \tag{4.5}$$

Where T_{rb} is the temperature divided by the normal boiling point ($T_{rb} = T/T_{NBP}$) and dB is the term that represents the groups contribution defined as:

$$dB = \left(\sum_i N_i C_i + GI\right) - 0.17055 \tag{4.6}$$

P_{ev} is expressed in [bar].

4.3.4 Liquid viscosity

The liquid viscosity is computed using the group contribution method proposed by Nannoolal [38]. In this case fewer experimental data were used for the regression of the group contributions (~1600), hence the accuracy of this method is lower than the previous ones, this is also due to the intrinsic difficulties in predicting liquid viscosities. Despite that, conventional correlations for the computation of the liquid phase viscosity of heavy hydrocarbons are very poor performing, thus making the selected method by far the best choice.

$$\ln\left(\frac{\mu_L(T)}{1.3}\right) = -dB_v\left(\frac{T - T_v}{T - \frac{T_v}{16}}\right) \tag{4.7}$$

Where dB_v and T_v are defined as follows:

$$dB_v = \frac{\sum_i N_i C_{dB_v\, i}}{n^{-2.5635} + 0.0685} + 3.7777 \tag{4.8}$$

$$T_v = 21.8444\, T_{NBP}^{0.5} + \frac{\left(\sum_i N_i C_{T_v\, i}\right)^{0.9315}}{n^{0.6577} + 4.9259} - 231.1361 \tag{4.9}$$

$C_{dBv\, i}$ and $C_{T_v\, i}$ are the contribution of the *i-th* group to the terms dB_v and T_v respectively. The temperature T is expressed in [K], and the viscosity μ_L is returned in [cP].

4.3.5 Gas heat capacity

Gas heat capacity is evaluated using the group contribution method proposed by Joback et al. [39]. With respect to the Nannoolal methods, in this case fewer groups are identified, and interactions between functional groups are not taken into account. Despite that, Joback methods are widely used nowadays for the computation of thermodynamic properties of hydrocarbons, thanks to their good accordance with experimental data. The proposed correlation is presented below.

$$c_{pG}(T) = A + B\,T + C\,T^2 + D\,T^3 \tag{4.10}$$

Where the parameters A, B, C, and D are computed as follows.

$$\begin{aligned} A &= \textstyle\sum_i N_i A_i - 37.93 \\ B &= \textstyle\sum_i N_i B_i + 0.21 \\ C &= \textstyle\sum_i N_i C_i - 3.91 * 10^{-4} \\ D &= \textstyle\sum_i N_i D_i + 2.06 * 10^{-7} \end{aligned} \tag{4.11}$$

N_i is the number of *i-th* groups in the molecule and A_i, B_i, C_i, and D_i are the contributions of the *i-th* group to the parameters A, B, C, and D respectively. More information on the groups and their contribution can be found in the work of Joback et al. [39]. The temperature T is in [K] and c_{pG} in [J/mol/K].

4.3.6 Enthalpy of formation

The standard enthalpy of formation is computed using the Joback group contribution method. The equation proposed by this work is the following:

$$\Delta H_f^0 = \sum_i N_i\,\Delta H_{fi}^0 + 68.29 \tag{4.12}$$

Where ΔH_{fi}^0 is the contribution of the *i-th* group to the standard enthalpy of formation. The value of ΔH_f^0 is returned in [kJ/mol].

4.3.7 Gibbs free energy of formation

Joback contribution method is also adopted for the evaluation of the standard Gibbs free energy of formation. The following equation is used.

$$\Delta G_f^0 = \sum_i N_i \, \Delta G_{fi}^0 + 53.88 \tag{4.13}$$

ΔG_{fi}^0 is the contribution of the *i-th* group to the standard Gibbs free energy of formation. ΔG_f^0 is expressed in [kJ/mol].

4.3.8 Standard entropy

The standard molar entropy is evaluated form the Gibbs free energy of formation and the standard enthalpy of formation using the definition of such properties; hence no error is added during the evaluation. First of all, the standard entropy of formation is computed using one of the definitions of the Gibbs free energy of formation:

$$\Delta S_f^0 = \frac{\Delta H_f^0 - \Delta G_f^0}{298K} \tag{4.14}$$

Then the standard molar entropy can be evaluated using the definition of the standard entropy of formation.

$$S^0 = \Delta S_f^0 + \sum_{i=1}^{NE} N_i \, S_i^0 \tag{4.15}$$

Where N_i is the number of atoms of the *i-th* element in the molecule, with i spanning from 1 to the total number of different elements present in the molecule NE, and S_i^0 is standard molar entropy of the *i-th* element. The values of ΔH_f^0 and ΔG_f^0 are both expressed in [kJ/mol], while the values of S_i^0 and S^0 are expressed in [kJ/mol/K].

4.3.9 Liquid density

The prediction of the liquid density of heavy hydrocarbons is not trivial, as for many other condensed state properties. Several different correlations were tested in search of an acceptable degree of accuracy of the predicted values, and the best results were obtained by combining two different correlations proposed by Riazi [40]. The first used equation was defined for the prediction of the molecular weight of petroleum heavy fractions.

$$MW = 223.56 \cdot \nu_{311.15K}^{-1.2435+1.1228 \cdot SG_{60}} \cdot \nu_{372.15K}^{3.4758-3.038 \cdot SG_{60}} \cdot SG_{60}^{-0.6665} \quad (4.16)$$

Where $\nu_{311.15K}$ and $\nu_{372.15K}$ are the kinematic viscosities at 311.15K and 372.15K respectively, they are expressed in [cSt], and SG_{60} is the specific gravity at 60F. The value of molecular weight is returned in [g/mol].

The second used correlation is obtained by a chart that describes the dependence of liquid density of hydrocarbons mixtures on the temperature. For the sake of simplicity of use and for making the correlation more suitable for numerical implementations, the data of the chart were fitted with a polynomial function. The resulting equation is showed below.

$$\begin{aligned} \rho_L(T) = 1000(&1.822 - 7.749 \cdot 10^{-3} \cdot T - 1.633 \cdot SG_{60} \\ &- 1.351 \cdot 10^{-6} \cdot T^2 + 0.01687 \cdot T \cdot SG_{60} \\ &- 0.5091 \cdot SG_{60}^2 + 1.152 * 10^{-6} \cdot T^2 \cdot SG_{60} \\ &- 9.635 \cdot 10^3 \cdot T \cdot SG_{60}^2 + 1.491 \cdot SG_{60}^3) \end{aligned} \quad (4.17)$$

In this equation the temperature is expressed in [K] and the density in [kg/m^3]. Two equations are needed in order to fill the unknown data SG_{60} that can be computed by solving the following system:

$$\begin{cases} MW = 223.56 \cdot \nu_{311.15K}^{-1.2435+1.1228 \cdot SG_{60}} \cdot \nu_{372.15K}^{3.4758-3.038 \cdot SG_{60}} \cdot SG_{60}^{-0.6665} \\ \nu_{311.15K} = \dfrac{\mu_L(311.15K)}{\rho_L(311.15K, SG_{60})} \\ \nu_{372.15K} = \dfrac{\mu_L(372.15K)}{\rho_L(372.15K, SG_{60})} \end{cases} \quad (4.18)$$

The viscosity values can be computed using the Nannoolal group contribution method (equation (4.7)).

4.3.10 Heat of vaporization

The heat of vaporization is predicted using the correlation proposed by Nishanth et al. [41]. This correlation is valid for pure hydrocarbons and for petroleum fractions as well.

$$\Delta H_{ev}(T) = \Delta H_{ev}(T_{NBP}) \left(\frac{1 - \frac{T}{T_C}}{1 - \frac{T}{T_{NBP}}} \right)^{0.38} \tag{4.19}$$

Where $\Delta H_{ev}(T_{NBP})$ is evaluated as follows:

$$\Delta H_{ev}(T_{NBP}) = 1.081 \cdot 10^3 + SG_{60}^{-0.01418} T_{NBP} \left(31.98 \log_{10}(T_{NBP}) + 22.12 \frac{T_{NBP}^{-1.573}}{MW} \right) \tag{4.20}$$

$\Delta H_{ev}(T)$ and $\Delta H_{ev}(T_{NBP})$ are expressed in [kJ/kg], T, T_C and T_{NBP} are in [K], and the molecular weight is in [g/mol].

4.3.11 Acentric factor

Acentric factor is predicted using the correlation proposed by Lee and Kesler for heavy hydrocarbons [42].

$$\omega = \frac{\ln P_{br} - 5.92714 + \frac{6.09648}{T_{br}} + 1.28862 \ln T_{br} - 0.169347\, T_{br}^6}{15.2518 - \frac{15.6875}{T_{br}} - 13.4721 \ln T_{br} + 0.43577\, T_{br}^6} \tag{4.21}$$

Where P_{br} is defined as $P_{br} = 1/P_C$, with P_C expressed in [bar], and T_{br} is defined as $T_{br} = T_{NBP}/T_C$.

4.3.12 Liquid heat capacity

The liquid heat capacity is predicted computing the difference between the liquid heat capacity and the ideal gas heat capacity with the correlation proposed by Riazi [40].

$$\frac{C_{pL} - C_{pG}^{id}}{R} = 1.586 + \frac{0.49}{1 - T_r} + \omega \left[4.2775 + \frac{6.3(1 - T_r)^{\frac{1}{3}}}{T_r} + \frac{0.4355}{1 - T_r} \right] \quad (4.22)$$

Where T_r is the reduced temperature defined as $T_r = T/T_C$. Both C_{pL} and C_{pG}^{id} are expressed in [J/mol/K].

4.3.13 Liquid thermal conductivity

The correlation proposed by Tsonopoulos et al. [43] for the computation of coal liquids and heavy fractions liquid thermal conductivity is used. Despite its simplicity, this correlation showed to be very accurate, mainly due to the low variability of thermal conductivity of heavy petroleum fractions.

$$k_L(T) = 0.05351 + 0.10177\ (1 - T_r)^{2/3} \quad (4.23)$$

The value of k_L is in [W/m/K].

4.3.14 Surface tension

The surface tension is evaluated using the correlation proposed by Kontoulis et al. [44], for heavy petroleum fractions.

$$\sigma(T) = 673.7\ [1 - T_r]^{1.232}\ K_w^{-1} \quad (4.24)$$

Where K_w is the Watson characterization factor defined as:

$$K_w = 1.8 \frac{T_{NBP}^{1/3}}{SG_{60}} \quad (4.25)$$

T_{NBP} is in [K], and the surface tension is returned in [mN/m].

4.3.15 Lennard-Jones potential parameters

The parameters of the Lennard-Jones potential are computed using the correlation for organic compounds proposed by Holley et al. [45].

$$\sigma_{LJ} = (2.3511 - 0.0874\ \omega)\left(\frac{T_C}{P_C}\right)^{1/3} \tag{4.26}$$

$$\epsilon_{LJ} = (0.7915 + 0.1693\ \omega)\ k_B\ T_C \tag{4.27}$$

Where k_B is the Boltzmann constant in [erg/K]. T_C and P_C are in [K] and [bar] respectively. The self-collision diameter σ_{LJ} is expressed in [Å] and the well depth is returned in [erg].

4.3.16 Gas viscosity

The gas viscosity is evaluated using the kinetic theory of gases:

$$\mu_G(T) = \frac{5}{6}\frac{\sqrt{\pi\ m\ k_B\ T}}{\pi\ \sigma_{LJ}^2\ \Omega^{(2,2)^*}} \tag{4.28}$$

Where m is the molecular mass in [kg], k_B is in [J/K] and the temperature is in [K]. The gas viscosity is returned in [Pas]. The value of the collision integral $\Omega^{(2,2)^*}$ is obtained by interpolation of the data charts proposed by Monchick et al. [46].

4.3.17 Gas thermal conductivity

The gas thermal conductivity is also computed using the kinetic theory of gases.

$$k_G(T) = \frac{\mu_G}{MW}\left(f_{trans}C_{v,trans} + f_{rot}C_{v,rot} + f_{vib}C_{v,vib}\right) \tag{4.29}$$

Where:

$$f_{trans} = \frac{5}{2}\left(1 - \frac{2}{\pi}\frac{C_{v,rot}}{C_{v,trans}}\frac{A}{B}\right) \tag{4.30}$$

$$f_{rot} = \frac{\rho_G D_{kk}}{\mu_G}\left(1 + \frac{2}{\pi}\frac{A}{B}\right) \tag{4.31}$$

$$f_{vib} = \frac{\rho_G D_{kk}}{\mu_G} \tag{4.32}$$

$$A = \frac{5}{2} - \frac{\rho_G D_{kk}}{\mu_G} \tag{4.33}$$

$$B = 1 + \frac{2}{\pi}\left(\frac{5}{3}\frac{C_{v,rot}}{R} + \frac{\rho_G D_{kk}}{\mu_G}\right) \tag{4.34}$$

$$C_{v,trans} = \frac{3}{2}R \tag{4.35}$$

$$C_{v,rot} = \frac{3}{2}R \tag{4.36}$$

$$C_{v,vib} = C_p - \frac{7}{2}R \tag{4.37}$$

$$D_{kk} = \frac{3}{16}\frac{\sqrt{2\pi k_b^3 T^3/m}}{P\pi\sigma_{LJ}^2\Omega^{(1,1)^*}} \tag{4.38}$$

The collision integral $\Omega^{(1,1)^*}$ was evaluated interpolating the values of the charts proposed by Monchick et al. [46]. μ_G is in [Pas], the molecular weight in [kg/mol], m in [kg], k_B in [J/K], the temperature is expressed in [K], the pressure in [Pa], and the Lennard-Jones

self-collision diameter is in [m]. The value of gas thermal conductivity is returned in [W/m/K].

4.4 Validation

Experimental data for the properties of hydrocarbons with molecular weight and aromaticity in the range of the asphaltenes' surrogates are not available in the literature, mostly because of the difficulty of separating them from the petroleum mixtures. For this reason, the validation of the methodology for the computation of the properties for surrogates' reference species had to be done using the experimental data of species that do not precisely meet the characteristics of asphaltenes surrogates. The species selected for the validation are hexatriacontylbenzene, chrysene, squalane, diphenyl disulfide, and pyrene. Their molecular structure is shown in Figure 4.2. These compounds were selected because of their high molecular weight and/or high aromaticity, making them the species most similar to asphaltene surrogates whose properties are available.

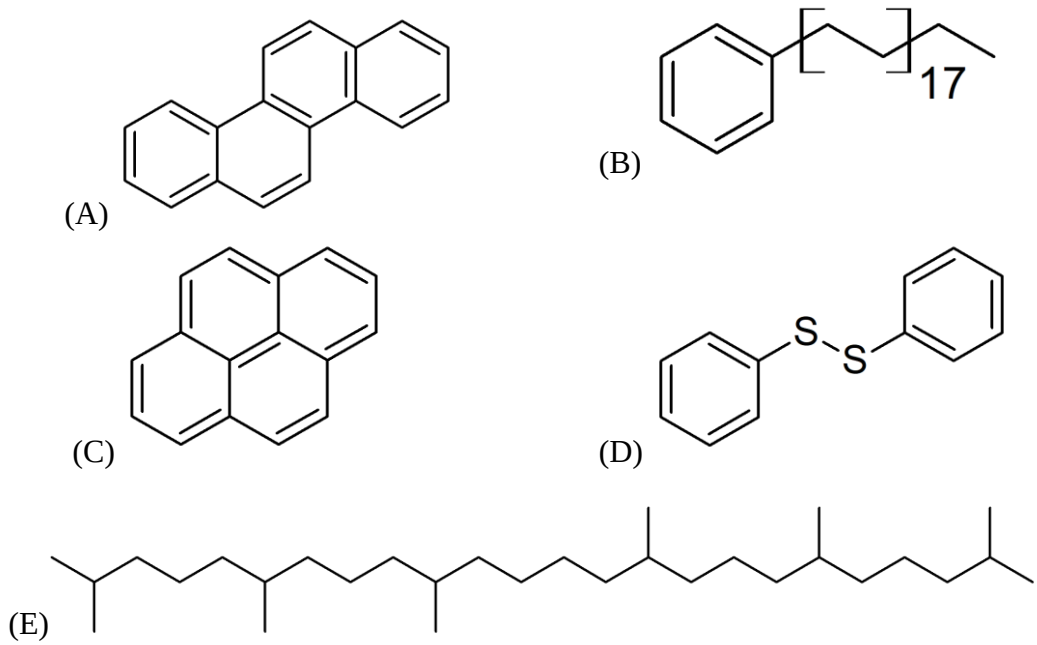

Figure 4.2: Species used for validation.

(A) Chrysene; (B) Hexatriacontylbenzene; (C) Pyrene; (D) Diphenyl disulfide; (C) Squalane

Appendix A shows a comparison between the experimental data and the predicted properties for the aforementioned species. As it can be seen for some properties there is still margin for improvement. In particular large discrepancies can be observed in the properties computed using empirical correlations, like the liquid thermal conductivity. This is mostly due to the fact that the species used for the validation are significantly different from the species and or mixtures studied for the development of the correlation. The obtained data were deemed to be accurate enough to be used for the simulations, after all relevant uncertainties are still present both in the kinetic model and in the surrogates definition, and accurate quantitative predictions are not the aim of this work. Future works can improve the methodology by carrying out an experimental campaign for the measurement of asphaltenes properties and developing ad hoc correlations.

4.5 Computed properties

The methodology for the computation of the thermophysical properties was implemented in MATLAB, and a fully automated code was developed. The code only requires as input the information about the molecular structure of the species, more precisely the list of Nannoolal groups present in the molecule, their frequency and the number of each element composing the molecule are the only inputs to the code.

The code was used for predicting the properties of all the reference species, and their values can be found in Appendix B.

4.6 Char properties

The species composing the carbonaceous residues are large polyaromatic hydrocarbons with extremely low H/C ratios. This species precipitates forming graphite-like solid particles, whose exact composition and structure is extremely variable and dependent on the conditions in which the solid is formed. Trying to accurately predict the properties of the solid compounds is outside of the scope of this work. As it will be shown in the following chapter, the developed numerical model does not include a proper solid phase, so the char is represented as a liquid whose properties are defined in order to approximate the real behavior of the solid phase.

Sublimation of solid carbonaceous compounds can be neglected thus it can be assumed that the release of such species in the gas phase is negligible. In order to represent this behavior with a liquid species, the vapor pressure of the char is set to be null. Avoiding completely the evaporation of this species, the values of normal boiling point, heat of vaporization, critical properties and all the gas properties do not affect anymore the simulations, hence any arbitrary value can be attributed to them.

The actual density of petroleum coke, without considering the porosity, is slightly lower that the density of the graphite, and it spans in the range of 2000 – 2250 kg/m^3 [47, 48, 49]. The more the coke is calcined at high temperatures the higher the density. The temperatures and residence times involved in the pyrolysis of heavy fuel oils are lower than in the production of petroleum coke, hence it is reasonable to assume that the char produced in these conditions have density on the lower end of the range. For this reason, a value of 2000 kg/m^3 was adopted for the char species. The variation of density with the temperature was neglected because coke species shows an extremely low thermal expansion [50], thus the value was considered as constant.

The estimation of the char viscosity is not trivial, indeed being a solid it has an infinite viscosity. Attributing an infinite value to the viscosity is not possible because, in addition to causing numerical problem in the simulations, it will lead to an infinite mixtures' viscosity even when small amounts of char are present in the liquid phase. Experimental observations show that the viscosity of a liquid phase with solid particles dispersed in it increases when the volume fraction of dispersed solid increases. Many different models are proposed in the literature for the prediction of the viscosity of liquid-solid dispersions. A simple but effective correlation, valid for spherical solid particles, is the so-called Einstein equation [51]:

$$\mu = \mu_0(1 + 2.5\,V) \tag{4.39}$$

Where μ is the viscosity of the dispersion, μ_0 is the viscosity of the dispersion medium, and V is the volume fraction of solid in the dispersion. This kind of dependence of the viscosity on the solid fraction cannot be accurately represented with the mixing rule for the viscosity of the liquid phase used in the model (Equation (4.42)). However, a good

approximation of such behavior can be obtained by attributing to the char a high value of viscosity, constant with the temperature.

All the remaining properties were considered to be equal to the one of the reference species Asph1, because due to its high aromaticity it is the species that better resembles the char components.

Under these assumptions, relevant errors in the prediction of the char properties are made, these errors are mainly consequences of the representation of the char as a liquid species rather than a solid one. However, at this stage of the model development the main focus is to gather qualitative observations of the phenomena that involves the char. Future developments of the model will lead to the implementation of a proper solid phase for the char, and with the help of ad-hoc experimental evaluation, better prediction of the solid properties could be done.

4.7 Liquid mixture properties

Once the properties for each species involved in the kinetic mechanism are defined, a set of mixing rules for the prediction of the properties of their mixtures has to be defined. Here the used mixing rules are listed.

4.7.1 Heat capacity

The liquid heat capacity of the mixture is computed using the ideal mixtures mixing rule.

$$C_{pL}^{MIX} = \sum_{i=1}^{NSL} C_{pL,i}\, W_{L,i} \tag{4.40}$$

Where NSL is the number of species in the liquid phase and $W_{L,i}$ is the mass fraction of the *i-th* species. The apex MIX indicates that the properties is related to the mixture.

4.7.2 Thermal conductivity

The mixing rule proposed by Vredveld [52] for nonaqueous systems is used for the evaluation of the liquid thermal conductivity.

$$k_L^{MIX} = \left(\sum_{i=1}^{NSL} k_{L,i}^{-2} \, W_{L,i} \right)^2 \tag{4.41}$$

4.7.3 Viscosity

The liquid mixture viscosity is computed using the mixing rule proposed by Quinones-Cisneros et al. [53] based on the friction theory.

$$\mu_L^{MIX} = \exp\left(\sum_{i=1}^{NSL} x_i \ln(\mu_{L,i}) \right) \tag{4.42}$$

Where x_i is the molar fraction of the *i-th* species.

4.7.4 Density

The density of the liquid mixture is computed using the additive volumes mixing rule.

$$\rho_L^{MIX} = \left(\sum_{i=1}^{NSL} \frac{W_{L,i}}{\rho_{L,i}} \right)^{-1} \tag{4.43}$$

4.8 Gas mixture properties

4.8.1 Heat capacity

The mixing rule for ideal gases is used for the evaluation of the gas mixture heat capacity.

$$C_{pG}^{MIX} = \sum_{i=1}^{NSG} C_{pG,i} \, y_i \tag{4.44}$$

Where NSG is the number of species in the gas phase, and y_i is the molar fraction of the *i-th* species in the gas mixture.

4.8.2 Thermal conductivity

The thermal conductivity of the gas mixture is computed using the correlation proposed by Burgoyne and Weinberg [54].

$$k_G^{MIX} = 0.5 \left(\sum_{i=1}^{NSG} y_i \, k_{G,i} + \left(\sum_{i=1}^{NSG} \frac{y_i}{k_{G,i}} \right)^{-1} \right) \tag{4.45}$$

4.8.3 Viscosity

The viscosity of the gas mixture was computed using the mixing rule proposed by Herning and Zipperer [55].

$$\mu_G^{MIX} = \frac{\sum_{i=i}^{NSG} y_i \, \mu_{G,i} \sqrt{MW_i}}{\sum_{i=i}^{NSG} y_i \sqrt{MW_i}} \tag{4.46}$$

4.8.4 Density

The ideal gases mixing rule is used for the evaluation of the gas mixture density.

$$\rho_G^{MIX} = \frac{P \, MW_G^{MIX}}{R \, T} \tag{4.47}$$

Where P is the pressure, R is the gas constant, T is the temperature and MW_G^{MIX} is the molecular weight of the mixture computed as follows:

$$MW_G^{MIX} = \left(\sum_{i=1}^{NSG} \frac{y_i}{MW_i} \right)^{-1} \tag{4.48}$$

5 Numerical model

Pyrolysis of heavy fuel oils involves several species and complex chemical reactions; observations of high temperature experiments show the formation of bubbles inside the liquid phase due to the evaporation of the generated light hydrocarbons while outside, at the interface with the surrounding gas, a solid layer is generated by the accumulation of carbonaceous residues [29]. The intrinsic complexity of the aforementioned phenomena in conjunction with the uncertainties in the HFO compositions, its properties, and the involved kinetics, makes it clear that the development of a comprehensive and detailed theoretical model, that is able to quantitatively describe all the involved phenomena, is not possible at the moment. Hence, some simplifications have to be done in order to develop a model for HFO pyrolysis.

On top of that the challenges related to the numerical implementation of a model cannot be neglected. When complex CFD models are applied to multiphase reactive systems, achieving acceptable CPU times and numerical stability is not a trivial task. That is especially true in this specific case, indeed, the presence of heavy hydrocarbons, like the asphaltene's surrogates, add an extra layer of numerical complexity due to some of their properties that can reach extreme values, like vapor pressure and viscosity. Hence, a simplified model is required to make simulations reliable and suited for personal computers. Moreover, this model is intended to be used as a tool for the refinement of the kinetic model, the intrinsic trial and error nature of the kinetic model development and validation makes mandatory to use a numerically efficient model, therefore accurate CFD model cannot be used due to their inherent large computational times.

Although a simplified model can lose the ability of describing quantitatively the real-case phenomena, it still remains a useful tool for understanding the involved phenomena and their dependence on the operative conditions. Moreover, a simplified model is helpful for learning how the more challenging aspect of such simulations could be tackled in future, more advanced, models.

In this work a modified version of the microgravity droplet solver part of the OpenSMOKE++ framework [56] was developed.

The software is built upon a one-dimensional model formulated by Cuoci et al. [57] that describes evaporation, mass and energy transport phenomena and liquid and gas phase chemical reactions in isolated liquid droplets.

5.1 Assumptions

The first assumption is that the system is in a zero-gravity environment and there are not forced convection fluxes in the system, this allows to consider the system as one dimensional with spherical symmetry. In fact, the absence of gravitational acceleration avoids any buoyancy effect thus eliminating any natural convection flux. Such hypothesis extremely simplifies the fluid dynamics of the system and thanks to its big advantages it is widely adopted in the study of isolated droplets' evaporation and ignition. Such conditions are also recreated experimentally by the use of free falling towers or by performing the experiment on the International Space Station [58] [59] [60] [61] [62].

These assumptions imply that:

- The droplet is perfectly spherical, and it keeps the spherical shape even while it changes size due to evaporation or thermal expansion.
- Properties vary only along the radial coordinate so each spherical shell of infinitesimal thickness concentric to the droplet is homogeneous.
- Energy and mass fluxes occur only along the radial coordinate.
- There are no convective fluxes due to buoyancy effects. The only convective fluxes present are due to the evaporation and the thermal expansion.

The following assumptions are also made:

- There are only one liquid phase and one gas phase.
- A one-dimensional radial coordinate system is used, with origin located in the center of the spherical droplet. This system is equivalent to a polar system where the angular coordinates are neglected because no properties variations occur along these coordinates.
- Evaporation and thermal expansion generate low velocity both in liquid and gas phase, so no turbulent regime is considered.

- Thermodynamic equilibrium is reached at the interface between liquid and gas phase.
- The species composing the atmosphere around the droplet cannot be absorbed in the liquid.
- Constant and homogeneous pressure on all the domain.

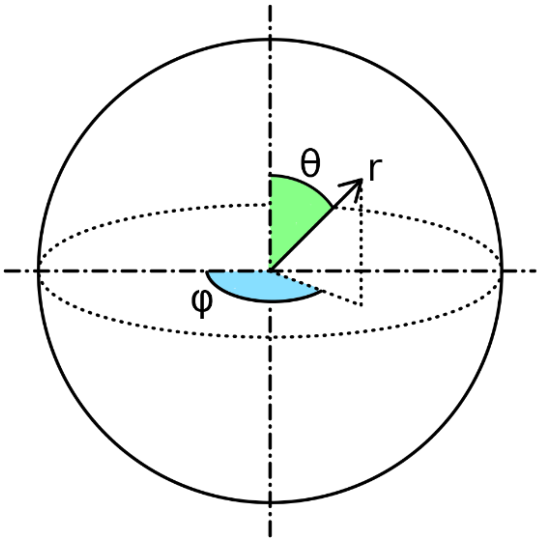

Figure 5.1: Polar coordinate system

5.2 Mathematical model

The model comprises two phases, a liquid phase representing the droplet, and a gas phase representing the surrounding environment. The presence of a fiber passing through the droplet can be considered in order to better simulate experimental setups where the droplet is anchored to one or more thin wires to keep it suspended steadily in the environment. However due to the impossibility of representing a fiber in a 1D system, only its contributions in the energy transport phenomena are included and no solid phase is added.

Mass and energy transport, chemical reactions, and thermodynamic equilibrium are described, for this purpose thermophoretic diffusion and radiative heat transfer are also taken in account.

The system is dived into:

- Center of the droplet
- Liquid Phase
- Liquid – gas interphase
- Gas Phase
- Gas phase outer boundary

5.2.1 Center of the droplet

Due to the spherical symmetry, no fluxes can occur at the center of the droplet, otherwise mass or energy would be generated or would disappear. For this reason, the following boundary conditions are applied to the center:

Heat equation

$$\left.\frac{\partial T_L}{\partial r}\right|_{r=0} = 0 \tag{5.1}$$

Where r is the radius and T_L is the temperature of the liquid.

Species diffusion

$$\left.\frac{\partial W_{L,i}}{\partial r}\right|_{r=0} = 0 \tag{5.2}$$

Where $W_{L,i}$ is the mass fraction of the *i-th* species in the liquid.

Mass conservation

$$v_L = 0 \tag{5.3}$$

Where v_L is the velocity of the liquid along the radial coordinate.

These conditions prevent any convective or diffusive flux to occur in the center of the droplet.

5.2.2 Liquid phase

For the liquid phase, the conservation equations are written as follows:

Continuity equation

$$\frac{\partial \rho_L}{\partial t} + \frac{1}{r^2}\frac{\partial}{\partial r}(r^2 \rho_L v_L) = 0 \tag{5.4}$$

This equation imposes the mass conservation in the liquid phase, and it describes how the liquid phase moves due to density variations that can be caused by variation of temperature (thermal expansion) and composition over time. The symbol ρ_L represents the liquid density.

Species equation

$$\rho_L \left(\frac{\partial W_{L,i}}{\partial t} + v_L \frac{\partial W_{L,i}}{\partial r}\right) = -\frac{1}{r^2}\frac{\partial}{\partial r}\left(r^2 j_{L,i}^d\right) + \dot{\Omega}_{L,i} \tag{5.5}$$

Where $j_{L,i}^d$ is the mass diffusion flux of the species *i-th* per unit of surface, and $\dot{\Omega}_{L,i}$ is the rate of formation of the species *i-th* due to chemical reactions. The rate of formation is evaluated summing the rate of production of the *i-th* species in all the NR_L liquid phase reactions.

The diffusion fluxes are computed using the Maxwell-Stefan theory. In this theory, differently from the Fick-based approach, the diffusion of the *i-th* species is considered as a function of the overall local composition of the mixture. Given a system composed by NSL liquid species, according to this method, the diffusion fluxes for each species can be computed by solving the following linear system, here presented in matrix form, of size NSL-1.

$$\boldsymbol{J}_L \cdot \boldsymbol{B} = -c_{L,tot} \boldsymbol{\Gamma} \frac{\partial \boldsymbol{x}}{\partial r} \tag{5.6}$$

Where $\boldsymbol{J}_L$ is the vector of the *i-th* species' molar diffusion fluxes, $c_{L,tot}$ is the liquid

concentration and $\frac{\partial \boldsymbol{x}}{\partial r}$ is the vector of the molar fractions' gradients along the radial coordinate.

The $\boldsymbol{B}$ matrix is defined as follow:

$$\begin{cases} B_{ij} = -x_i \left(\dfrac{1}{D_{i,j}} - \dfrac{1}{D_{i,NSL}} \right) & i \neq j \\ B_{ii} = \dfrac{x_i}{D_{i,NSL}} + \displaystyle\sum_{k=1,k\neq i}^{NSL} \dfrac{x_k}{D_{i,k}} \end{cases} \tag{5.7}$$

Where x_i is the molar fraction of the *i-th* species, and $D_{i,j}$ is the Stefan-Maxwell binary diffusion coefficient of the *i-th* species inside the *j-th* species. Such coefficients are computed using the equation proposed by Wesselingh and Krishna [63].

$$D_{ij} = \left(D_{i,j}^{inf}\right)^{\frac{1+x_j-x_i}{2}} \cdot \left(D_{j,i}^{inf}\right)^{\frac{1+x_j+x_i}{2}} \tag{5.8}$$

Where $D_{j,i}^{inf}$ is the infinite dilution diffusion coefficient of the *i-th* species into the *j-th* species, evaluated using the e Siddiqi-Lucas correlation [64].

The elements of the activity matrix $\boldsymbol{\Gamma}$ are defined as follow:

$$\Gamma_{i,j} = \delta_{i,j} + x_i \left(\frac{\partial \ln \gamma_i}{\partial x_j} \right)_{T,P,x_{k\neq j=1\ldots NSL-1}} \tag{5.9}$$

Where $\delta_{i,j}$ is the Kronecker delta, and γ_i is the activity coefficient of the *i-th* species.

As stated before, the system have a size of $NSL - 1$, hence all the diffusion fluxes but one are computed. The last diffusion flux is computed imposing that the total flux due to diffusion has to be null.

$$J_{NSL} = -\sum_{i=1}^{NSL-1} J_i \tag{5.10}$$

Energy balance

$$\rho_L c_{p,L}\left(\frac{\partial T_L}{\partial t}+v_L\frac{\partial T_L}{\partial r}\right)=\frac{1}{r^2}\frac{\partial}{\partial r}\left(r^2 k_L\frac{\partial T_L}{\partial r}\right)-\sum_{i=1}^{NSL} j_{L,i}^{d} c_{p,L,i}\frac{\partial T_L}{\partial r}-\sum_{i=1}^{NSL}\dot{\Omega}_{L,i}\hat{h}_{R,i}+S_L^f \qquad (5.11)$$

Where $c_{p,L}$ is the specific heat capacity of the mixture, $c_{p,L,i}$ is the specific heat capacity of the pure *i-th* species, k_L is the thermal conductivity of the mixture, $\hat{h}_{R,i}$ is the mass enthalpy of formation of the *i-th* species, and S_L^f is the term that takes in account the heat gain possibly due to the presence of one or more supporting fibers.

The contribution of the fiber is evaluated using the one-dimensional model proposed by Farouk and Dryer [65].

5.2.3 Interface

Mass conservation

$$\bar{\rho}_L\frac{dR_D}{dt}+\frac{R_D}{3}\frac{d\bar{\rho}_L}{dt}=-\rho_G^I\left(v_G^I-\frac{dR_D}{dt}\right) \qquad (5.12)$$

Where $\bar{\rho}_L$ is the average droplet density, R_D is the overall radius of the droplet, ρ_G is the density of the gas, and v_G is the velocity of the gas along the radial coordinate. The apex I indicates that the property is evaluated at the interface.

Thermodynamic equilibrium

$$T_L^I=T_G^I \qquad (5.13)$$

Where T_L is the liquid temperature, T_G is the gas temperature. This equation imposes the thermal equilibrium at the interface.

$$f_{L,i}^I=f_{G,i}^I \qquad (5.14)$$

Where $f_{L,i}$ and $f_{G,i}$ are the fugacity of the *i-th* species respectively in the liquid and in the gas phase. The fugacity is evaluated using a suitable equation of state (Raoult, Peng-

Robinson).

This equation imposes the chemical equilibrium at the interface, and it is used only for the species composing the liquid phase, indeed it is assumed that the species that compose the gaseous atmosphere cannot be adsorbed by the liquid. For such species the liquid side interface composition is null, and the gas side interface composition is evaluated by imposing that there is no flux of these species trough the interface. This condition is set by the following equation.

$$\left(v_G^I - \frac{dR_D}{dt}\right) W_{G,i}^I + j_{G,i}^I = 0 \tag{5.15}$$

Where $W_{G,i}$ is the *i-th* species mass fraction in the gas phase. The term $j_{G,i}$ represents the flux for unit of surface of the *i-th* species due to concentration-driven diffusion and Soret effect [66], computed as:

$$j_{G,i} = j_{G,i}^d + j_{G,i}^s \tag{5.16}$$

Where $j_{G,i}^d$ is the concentration-driven diffusion evaluated using the Fick's law, and $j_{G,i}^s$ is the flux due to the Soret effect.

The mechanical equilibrium is guaranteed by the hypothesis of constant and homogenous pressure along all the domain.

Species conservation

$$\left(v_L^I - \frac{dR_D}{dt}\right) W_{L,i}^I + j_{L,i}^{d\,I} = \left(v_G^I - \frac{dR_D}{dt}\right) W_{G,i}^I + j_{G,i}^I \tag{5.17}$$

Energy conservation

$$k_L^I \left.\frac{\partial T_L}{\partial r}\right|_{R_D} + \sum_{i=1}^{NSL} \left[\left(\dot{m}_{ev} W_{G,i}^I + j_{G,i}^I\right) \Delta H_{ev,i}\right] = k_G^I \left.\frac{\partial T_G}{\partial r}\right|_{R_D} + \dot{q}_{rad} \tag{5.18}$$

Where $k_G$is the thermal conductivity of the gas mixture, $\Delta H_{ev,i}$ is the enthalpy of vaporization of the *i-th* species, $\dot{q}_{rad}$ is the heat flux due to the radiation at the interface, and $\dot{m}_{ev}$ is the vaporization flux given by:

$$\dot{m}_{ev} = \rho_G^I \left(v_G^I - \frac{dR_D}{dt} \right) \tag{5.19}$$

For the evaluation of the gas radiation different methods are implanted in the solver (P1, SP3, discrete ordinate methods, optically-thin and analytical solution for gray gas). Non-gray radiation effects are modeled trough the Weighted Sum of Gray Gases model (WSGGM).

5.2.4 Gas phase

Continuity equation

$$\frac{\partial \rho_G}{\partial t} + \frac{1}{r^2}\frac{\partial}{\partial r}(r^2 \rho_G v_G) = 0 \tag{5.20}$$

Species equation

$$\rho_G \left(\frac{\partial W_{G,i}}{\partial t} + v_G \frac{\partial W_{G,i}}{\partial r} \right) = -\frac{1}{r^2}\frac{\partial}{\partial r}\left(r^2 j_{G,i}\right) + \dot{\Omega}_{G,i} \tag{5.21}$$

Where $\dot{\Omega}_{G,i}$ is the rate of formation of the species *i-th* due to chemical reactions in the gas phase.

Energy balance

$$\begin{aligned} \rho_G c_{p,G} \left(\frac{\partial T_G}{\partial t} + v_G \frac{\partial T_G}{\partial r} \right) = \frac{1}{r^2}\frac{\partial}{\partial r}\left(r^2 k_G \frac{\partial T_G}{\partial r} \right) + \\ - \sum_{i=1}^{NSG} j_{G,i} c_{p,G,i} \frac{\partial T_G}{\partial r} - \sum_{i=1}^{NSL} \dot{\Omega}_{G,i} \hat{h}_{R,i} - \nabla \dot{q}_{rad} + S_G^f \end{aligned} \tag{5.22}$$

Where $c_{p,G}$ and $c_{p,G,i}$ are the specific heat capacity of the gas mixture and the pure *i-th* species respectively, k_G is the thermal conductivity of the gas mixture, and S_G^f is the heat gain due to the fiber.

5.2.5 Outer boundary

At the external boundary of the gas phase the following boundary conditions are set.

$$\left.\frac{\partial T_G}{\partial r}\right|_{R_{MAX}} = 0 \tag{5.23}$$

$$\left.\frac{\partial W_{G,i}}{\partial r}\right|_{R_{MAX}} = 0 \tag{5.24}$$

5.3 Numerical implementation

The mathematical model consists of a differential algebraic equation system. Two sets of partial differential equations are defined, one for the liquid phase (equations (5.4), (5.5), (5.11)), and one for the gas phase (equations (5.20) – (5.22)). The two sets of differential equations are bound together by the algebraic equations describing the properties at the interface (equations (5.12) – (5.15), (5.17), (5.18)). For the partial differential equations, boundary conditions are set both to the droplet's center (equations (5.1) – (5.3)), and for the outer gas phase boundary (equations (5.23), (5.24)).

The numerical solution of the partial differential equations is performed through the method of lines, which consists in discretizing the spatial derivatives only, while leaving the time variable continuous. In this case, due to the one-dimensionality of the problem, that means to discretize the radial coordinates only.

5.3.1 Spatial discretization

The spatial discretization, using the Finite Difference Method (FDM), is applied to a moving one-dimensional grid.

The definition of the grid is a key aspect for the performance of the numerical algorithm, it has to be dense enough to guarantee an accurate approximation of the functions but increasing the number of points also increases the number of computations required.

Hence the grid has to be opportunely defined to reach the best compromise between simulation accuracy and performances. For these reasons, the grid is created by merging the two separate grids opportunely generated for the liquid and the gas phase. Because of the higher gradients in proximity of the interface, the grid points are not equally spaced, but they are denser near the surface and sparser towards the center of the droplet and especially the outer boundary. Such grids guarantee a sufficient number of points to cope with the high gradients while limiting the overall number of calculations by removing points where functions slopes are low.

Figure 5.2: Representation of droplet discretization

Particular attention has to be paid to the liquid phase grid, in fact, the presence of species with high difference in vapor pressure leads to extreme composition gradients near the interface. A broad set of grids was tested in order to find the best performing one, the set was composed by grids with equidistant points, equivolumes grids and custom defined grids. All types of grids were tested with different number of points spanning from 30 to 1000. The study showed that the overall best grid was a custom grid with 175 points. Such grid was generated by defining the desired point spacing in relative radial coordinate (defined as radial coordinate divided by the initial droplet's radius) at the interface and then computing all the subsequent point spacing as follows.

$$\Delta r_i = \Delta r_{i-1}^k \tag{5.25}$$

Where Δr_i is the distance in relative radius between the *i+1-th* point and the *i-th* point, and k is a user defined constant. The aforementioned grid was generated by setting the interface side grid spacing as $\Delta r_0 = 10^{-5}$ and the constant as $k = 1.05$. Nonetheless, a per-case grid choice may be still necessary to cope with issues of specific simulations.

Since the droplet's surface moves over time, initially enlarging due to thermal expansion, then shrinking due to evaporation, the grid must change over time in order to keep the zone with denser point in proximity of the interface. For this reason, at each iteration both the liquid phase grid and the gas phase grid are updated by stretching the points in such a way that the first and last point of the liquid grid coincide with the interface and the droplet's center, while the first and the last points of the gas grid coincide with the interface and the gas outer boundary. All the remaining points are moved so that their relative position remains the same.

5.3.2 Numerical algorithm

Once the grid is defined, the partial derivatives over the radius are discretized using a fist-order discretization, for this purpose the user can choose between upwind, backward, forward, or centered scheme.

In a simulation involving NSL liquid phase species, and NSG gas phase species, that uses a grid with NPL points in the liquid phase grid and NPG points in the gas phase grid, the total number of equations of the DAE system n_E is given by the following equation.

$$n_E = NPL(NSL + 3) + 5 + NPG(NSG + 3) \tag{5.26}$$

It is clear that even with simplified kinetic schemes the total number of equations can easily fall in the order of several thousands. This, in conjunction with the high nonlinearity of the transport equations and the intrinsic stiffness of the problem, poses

several numerical challenges. For this reason a DAE solver based upon the BzzDae solver [67] [68], using a backward differentiation formula (BDF) method [69], was adopted, indeed its ability in handling stiff problems makes it suitable for this task.

6 Simulations

In this chapter the simulations of droplet pyrolysis executed with the developed code are presented. As it will be shown, the used assumptions limit the ability of the model to quantitatively represent the real case observations. Anyway, the software proved to be a useful tool for understanding some core phenomena involved in the pyrolysis of heavy hydrocarbons.

6.1 Surface char accumulation

Accumulation of heavy compounds on the surface of the droplet is a phenomenon well known to occur during the pyrolysis and combustion of heavy hydrocarbons. In case of heavy fuel oils, the superficial layer of heavy hydrocarbons leads to the formation of the cenosphere [29, 70], a porous, solid, hollow shell that endures the pyrolysis/combustion process and can be found in the flue gases. In pyrolysis processes the cenosphere is mostly composed by solid carbonaceous residue mixed with smaller quantities of mineral ashes. Under oxidative conditions the carbonaceous compounds can participate to heterogeneous combustion reactions and thus their final quantity can be lower than in comparable pyrolytic conditions. Anyway, large quantities of unreacted carbon can be still found in the flue gases of heavy fuel oil burners, mainly because of the low speed of the solid carbon oxidation reactions.

High speed imaging of heavy fuel oil combustion provided a clear observation of the dynamic of formation of cenospheres [29]. The experiments showed that after the initial evaporation of the light compounds contained in the HFO, as soon as the temperature in the droplet allows for the cracking reactions, a solid superficial layer forms and starts to thicken. Meanwhile, the enclosed liquid keeps pyrolyzing releasing gas products. The reacting liquid keeps losing mass and volume causing the droplet to shrink. The solid layer at first follows the liquid surface dragged by surface tension thus compressing, then once it is rigid enough it partially detaches from the liquid phase and it stops shrinking. The porosity of the solid shell allows for the pyrolysis products to escape the droplet, however the resistance to flow can lead to a buildup of pressure inside the droplet high enough to deform and eventually cause the rupture of the cenosphere. After the flame is

extinguished the remaining cenosphere generally is a heavily deformed hollow sphere with one or more holes in it, however smaller droplets can generate almost perfectly spherical shells.

In the literature there is agreement about the critical role that the accumulation of heavy compounds on the droplet surface plays in the generation of the cenosphere. However little efforts were made in describing the phenomena that lead to the accumulation of char on the surface. The common belief is that char builds upon the surface because the higher superficial temperature causes a faster pyrolysis of the outer layers of the droplet, thus more residue is formed near the surface. Simulations made with the model developed in this work showed that the accumulation of heavy compounds over the droplet surface occurs even when no appreciable temperature gradient is present over the droplet surface.

Another explanation of this phenomenon that can be found in the literature is that the evaporating light compounds lower their superficial concentration thus raising the concentration of low volatility species. This only partially uncovers the problem; indeed, it does not explain why of all the non-evaporating species remaining in the liquid phase, only the heavier accumulates over the surface. If the evaporation of the light compounds is the only driving force of the heavy compound surface buildup, the ratio between heavy compounds should remain equal along the droplet. On the contrary, in experimental evaluations a higher char/asphaltene ratio is observed on the surface rather than in the center of the droplet.

In order to facilitate the comprehension of the involved phenomena, the simulations showed in this section are performed using a simplified kinetics scheme. Only the reference species Asph1 is taken in account, and its decomposition reaction was simplified lumping together all the light products into a single one. The simplified kinetic scheme is shown in Table 4. This allows for easier mathematical description of the phenomena and lower computational cost of the simulations without losing generality.

Table 4: Simplified kinetic scheme

	k_0 [1/s]	E_{att} [cal/mol]
Asph1 → 5 C_6H_6 + 30 CHAR	$5.0 \cdot 10^{13}$	58000

Simulations of pyrolysis of a 1.05 mm droplet of pure Asph1 were performed. The initial droplet and gas phase temperatures are set to 300 K and 850 K respectively. The surrounding gaseous environment is composed by pure nitrogen. The profiles of temperature and char mass fraction along the droplet cross section are shown in Figure 6.1. Some major characteristics can be noted:

- The droplet initially swells due to thermal expansion, then it shrinks due to the evaporation of the light species produced by the reaction.
- No appreciable temperature gradient is present along the radial coordinates while the droplet reacts. The characteristic time of the heat transfer is much higher than the characteristic time of the reaction.
- The char accumulates over the surface.

This simulation clearly shows that char accumulation over the surface can occur even when the droplet is at almost homogeneous temperature.

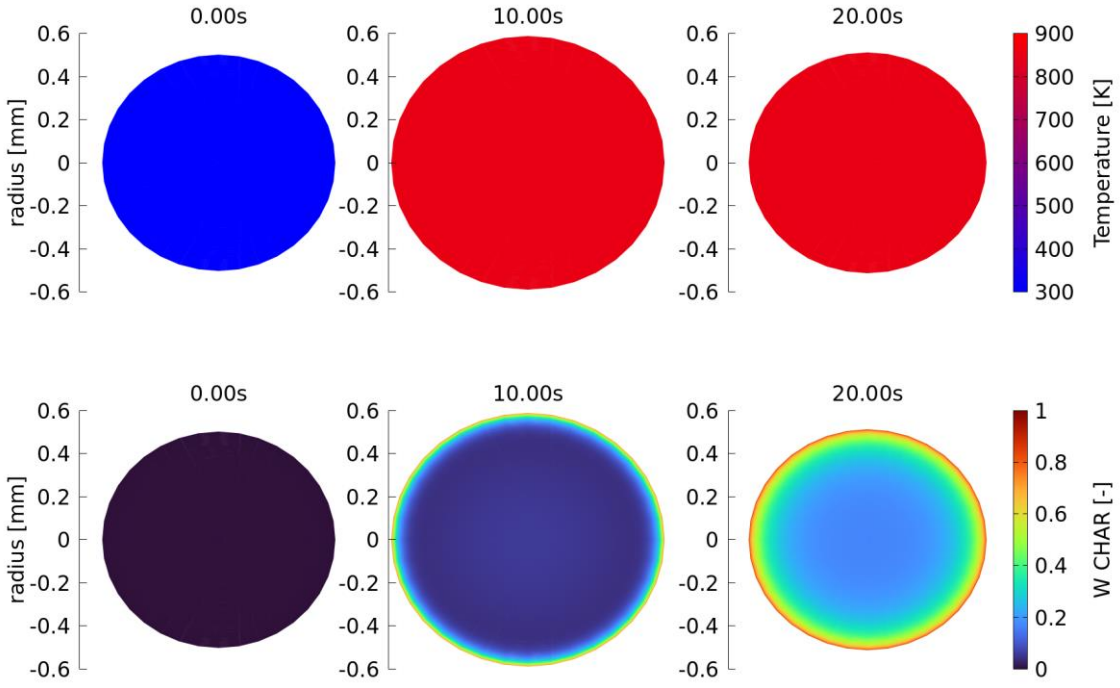

Figure 6.1: Temperature and char mass fraction profiles

The phenomena that lead to the accumulation of the char over the surface can be clearly understood if the process of evaporation is analyzed in detail. When the light compound is formed, it starts to evaporate due to the high temperature of the droplet, this leads to a diffusive flux of the light compound towards the surface. The evaporation the of light compound generates a net relative velocity between the liquid and the surface, indeed, once the droplet reached the maximum temperature and there is no more thermal expansion, the droplet starts to shrink, thus the surface moves towards the liquid phase. Figure 6.2 shows that this behavior is represented in the simulation. In this figure the surface velocity and the liquid absolute velocity at the interface are depicted. As it can be seen, the surface speed is always lower than the liquid speed at the interface. This means that relatively to the surface, the liquid phase has a positive velocity directed outside the droplet. This generates a convective flux exiting the liquid phase. It is also interesting to note that after around 5 seconds, both the surface velocity and the liquid absolute velocity at the interface become negative, thus directed towards the center of the droplet. This happens because at this time the droplet has reached a steady temperature, hence the thermal expansion does not occur anymore. Moreover, because of the reaction, some of the asphaltene reference species is converted into the denser char, hence the liquid phase starts to contract. This generates a net absolute liquid velocity directed towards the center of the droplet. The variation of the average density of the liquid phase is represented in Figure 6.3. Despite the liquid phase has an absolute negative speed when the droplet starts to contract, it still keeps a positive relative velocity with respect of the surface, hence the exiting convective flux is preserved.

The evaporating flux of the *i-th* species is described by equation (5.17), such equation can be expressed as follows:

$$v_L^{rel}\, W_{L,i}^{I} + j_{L,i}^{d\,I} = \dot{m}_{ev,i} \tag{6.1}$$

Where v_L^{rel} is the relative velocity between the liquid and the surface, considered positive when the generated convective flow exits the droplet, $\dot{m}_{ev,i}$ is the evaporating flux for unit of surface of the *i-th* species leaving the droplet. The first addendum of the left-hand side of the equation represents the convective contribution to the flux of the *i-th* species while the second addendum represents the diffusive contribute.

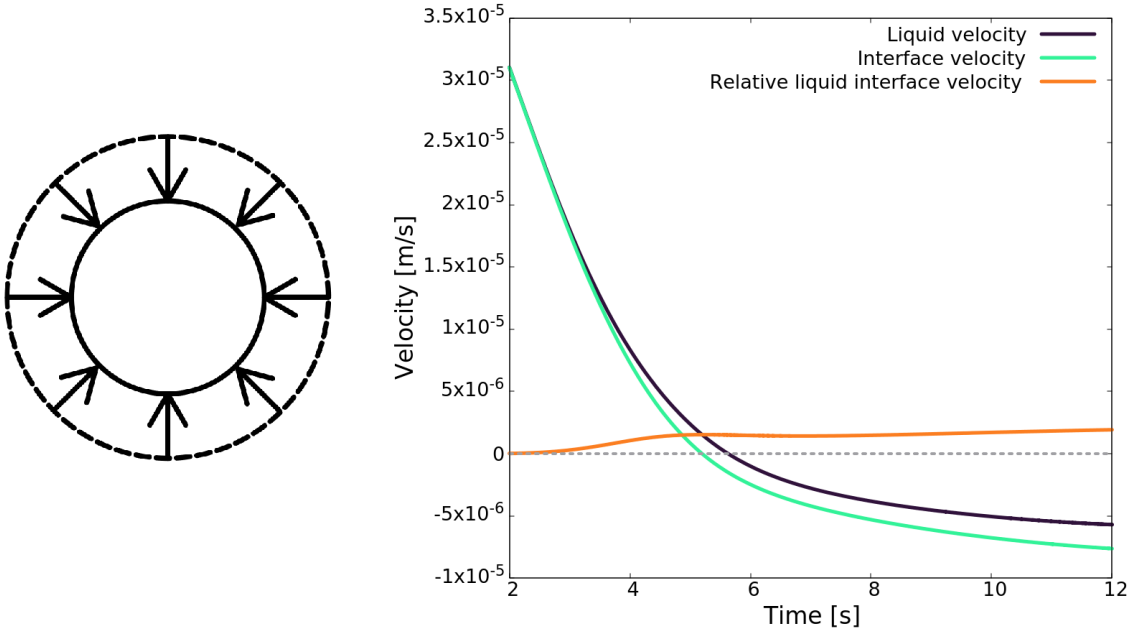

Figure 6.2: Droplet shrinkage and relative liquid-surface velocity at the interface

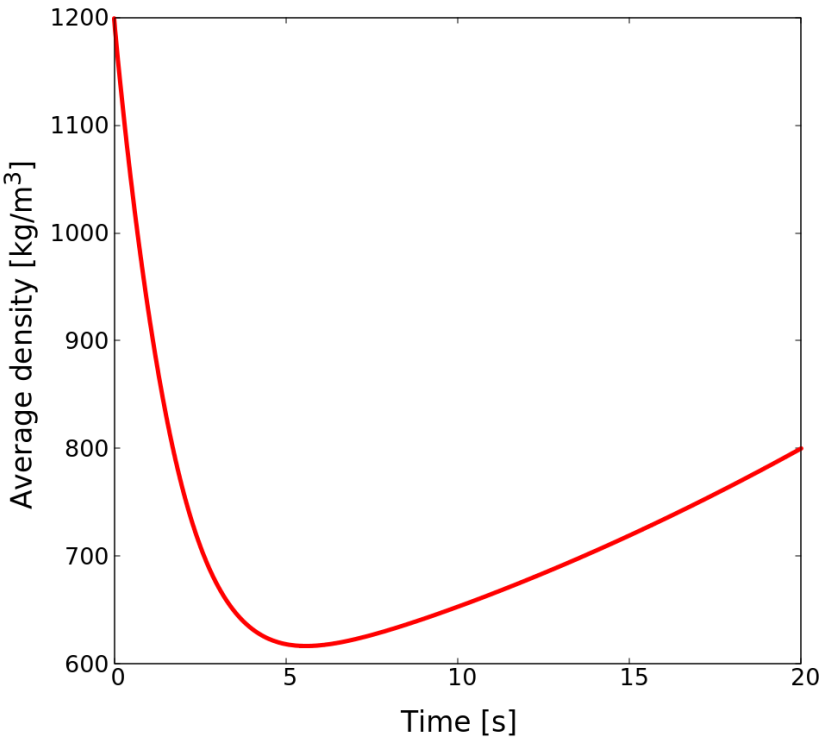

Figure 6.3: Average droplet density over time

The evaporative flux of the char is nil, while the evaporative flux of Asph1 can be neglected at these temperatures, hence for both species the sum of convective flux and diffusive flux at the surface must be equal to zero.

$$v_L^{rel}\, W_{L,i}^I + j_{L,i}^{d\,I} = 0 \tag{6.2}$$

$$v_L^{rel}\, W_{L,i}^I = -j_{L,i}^{d\,I} \tag{6.3}$$

If the convective term, generated by the relative liquid-surface velocity, is exiting the droplet, in order to achieve zero flux at the surface, the diffusive flux at the surface must have the same modulus and enter the droplet. This is obtained only if the diffusive flux is in the direction of the center of the droplet. If a Fick law diffusion is considered, this can be achieved only if the gradient of the molar fraction of the *i-th* species over the radius is positive at the surface, hence the concentration of the *i-th* species must be higher at the surface than in the center of the droplet. Moreover, the lower the diffusion coefficient of a species the higher the gradient must be in order to generate the required counter-diffusion flux. In general, the heavier a hydrocarbon is the lower its diffusion coefficient is. This is one of the reasons for which heavy hydrocarbons accumulate on the surface during the droplet pyrolysis.

This phenomenon can be easily explained if it is assumed that the surface act as a sieve, allowing the light, evaporating compounds to pass through while blocking the heavier, non-evaporating species. When the mixture flows towards the surface, the heavier molecules accumulate over the sieve and the concentration reached at the surface is inversely proportional to the ability of the species to diffuse towards the center of the droplet. A simple representation of this model is shown in Figure 6.4.

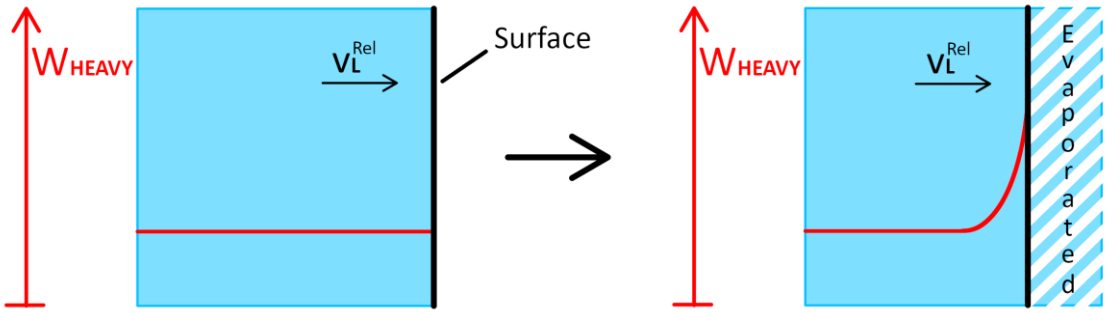

Figure 6.4: Sieve model

On top of this phenomenon, also friction between different diffusing species contributes to the accumulation of heavy compounds on the droplet surface. Indeed, in real-case diffusion, the diffusive flux of one species is not only dependent on the gradient of concentration of such species, but also depends on the overall mixture composition and on the diffusive fluxes of other species. These contributions are taken into account in the model by using a Maxwell-Stefan diffusion law. Such law considers both the diffusion flux due to the concentration gradients and the diffusion due to the friction between diffusing species. The diffusive flux of char can be easily represented by solving the system shown in Equation (5.6). Thanks to the use of a simplified, 3-species kinetic mechanism, the involved mathematic becomes much easier. Having only 3 species the system is composed by two equations. It was decided to compute the diffusive fluxes of the benzene and the char solving the system, while the diffusion flux of the Apsh1 can be computed imposing that the sum of all the diffusive fluxes must equal to zero. Under these conditions the vector of the diffusive fluxes and the vector of the concentration gradients are expressed as follows.

$$\boldsymbol{J}_L = \begin{bmatrix} J_{C6H6} \\ J_{CHAR} \end{bmatrix}$$
$$\frac{\partial \boldsymbol{x}}{\partial r} = \begin{bmatrix} \frac{\partial x_{C6H6}}{\partial r} \\ \frac{\partial x_{CHAR}}{\partial r} \end{bmatrix} \tag{6.4}$$

The elements of the matrix $\boldsymbol{B}$ are shown below.

$$\begin{aligned} B_{1,1} &= \frac{x_{C6H6}}{D_{C6H6,Asph1}} + \frac{x_{CHAR}}{D_{C6H6,CHAR}} + \frac{x_{Asph1}}{D_{C6H6,Asph1}} \\ B_{1,2} &= -x_{C6H6}\left(\frac{1}{D_{C6H6,CHAR}} - \frac{1}{D_{C6H6,Asph1}}\right) \\ B_{2,1} &= -x_{CHAR}\left(\frac{1}{D_{C6H6,CHAR}} - \frac{1}{D_{CHAR,Asph1}}\right) \\ B_{2,2} &= \frac{x_{CHAR}}{D_{CHAR,Asph1}} + \frac{x_{C6H6}}{D_{C6H6,CHAR}} + \frac{x_{Asph1}}{D_{CHAR,Asph1}} \end{aligned} \tag{6.5}$$

The liquid phase is here considered as an ideal mixture, hence the matrix $\boldsymbol{\Gamma}$ is a two by two identity matrix. In order to better highlight the contributes of the species concentration gradients on the diffusive fluxes, the system shown in Equation (5.6) is rewritten in the following form.

$$\boldsymbol{J}_L = -c_{L,tot}\boldsymbol{B}^{-1}\boldsymbol{\Gamma}\frac{\partial \boldsymbol{x}}{\partial r} \tag{6.6}$$

For the sake of a simpler representation of the equations, the following matrix is defined.

$$\boldsymbol{D}^{\boldsymbol{eff}} = \boldsymbol{B}^{-1}\boldsymbol{\Gamma} \tag{6.7}$$

Its elements are shown below. A nomenclature of the matrix's elements that better represents their physical meaning is also proposed.

$$\begin{aligned} D_{1,1}^{eff} &= D_{C6H6,C6H6}^{eff} = \frac{D_{C6H6,Asph1}(x_{C6H6}D_{CHAR,Asph1} + (1-x_{C6H6})D_{C6H6,CHAR})}{x_{C6H6}D_{CHAR,Asph1} + x_{CHAR}D_{C6H6,Asph1} + x_{Asph1}D_{C6H6,CHAR}} \\ D_{1,2}^{eff} &= D_{C6H6,CHAR}^{eff} = \frac{x_{C6H6}D_{CHAR,Asph1}(D_{C6H6,Asph1} - D_{C6H6,CHAR})}{x_{C6H6}D_{CHAR,Asph1} + x_{CHAR}D_{C6H6,Asph1} + x_{Asph1}D_{C6H6,CHAR}} \\ D_{2,1}^{eff} &= D_{CHAR,C6H6}^{eff} = \frac{x_{CHAR}D_{C6H6,Asph1}(D_{CHAR,Asph1} - D_{C6H6,CHAR})}{x_{C6H6}D_{CHAR,Asph1} + x_{CHAR}D_{C6H6,Asph1} + x_{Asph1}D_{C6H6,CHAR}} \\ D_{2,2}^{eff} &= D_{CHAR,CHAR}^{eff} = \frac{D_{CHAR,Asph1}(x_{CHAR}D_{C6H6,Asph1} + (1-x_{CHAR})D_{C6H6,CHAR})}{x_{C6H6}D_{CHAR,Asph1} + x_{CHAR}D_{C6H6,Asph1} + x_{Asph1}D_{C6H6,CHAR}} \end{aligned} \tag{6.8}$$

The diffusive fluxes can be computed solving the following system.

$$\boldsymbol{J}_L = -C_{TOT}\boldsymbol{D}^{\boldsymbol{eff}}\frac{\partial \boldsymbol{x}}{\partial r} \tag{6.9}$$

Hence the diffusive flux of the char can be evaluated as shown.

$$J_{CHAR} = -C_{TOT}D^{eff}_{CHAR,CHAR}\frac{\partial x_{CHAR}}{\partial r} - C_{TOT}D^{eff}_{CHAR,C6H6}\frac{\partial x_{C6H6}}{\partial r} \tag{6.10}$$

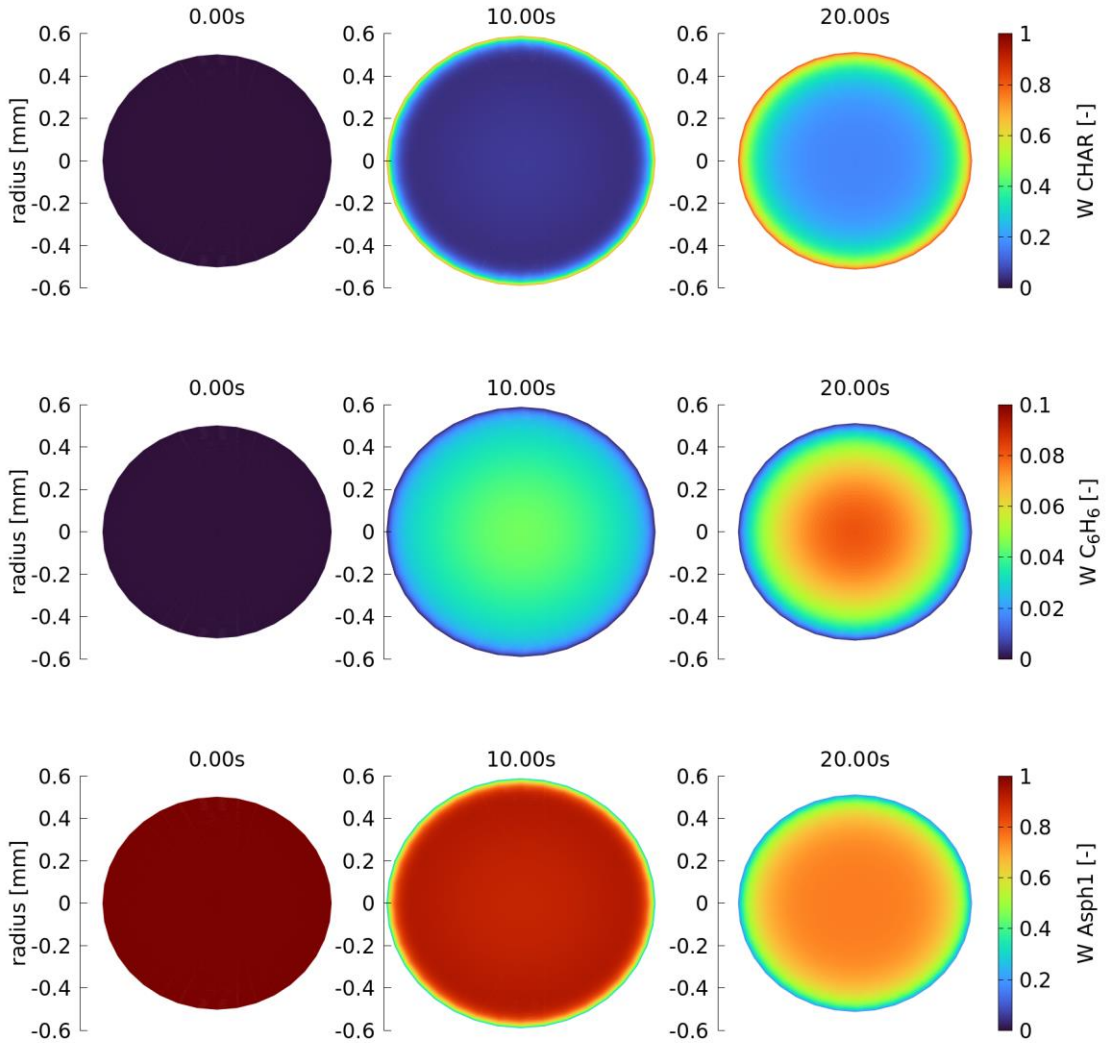

Figure 6.5: Mass fraction of char, benzene, and reference species

It is trivial to distinguish between the diffusive contribution of the species concentration gradient, represented by the first addendum of the right-hand side of Equation (6.10), and the diffusive contribution of the friction with other diffusing species, represented by the second addendum. The value of $D_{CHAR,C6H6}^{eff}$ over time and the droplet radius is shown in Figure 6.6. It can be seen that the effective diffusion coefficient that represents the friction with the other species is positive for almost all the domain, in particular it is always positive near the surface. This means that the diffusive flux of the char is biased to follow the diffusive flux of the benzene. Indeed, the benzene has a lower diffusion coefficient in char rather than in the asphaltene reference species, hence, when benzene diffuses towards the surface, it tends to preferentially drag the char to the surface.

The phenomenon of diffusion due to friction is particularly important under these conditions, indeed the char has extremely low diffusion coefficients, thus it hardly diffuses under concentration gradients while it is easily dragged by other diffusing species. This can be clearly noted in Figure 6.7, where it is shown that the friction term is greater than the concentration gradient term for most of the domain. The predominance of the friction diffusion term can lead to the so-called uphill diffusion regime [71], a condition in which a species diffuses from a low concentration area to a high concentration area. The char mass fraction profile is shown in Figure 6.8, the subset of the domain in which there is an uphill diffusion regime is highlighted.

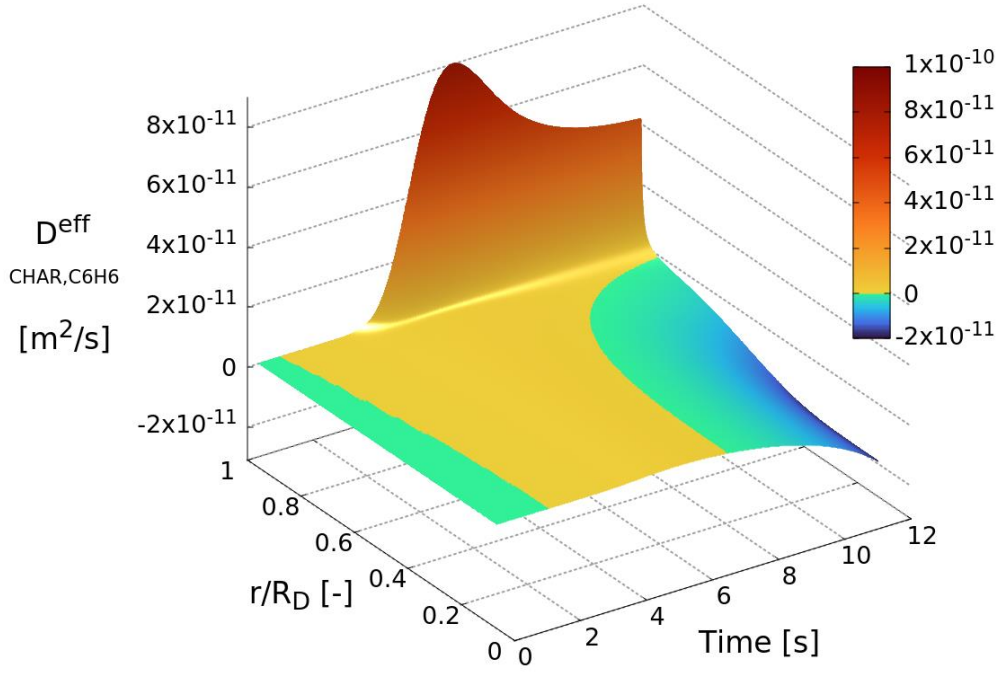

Figure 6.6: Effective Char-C_6H_6 diffusion coefficient

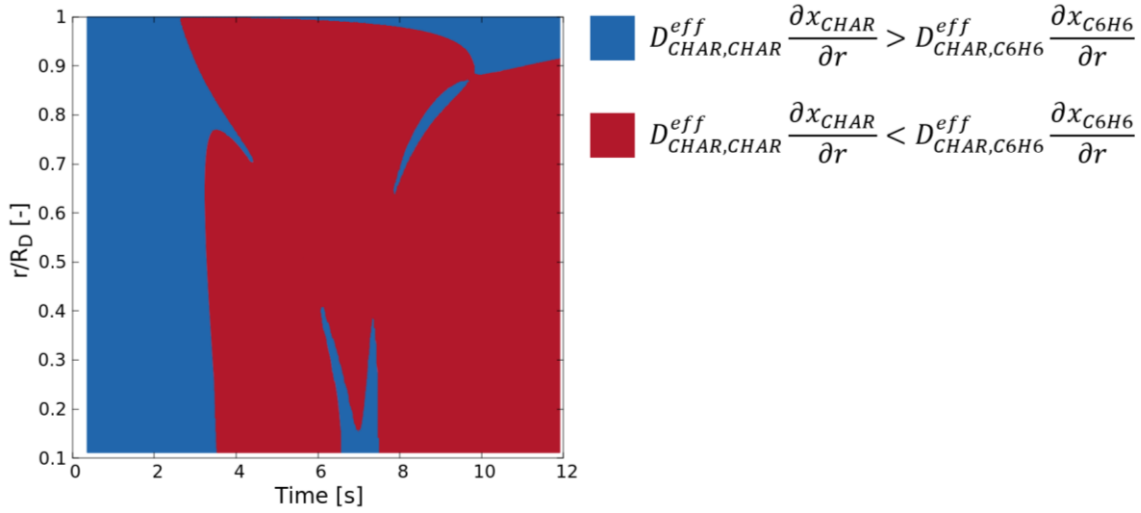

Figure 6.7: Concentration diffusion vs. friction diffusion

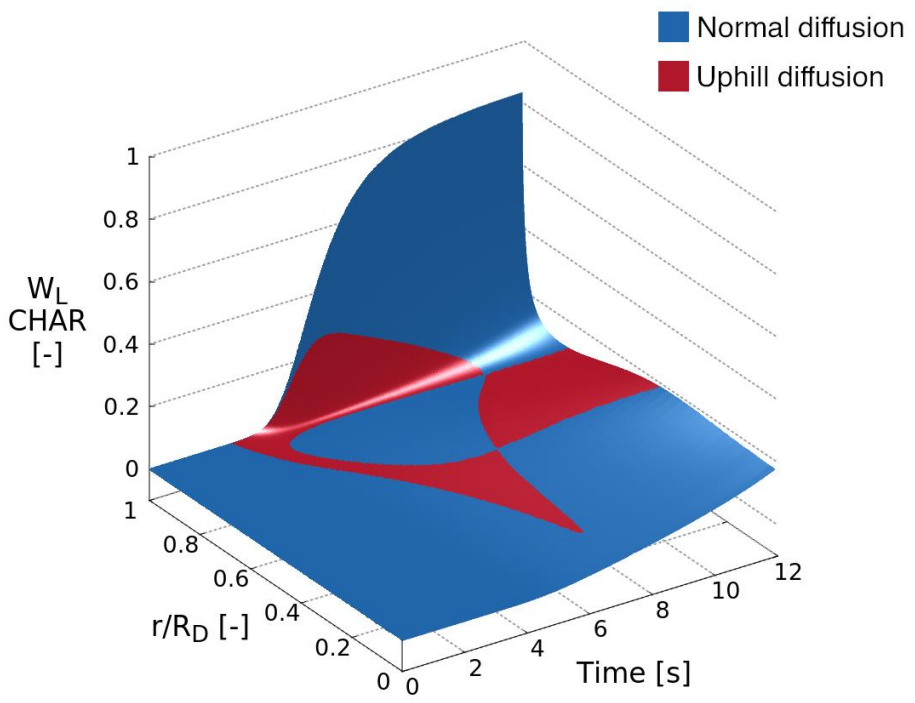

Figure 6.8: Char mass fraction, and uphill diffusion

In conclusion, the results of this simulation clearly shows that the accumulation of char on the surface is driven by diffusive phenomena. Two different contributions are detected:

- Accumulation due to superficial counter-diffusion of non-evaporating species.
- Accumulation due to drag of low diffusivity compounds by evaporating species.

A proof that these phenomena are the main causes for the formation of a superficial shell of heavy species can be obtained by proving that eliminating these driving forces no accumulation occurs. In Figure 6.9 the results of a simulation in which all the operative conditions are the same of the previous simulation, but the benzene was not allowed to evaporate, are shown. Under this assumption no convective flux occurs on the surface and no diffusive flux of benzene is generated inside the droplet either. In this case the char is homogeneously distributed inside the droplet and no appreciable superficial concentration gradient can be observed.

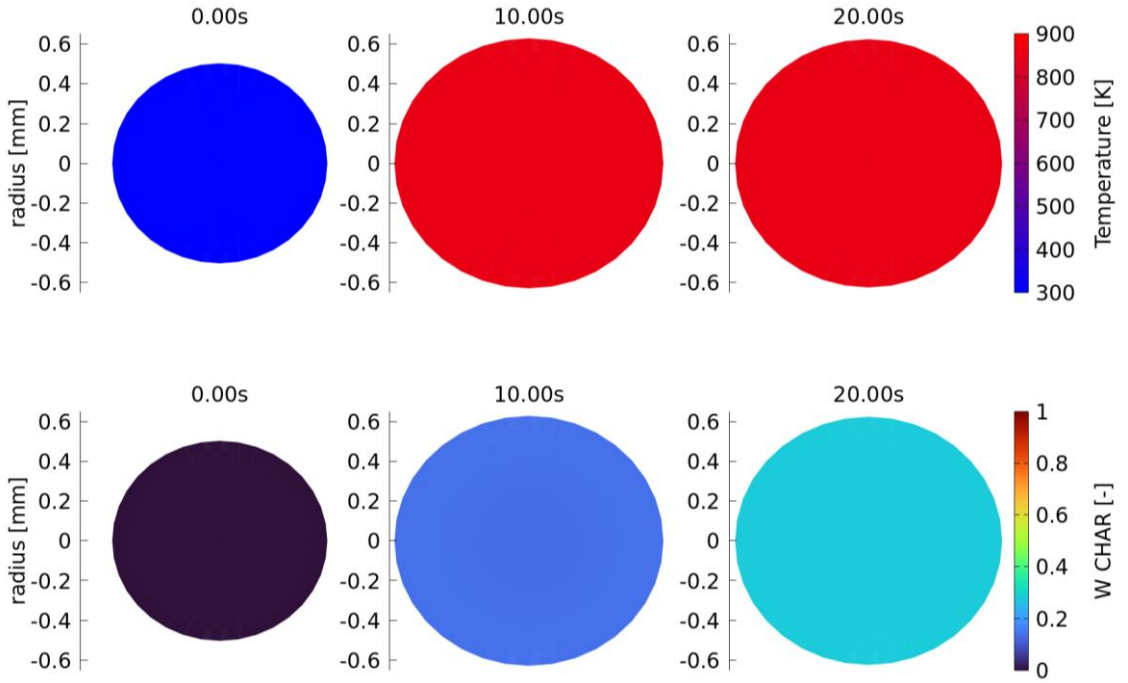

Figure 6.9: Temperature and char mass fraction profiles - No C_6H_6 evaporation

6.2 Evaporation simulation

The adopted model does not consider the formation of bubbles inside the droplet due to the presence of trapped high volatility compounds. In this section the magnitude of the errors caused by such assumption is analyzed.

In experimental setups it is observed that HFO droplets suspended in high temperature environments tend to form bubbles inside the liquid phase [29, 72, 73]. This phenomenon is caused by the evaporation of light compounds initially present in the heavy fuel oil and the small hydrocarbons produced by the thermal cracking reactions. In particular, the bubbles nucleate when the pressure of the mixture inside the droplet is high enough to overcome the atmospheric pressure and the liquid surface tension [74]. The contribute of the surface tension on the pressure threshold for the bubble generation is difficult to estimate, indeed it is heavily influenced by the local composition of the mixture and by the presence of impurities that can act as nucleation sites.

The bubbles formation is highly enhanced by the presence of heavy compounds, indeed when such compounds accumulate over the surface, they form an external viscous layer that inhibits the diffusion of light compounds outside the droplet. The decrease of

superficial evaporating flux also decreases the droplet heat removal thus causing the droplet to reach higher temperatures and higher mixture vapor pressure in the inner layers.

The formation of bubbles causes the droplet to considerably swell, greatly affecting mass and energy transport phenomena. Moreover, when the bubbles burst releasing the gases into the environment surrounding the droplet, they can introduce violent mixing in the liquid phase due to the rapid deformation of the droplet. All these phenomena have large contributes on the overall pyrolytic behavior of the droplet.

Here the results of a simulation are presented. The operative conditions are shown in Table 5. The pyrolysis reaction of the asphaltene reference species is suppressed in order to limit the number of involved species and to simplify the comprehension of the problem. The composition of the droplet was selected in order to mimic the evaporation of heavy fuel oils, where compounds with highly different vapor pressure are mixed together. The properties related to evaporation of Asph1, and methylnaphthalene are compared in Table 6, while in Figure 6.10 the values of the vapor pressure for the two species are shown.

Table 5: Evaporation simulation operative conditions

Initial diameter		1.005	[mm]
Initial droplet temperature		300	[K]
Initial gas temperature		800	[K]
Droplet composition	Asph1	0.1	wt
	$C_{10}H_7CH_3$	0.9	wt
Gas composition	N_2	1.0	wt
Pressure		1.0	[bar]

Table 6: Properties of reference species and methylnaphthalene

	Asph1	$C_{10}H_7CH_3$	
T_{NBP}	1181.4	514.2	[K]
T_C	1338.1	761.0	[K]
P_C	6.58	32.5	[atm]

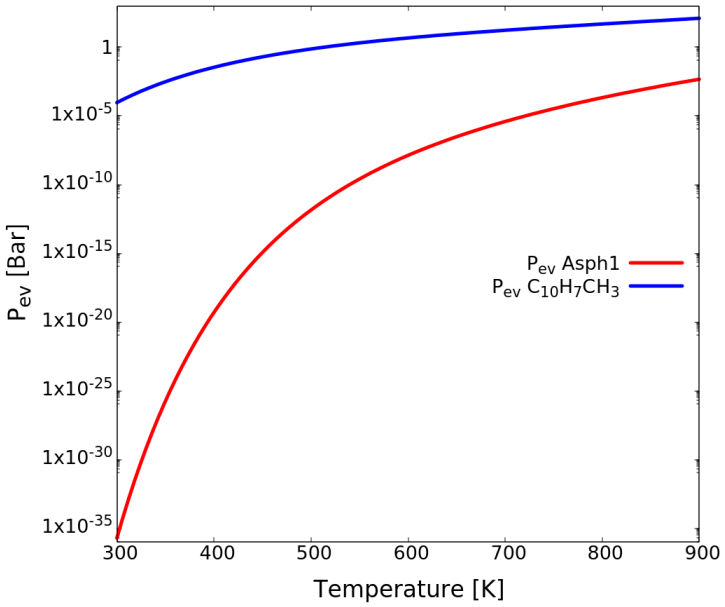

Figure 6.10: Vapor pressure of methylnaphthalene and Asph1
in the temperature range of the simulation

In Figure 6.11 the mass fraction profiles of the two species are showed. As expected, in a short time the superficial methylnaphthalene evaporates leaving an outer shell composed by almost pure asphaltene. The rapid superficial evaporation is completed after about 1 second, after that the evaporation of the light compound becomes slower because of the diffusion limitation caused by the outer shell rich in asphaltene. The evaporation becomes faster only when the droplet raises in temperature and the viscosity of the asphaltene reference species decreases considerably.

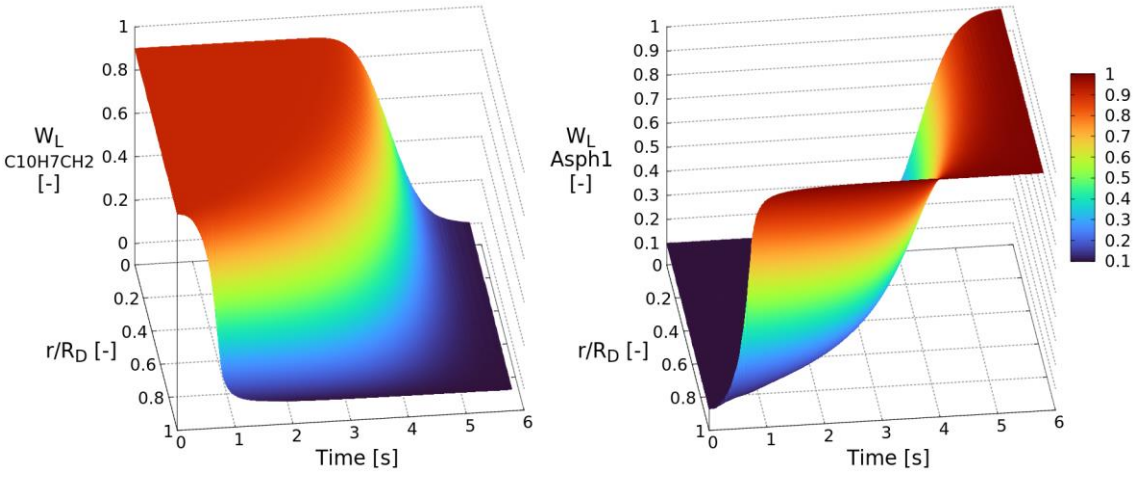

Figure 6.11: Asph1 and $C_{10}H_7CH_3$ mass fractions

As it was stated before, the slowdown of the evaporation causes the droplet to reach high temperatures. This phenomenon can be observed in Figure 6.12, where the temperature of the drolpet is shown. It can be observed that right before the 1s time mark the increase of superficial temperature slows down due to the evaporation of light compounds, when the the superficial concentration of methylnaphthalene reaches the minimum the superficial temperature return to raise at a higher rate.

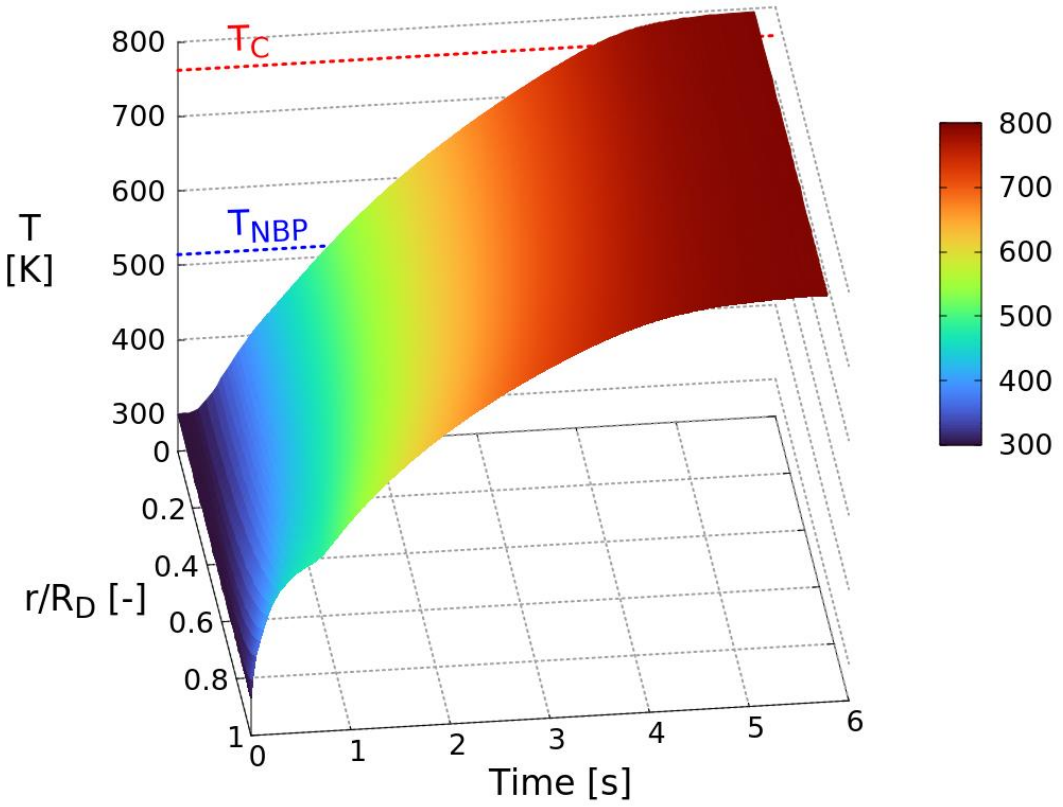

Figure 6.12: Temperature profile. (T_C and T_{NBP} are referred to $C_{10}H_7CH_3$)

In Figure 6.13 the mixture vapor pressure is shown. As it can be seen, the vapor pressure inside the droplet reaches extremely high values, with a maximum of 27.3 bar. This is due to the combination of high internal temperature and high internal concentration of light compound. This behavior is not representative of a real case scenario, bubbles should generate inside the liquid phase as soon as the mixture vapor pressure becomes slightly higher than the atmospheric pressure. The bubbles, adding more gas-liquid interface

surface, increase the evaporation rate thus decreasing both the droplet temperature and the liquid phase light compound concentration.

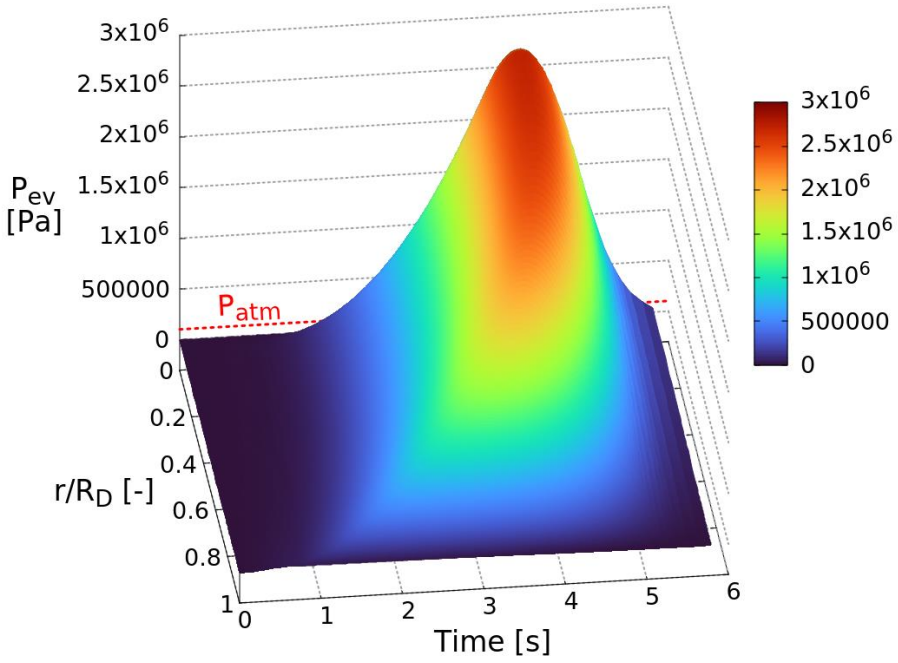

Figure 6.13: Mixture vapor pressure

The inability of the model to represent the formation of bubbles clearly is a big limitation. Without taking into account the generation of bubbles it is not possible to achieve quantitative prediction of the pyrolysis process. When a better understanding of the nucleation and bubble disruption/collapse processes in heavy fuel oils will be achieved, future works could improve the model in order to consider such phenomena.

7 Conclusions and outlooks

In this work two major achievements are presented, the first one is a methodology for the prediction of asphaltenes surrogates thermophysical properties, the second one is a model for the pyrolysis of isolated asphaltene droplets coupled with the relative numerical code. These are the first steps in the development of an accurate predictive model for the description of high temperature behavior of heavy fuel oils. Indeed, the continuous increase in world energy demand in conjunction with the depletion of the lighter crude oil reserves are making heavy fossil fuels continuously more important in the energetic market. This project is driven by the need for a better understanding of such phenomena with the final goal of developing new, efficient, and clean technologies for the upgrade and utilization of heavy oil fractions. The asphaltene fraction was the main focus of the work because it is deemed to be the main cause of the major problems related to HFOs utilization, like generation of solid residue and pollutants emission.

The model still shows significant limitations and at the time it cannot be used for quantitative prediction of the asphaltene pyrolysis process. The lack of a proper solid phase and of bubbles generation are the main causes of the discrepancies between the simulations results and the experimental observation. However, the results obtained by the simulations proven to be useful for understanding some of the phenomena involved in the subject of study. The findings about the heavy compounds accumulation on the droplet surface are of particular interest. Despite this phenomenon is of critical importance for the formation of solid particles during the combustion of HFOs, it was never studied in depth. The results of the simulations made it possible to identify the driving forces of this phenomena and to detect which of them are the most relevant. The analysis of the data shows that the temperature gradient, deemed to be the main causes of the cenosphere formation, actually can have a negligible contribution. Instead, it has been proven that solid accumulation on the surface is mainly driven by diffusion. On top of giving a better comprehension of the overall process, these observations can provide useful guidelines for the development of future, more sophisticated models. Indeed, this work reveals the importance of the friction between different diffusing species, implying that it should be not neglected in future works.

Future works could improve both the methodology for the prediction of the reference species properties and the model. An extensive experimental campaign will be necessary, indeed, now, the data required to understand how to model complex phenomena like the solid and bubbles nucleation are not available in the literature for HFOs. Ad hoc experimental evaluation of some of the asphaltenes properties required by the model could also greatly improve the overall accuracy of the simulations.

8 Appendices

8.1 Appendix A – Methodology validation

Hexatriacontylbenzene

Property		Predicted	Experimental
T_C	[K]	919.4	1067.6
P_c	[bar]	4.30	4.13
T_{NBP}	[K]	834.5	804.6

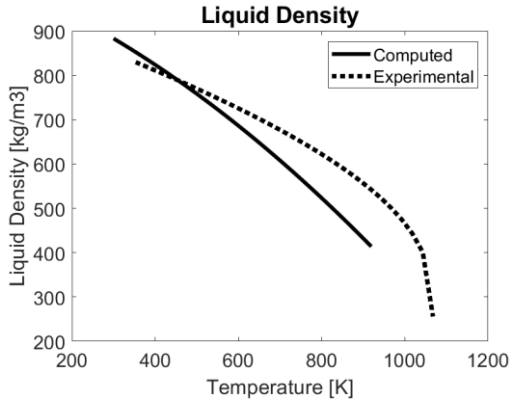

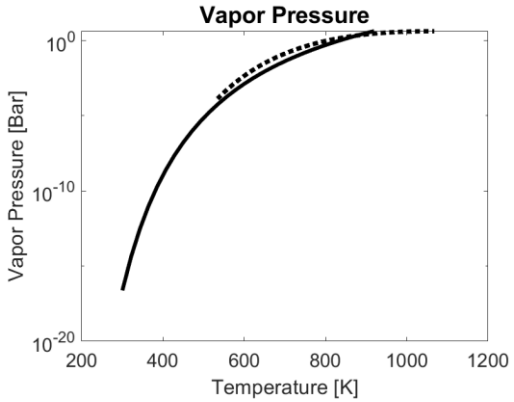

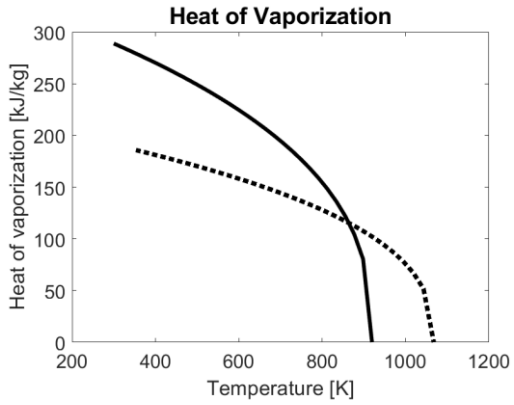

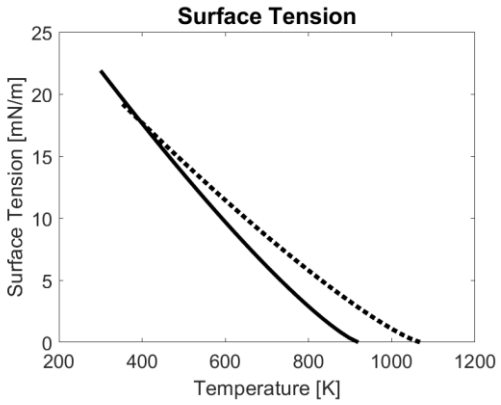

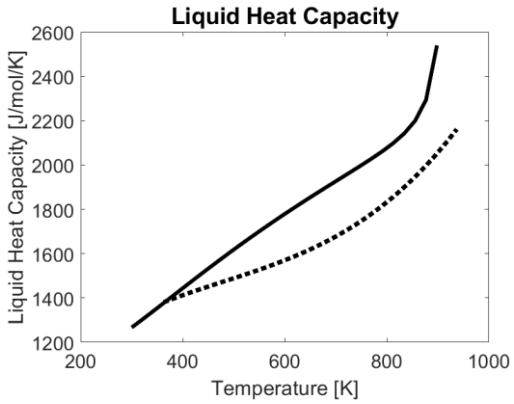
Liquid Heat Capacity
Liquid Heat Capacity [J/mol/K]
Temperature [K]

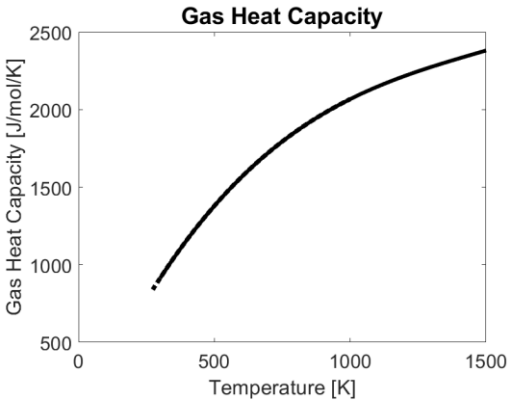
Gas Heat Capacity
Gas Heat Capacity [J/mol/K]
Temperature [K]

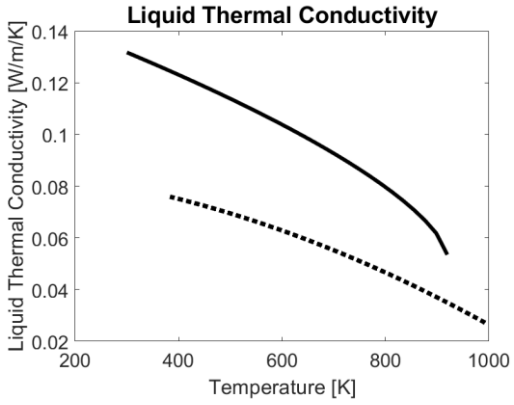
Liquid Thermal Conductivity
Liquid Thermal Conductivity [W/m/K]
Temperature [K]

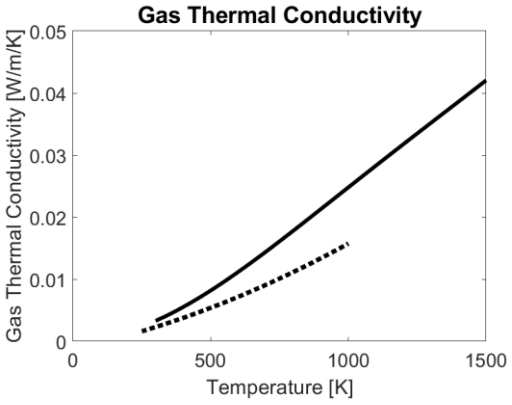
Gas Thermal Conductivity
Gas Thermal Conductivity [W/m/K]
Temperature [K]

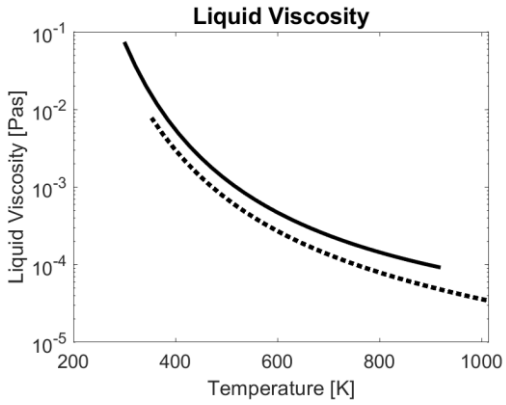
Liquid Viscosity
Liquid Viscosity [Pas]
Temperature [K]

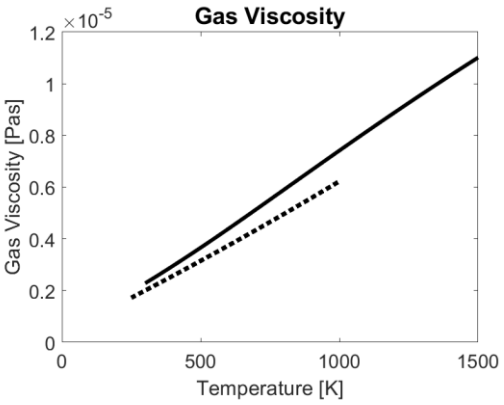
Gas Viscosity
Gas Viscosity [Pas]
Temperature [K]

Pyrene

Property		Predicted	Experimental
T_C	[K]	941.6	936.0
P_c	[bar]	29.3	26.1
T_{NBP}	[K]	662.4	664.6

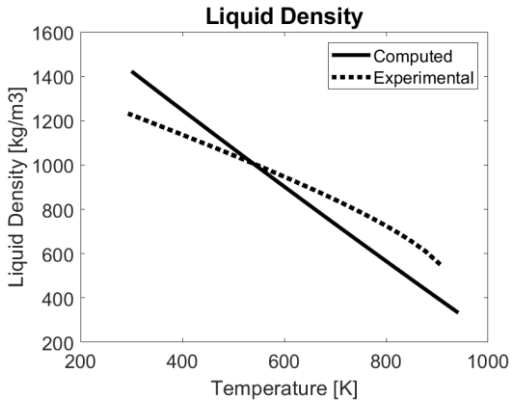

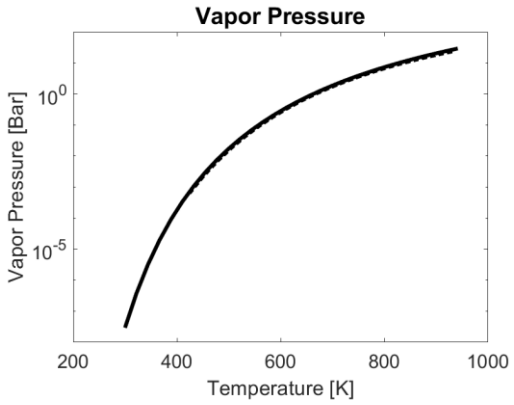

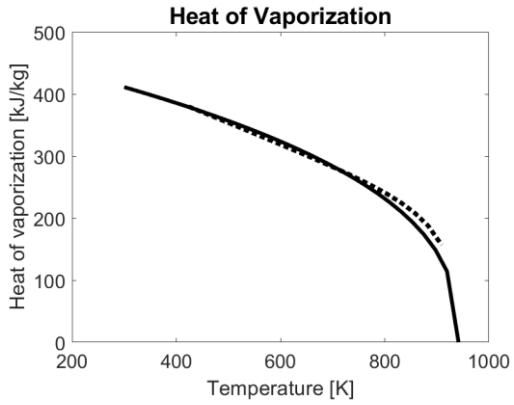

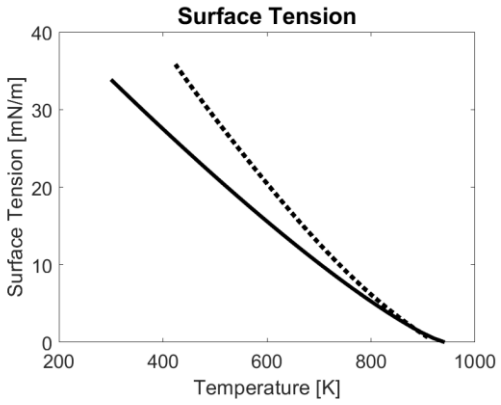

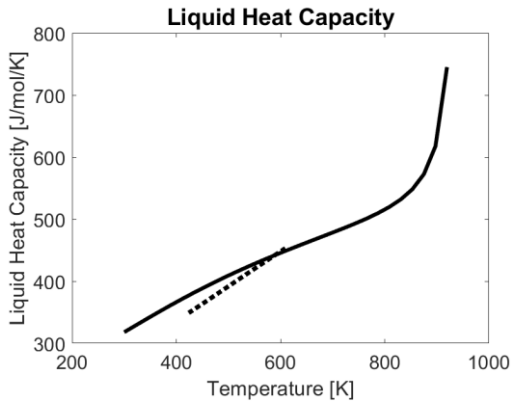

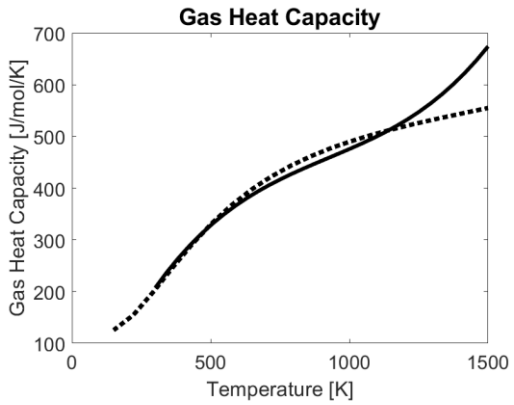

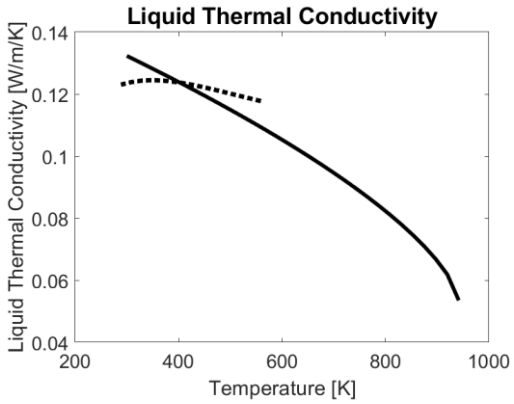
Liquid Thermal Conductivity
Liquid Thermal Conductivity [W/m/K]
0.14
0.12
0.1
0.08
0.06
0.04
200
400
600
800
1000
Temperature [K]

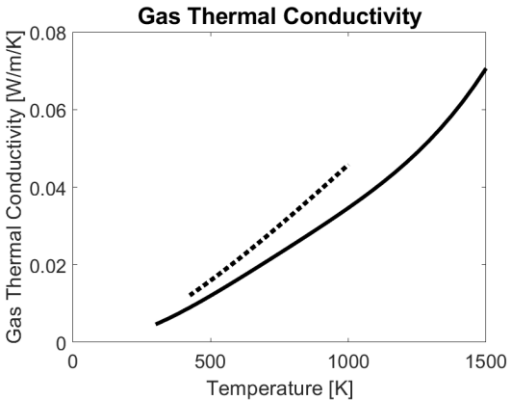
Gas Thermal Conductivity
Gas Thermal Conductivity [W/m/K]
0.08
0.06
0.04
0.02
0
0
500
1000
1500
Temperature [K]

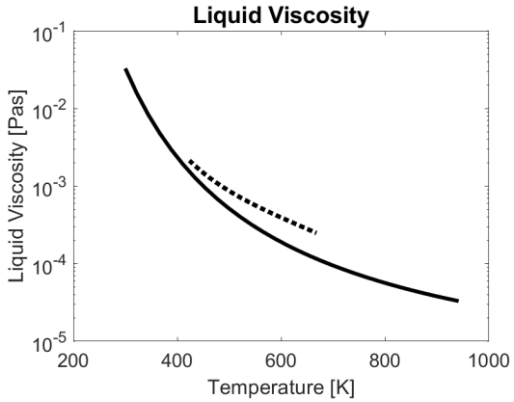
Liquid Viscosity
Liquid Viscosity [Pas]
10-1
10-2
10-3
10-4
10-5
200
400
600
800
1000
Temperature [K]

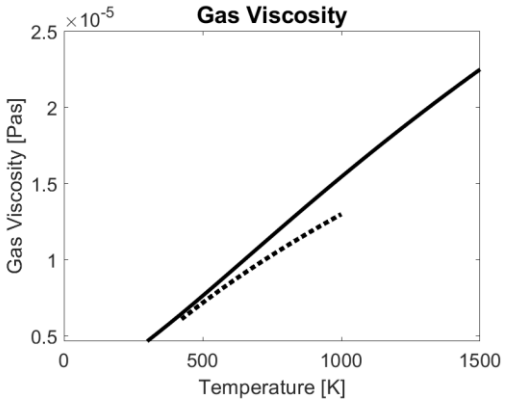
Gas Viscosity
×10-5
Gas Viscosity [Pas]
2.5
2
1.5
1
0.5
0
500
1000
1500
Temperature [K]

Chrysene

Property		Predicted	Experimental
T_C	[K]	961.2	979.0
P_c	[bar]	28.2	23.9
T_{NBP}	[K]	684.0	713.7

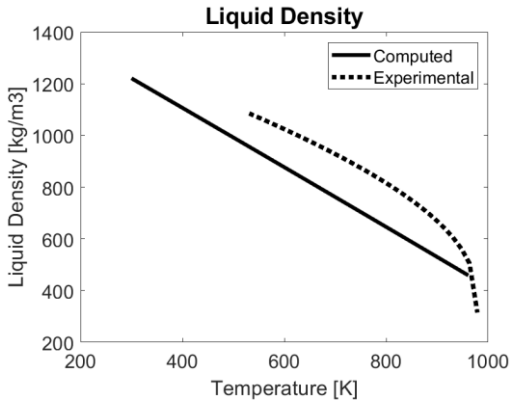

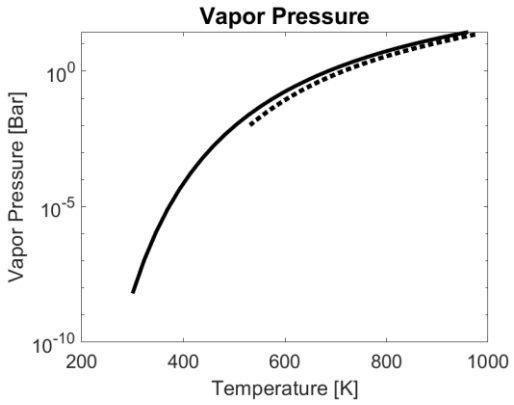

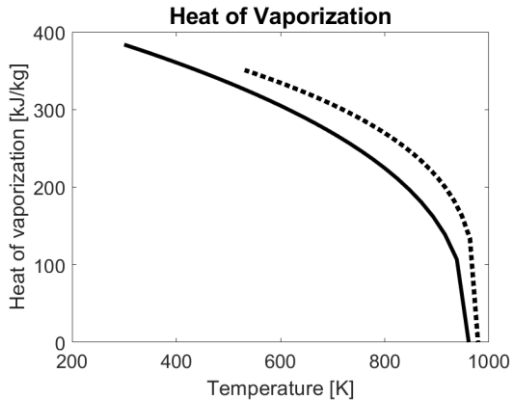

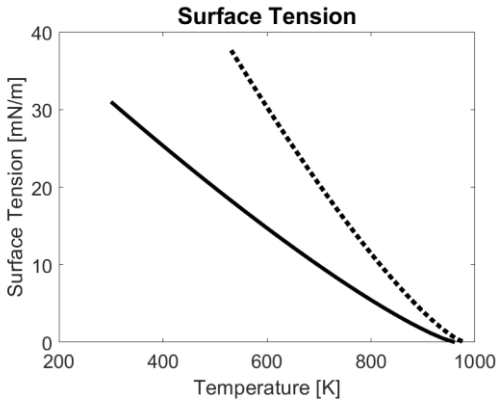

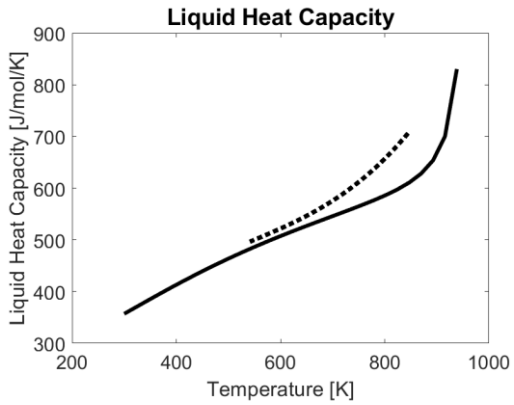

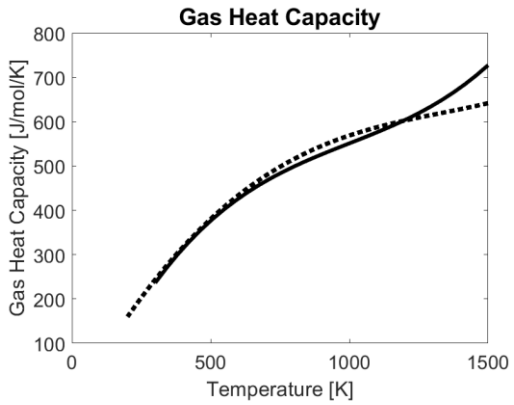

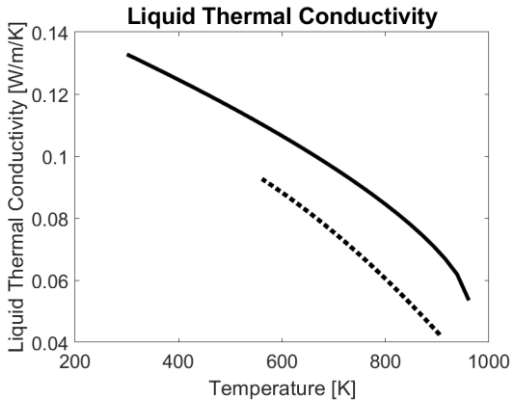
Liquid Thermal Conductivity
Liquid Thermal Conductivity [W/m/K]
0.14
0.12
0.1
0.08
0.06
0.04
200
400
600
800
1000
Temperature [K]

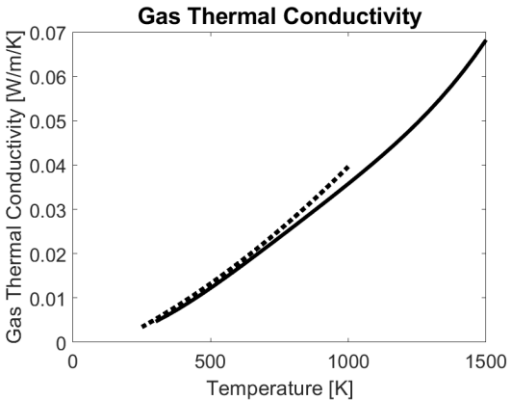
Gas Thermal Conductivity
Gas Thermal Conductivity [W/m/K]
0.07
0.06
0.05
0.04
0.03
0.02
0.01
0
0
500
1000
1500
Temperature [K]

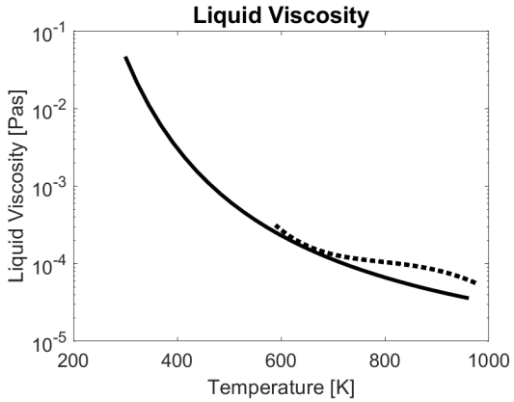
Liquid Viscosity
Liquid Viscosity [Pas]
10-1
10-2
10-3
10-4
10-5
200
400
600
800
1000
Temperature [K]

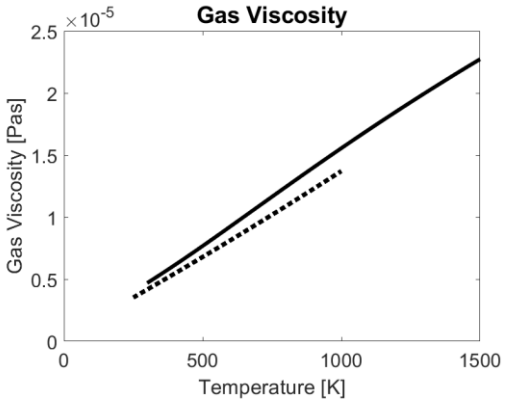
Gas Viscosity
×10-5
Gas Viscosity [Pas]
2.5
2
1.5
1
0.5
0
0
500
1000
1500
Temperature [K]

Squalane

Property		Predicted	Experimental
T_C	[K]	806.1	863.0
P_c	[bar]	6.96	8.68
T_{NBP}	[K]	689.0	717.2

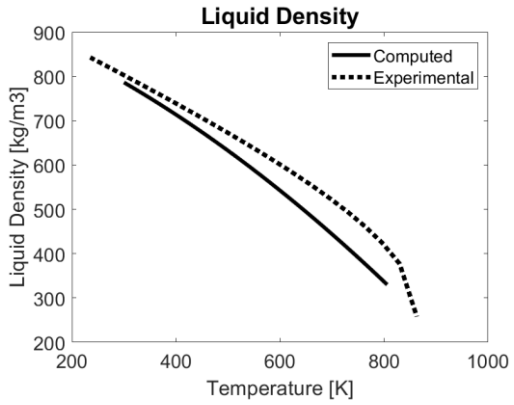

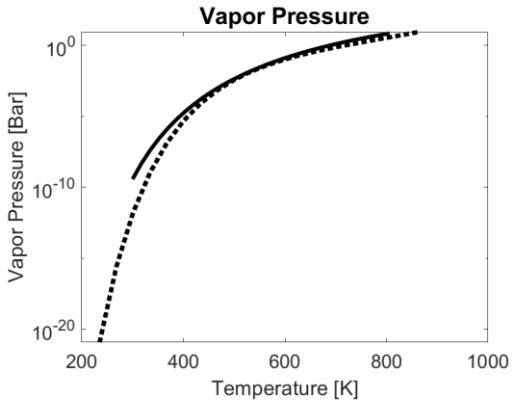

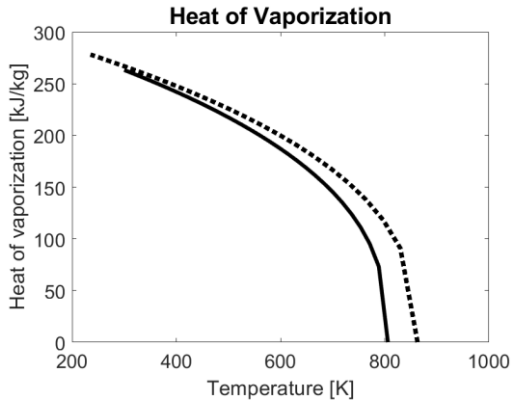

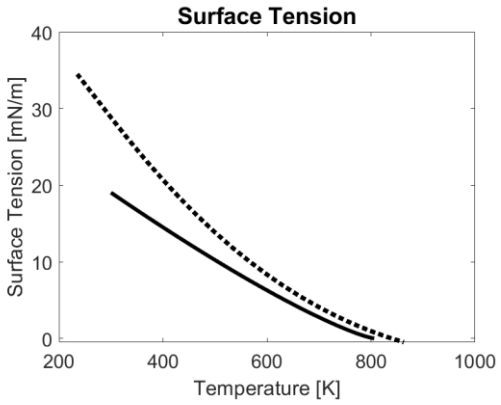

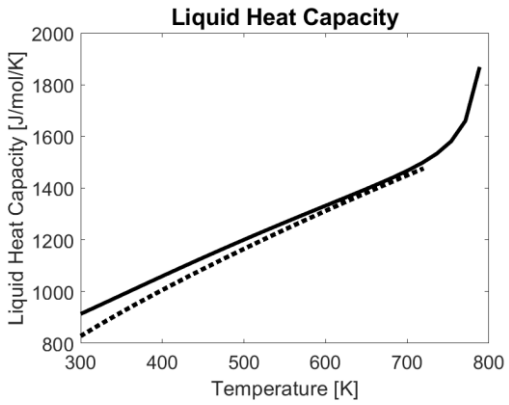

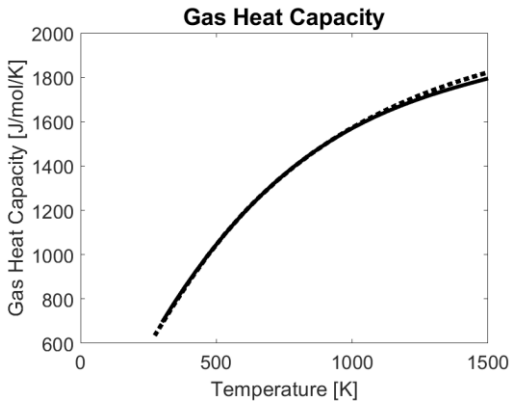

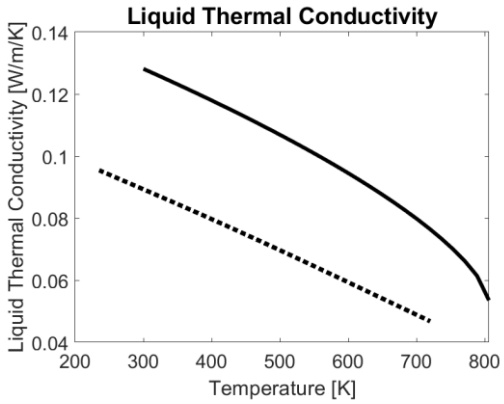
Liquid Thermal Conductivity
Liquid Thermal Conductivity [W/m/K]
0.14
0.12
0.1
0.08
0.06
0.04
200
300
400
500
600
700
800
Temperature [K]

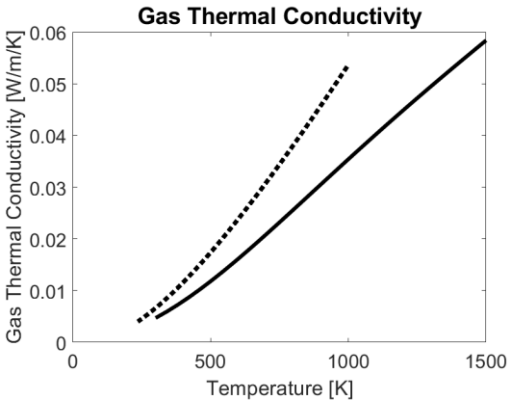
Gas Thermal Conductivity
Gas Thermal Conductivity [W/m/K]
0.06
0.05
0.04
0.03
0.02
0.01
0
0
500
1000
1500
Temperature [K]

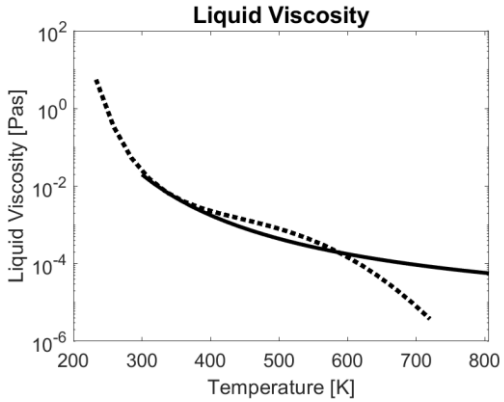
Liquid Viscosity
Liquid Viscosity [Pas]
10^2
10^0
10^-2
10^-4
10^-6
200
300
400
500
600
700
800
Temperature [K]

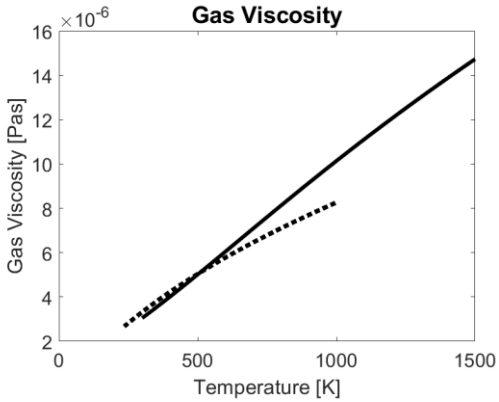
Gas Viscosity
×10^-6
Gas Viscosity [Pas]
16
14
12
10
8
6
4
2
0
500
1000
1500
Temperature [K]

Diphenyl disulfide

Property		Predicted	Experimental
T_C	[K]	876.4	829.8
P_c	[bar]	35.9	35.7
T_{NBP}	[K]	606.7	583.9

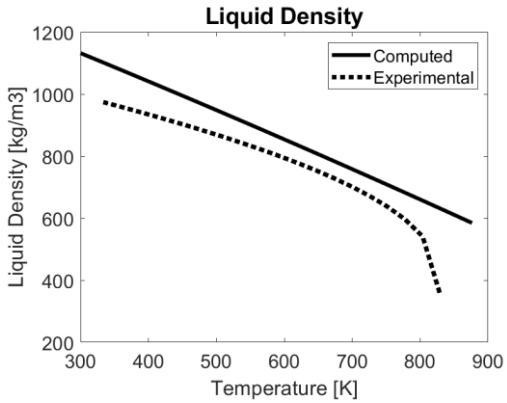

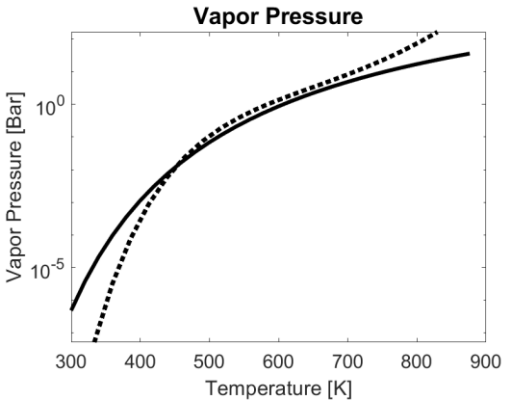

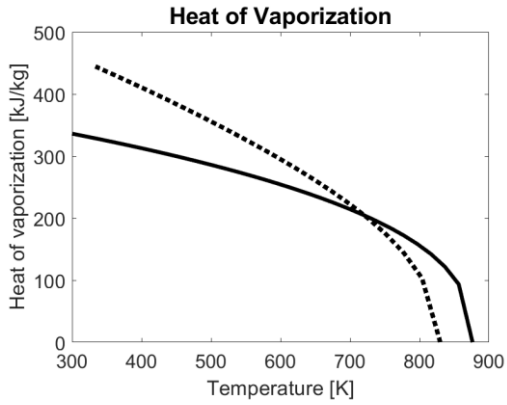

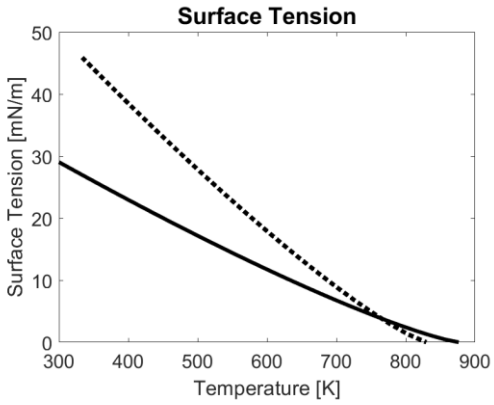

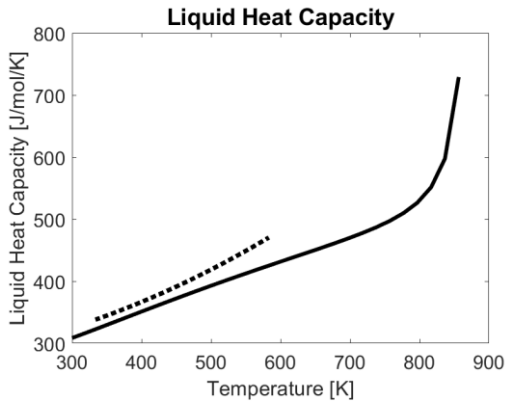

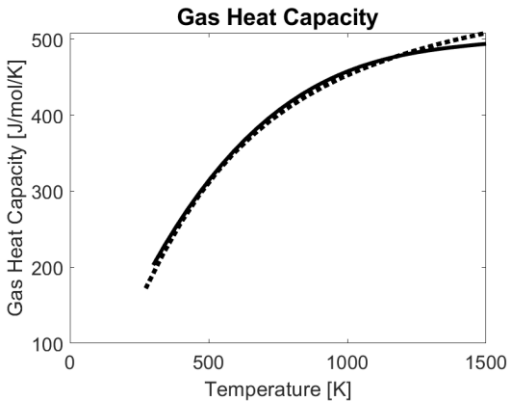

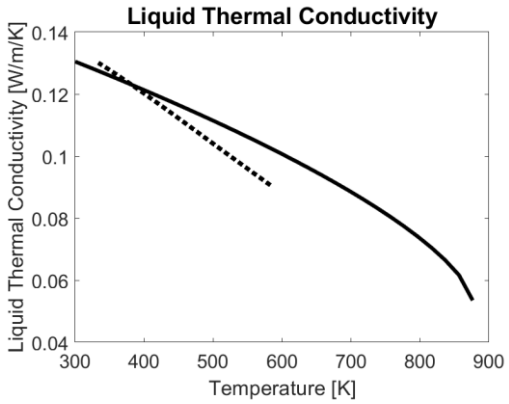
Liquid Thermal Conductivity
Liquid Thermal Conductivity [W/m/K]
0.14
0.12
0.1
0.08
0.06
0.04
300
400
500
600
700
800
900
Temperature [K]

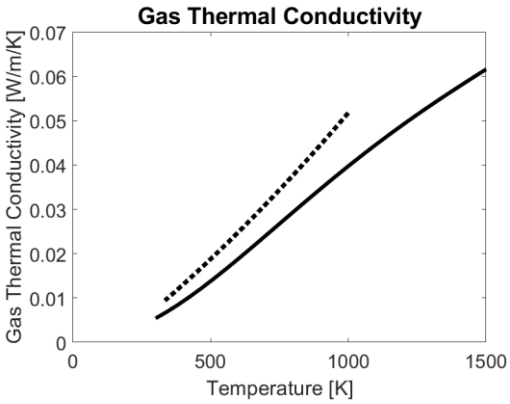
Gas Thermal Conductivity
Gas Thermal Conductivity [W/m/K]
0.07
0.06
0.05
0.04
0.03
0.02
0.01
0
0
500
1000
1500
Temperature [K]

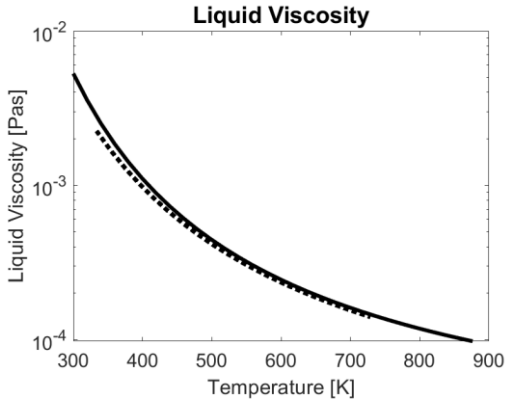
Liquid Viscosity
Liquid Viscosity [Pas]
10-2
10-3
10-4
300
400
500
600
700
800
900
Temperature [K]

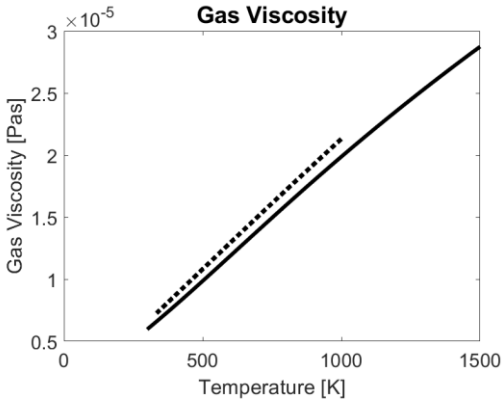
Gas Viscosity
×10-5
Gas Viscosity [Pas]
3
2.5
2
1.5
1
0.5
0
500
1000
1500
Temperature [K]

8.2 Appendix B – Reference species properties

Asph1

Property		
T_C	1338.1	[K]
P_c	6.58	[bar]
T_{NBP}	1181.5	[K]

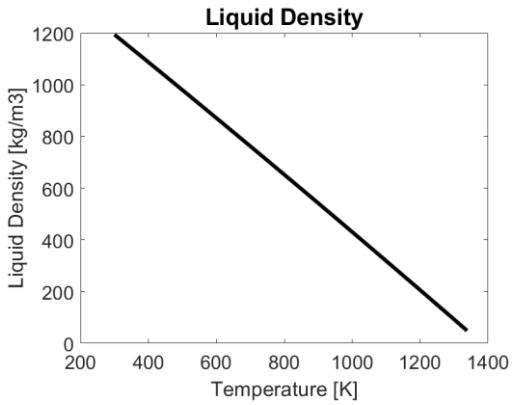

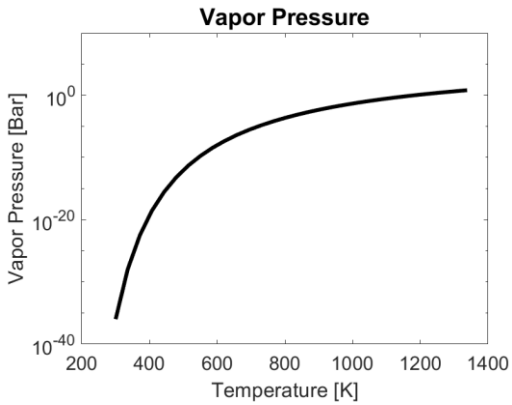

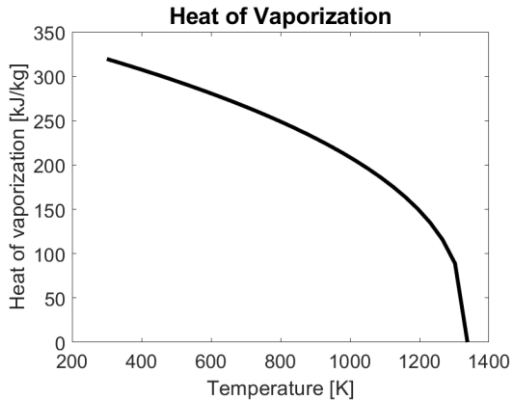

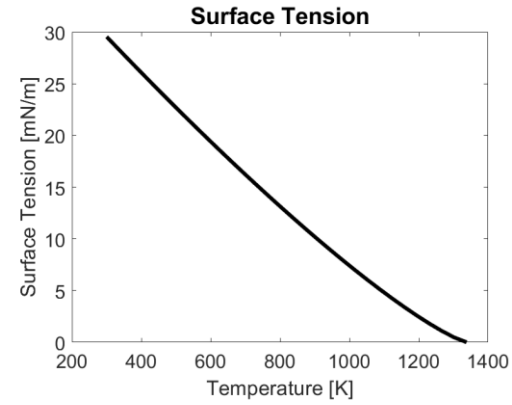

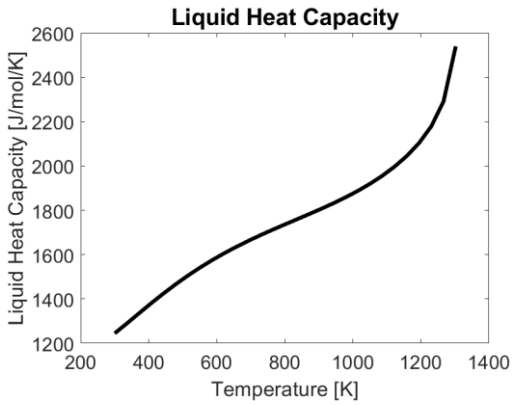

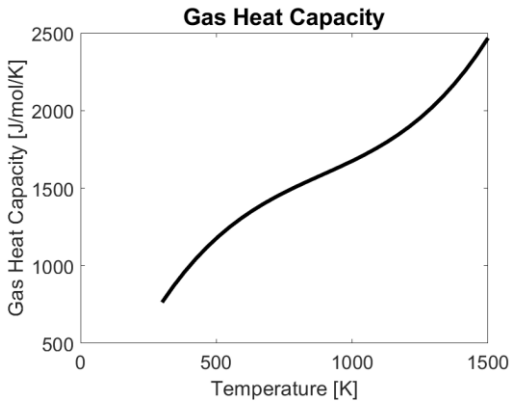

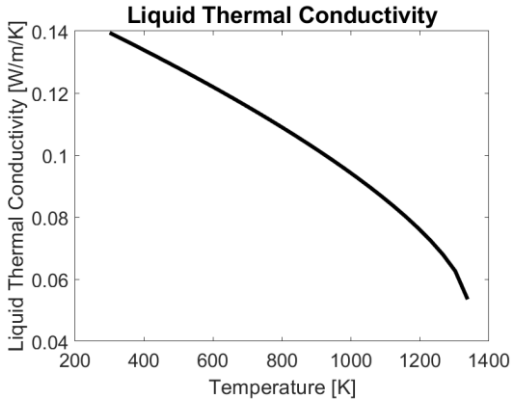
Liquid Thermal Conductivity
Liquid Thermal Conductivity [W/m/K]
0.14
0.12
0.1
0.08
0.06
0.04
200
400
600
800
1000
1200
1400
Temperature [K]

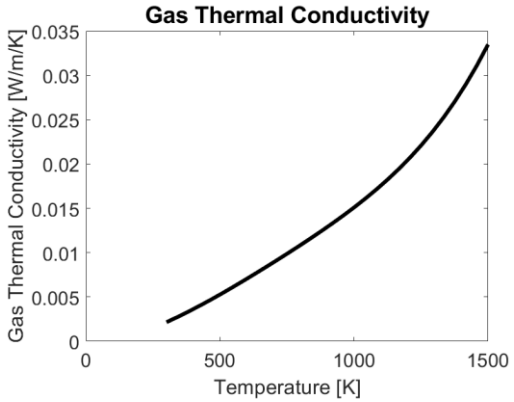
Gas Thermal Conductivity
Gas Thermal Conductivity [W/m/K]
0.035
0.03
0.025
0.02
0.015
0.01
0.005
0
0
500
1000
1500
Temperature [K]

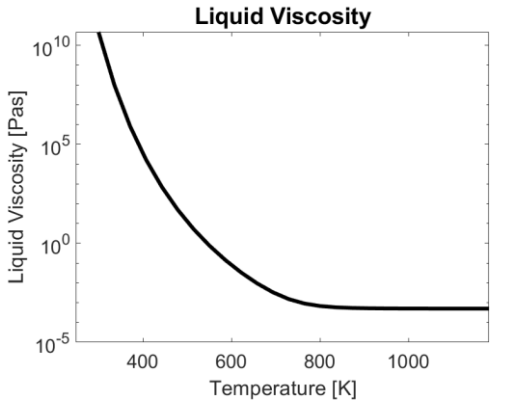
Liquid Viscosity
Liquid Viscosity [Pas]
10^10
10^5
10^0
10^-5
400
600
800
1000
Temperature [K]

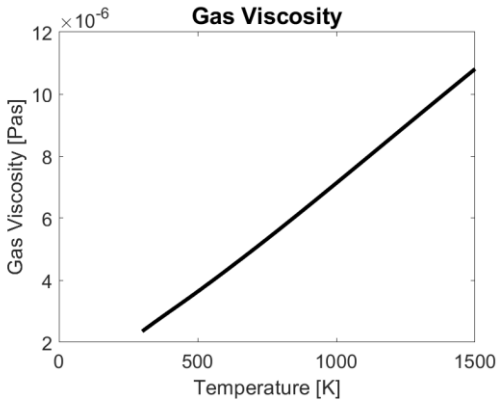
Gas Viscosity
×10^-6
Gas Viscosity [Pas]
12
10
8
6
4
2
0
500
1000
1500
Temperature [K]

Asph2

Property		
T_C	1009.9	[K]
P_c	2.74	[bar]
T_{NBP}	971.7	[K]

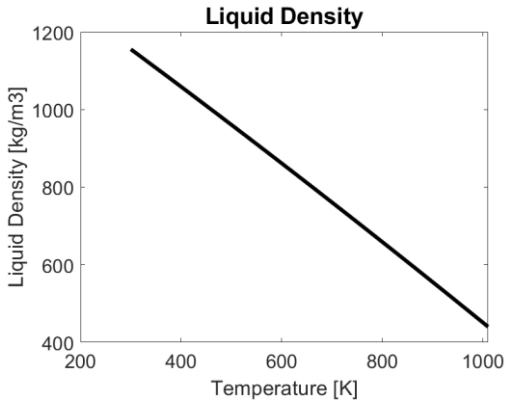

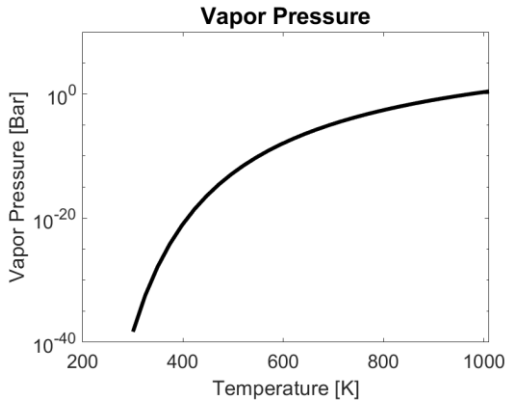

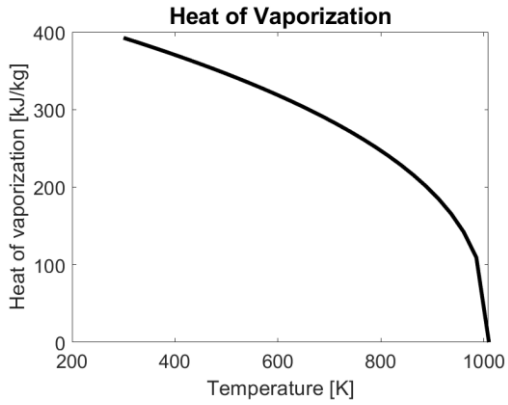

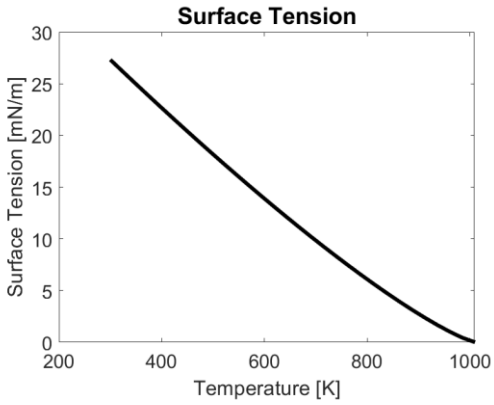

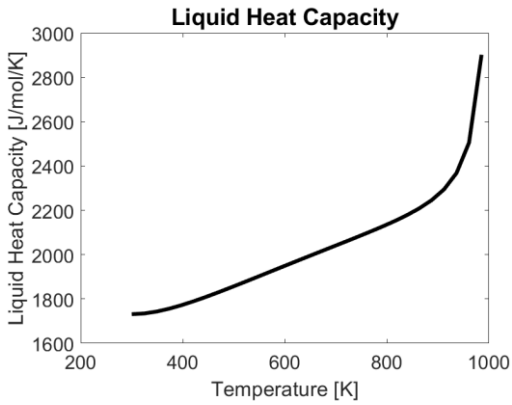

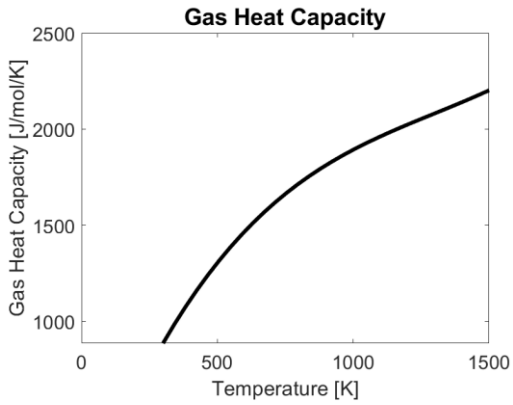

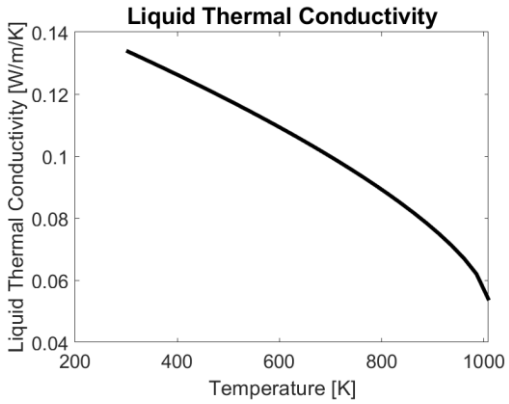
Liquid Thermal Conductivity
Liquid Thermal Conductivity [W/m/K]
0.14
0.12
0.1
0.08
0.06
0.04
200
400
600
800
1000
Temperature [K]

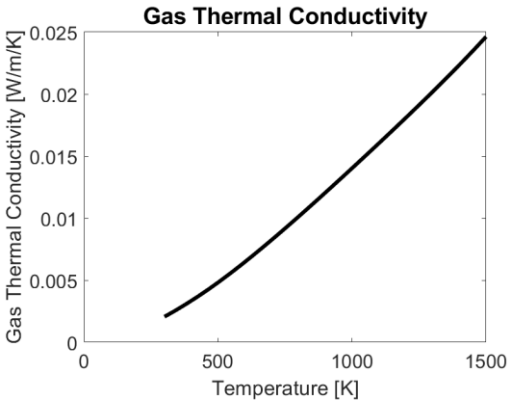
Gas Thermal Conductivity
Gas Thermal Conductivity [W/m/K]
0.025
0.02
0.015
0.01
0.005
0
0
500
1000
1500
Temperature [K]

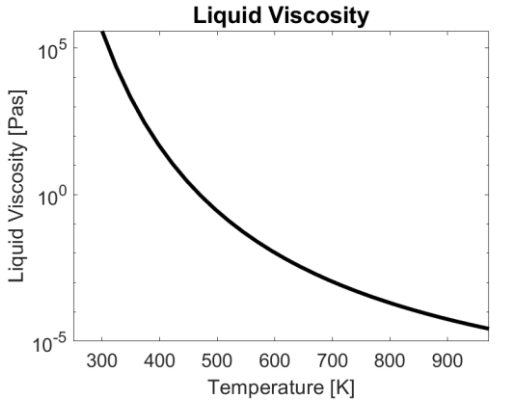
Liquid Viscosity
Liquid Viscosity [Pas]
10^5
10^0
10^-5
300
400
500
600
700
800
900
Temperature [K]

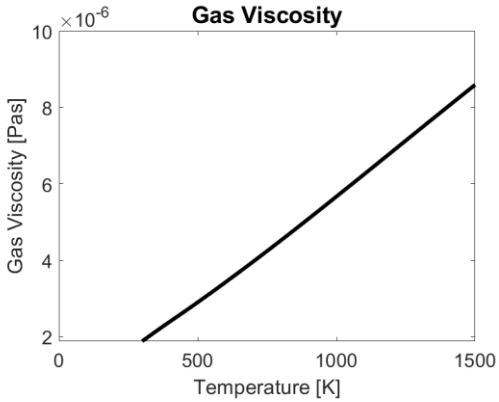
Gas Viscosity
×10^-6
Gas Viscosity [Pas]
10
8
6
4
2
0
500
1000
1500
Temperature [K]

Asph3

Property		
T_C	974.5	[K]
P_c	3.04	[bar]
T_{NBP}	899.7	[K]

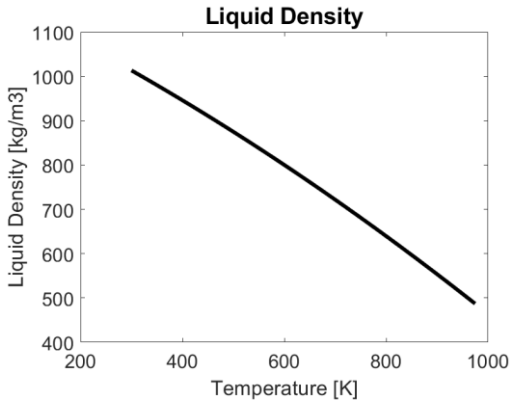

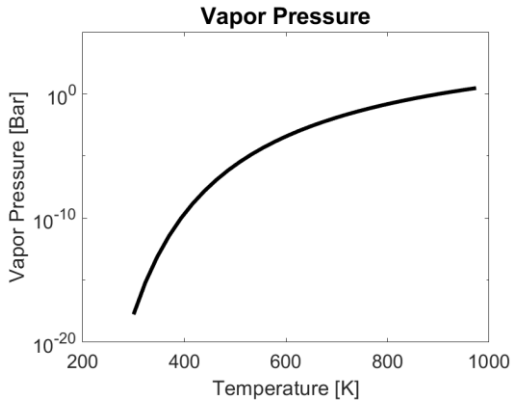

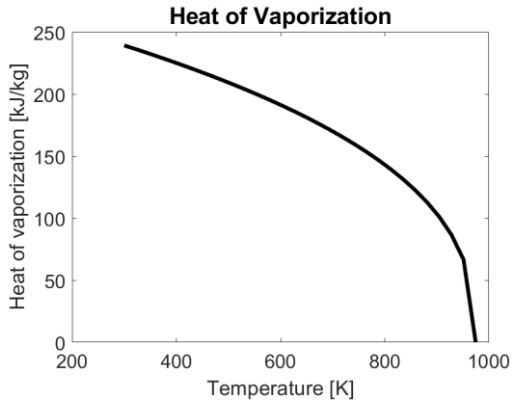

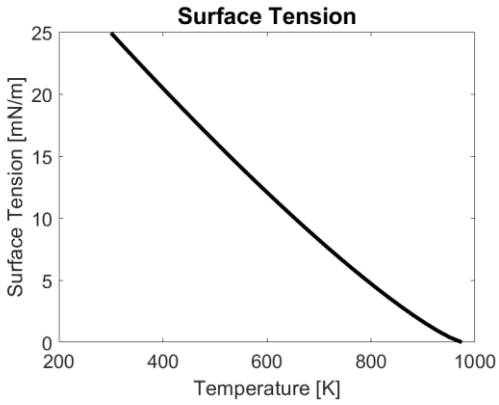

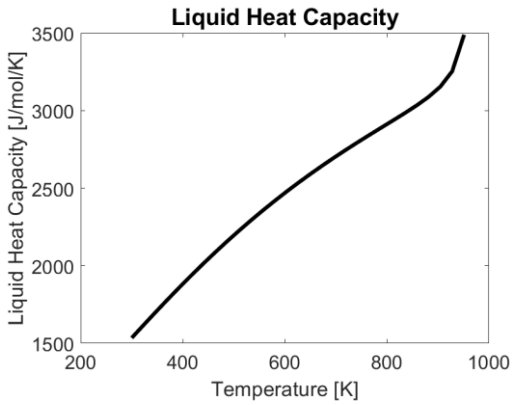

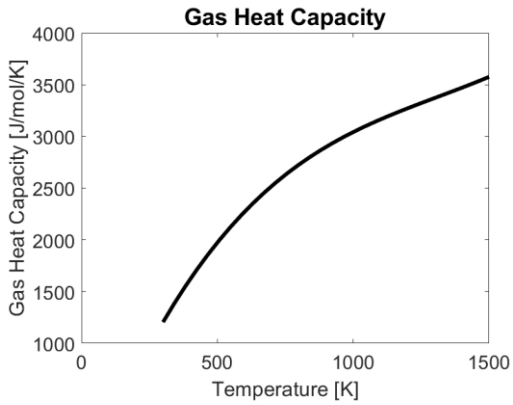

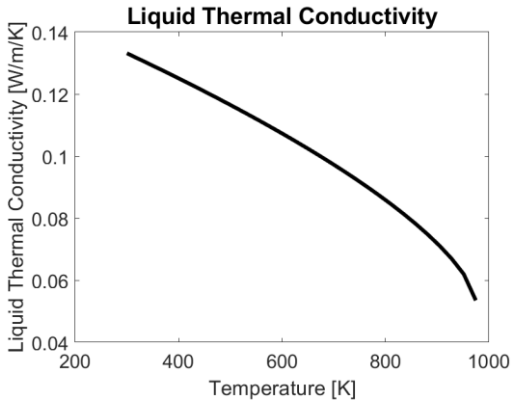
Liquid Thermal Conductivity
Liquid Thermal Conductivity [W/m/K]
0.14
0.12
0.1
0.08
0.06
0.04
200
400
600
800
1000
Temperature [K]

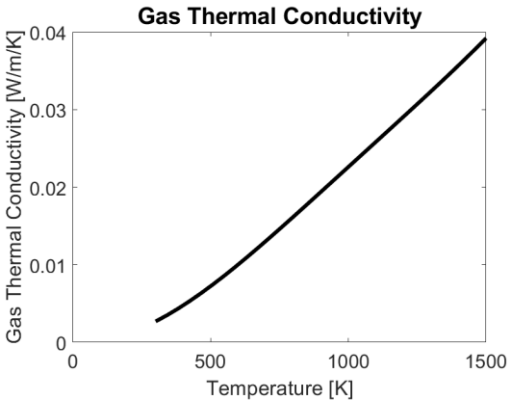
Gas Thermal Conductivity
Gas Thermal Conductivity [W/m/K]
0.04
0.03
0.02
0.01
0
0
500
1000
1500
Temperature [K]

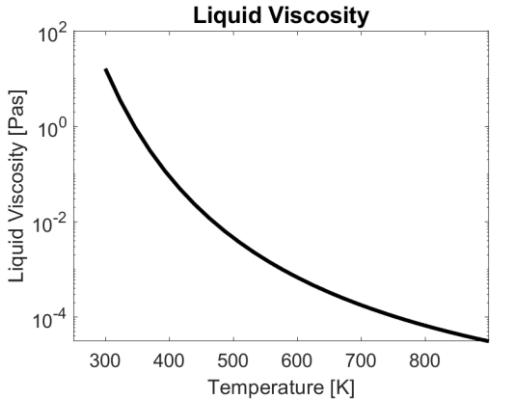
Liquid Viscosity
Liquid Viscosity [Pas]
10^2
10^0
10^-2
10^-4
300
400
500
600
700
800
Temperature [K]

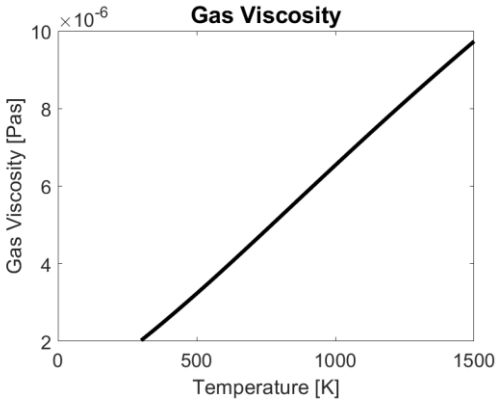
Gas Viscosity
×10^-6
Gas Viscosity [Pas]
10
8
6
4
2
0
500
1000
1500
Temperature [K]

Asph4

Property		
T_C	1082.4	[K]
P_c	2.09	[bar]
T_{NBP}	1035.5	[K]

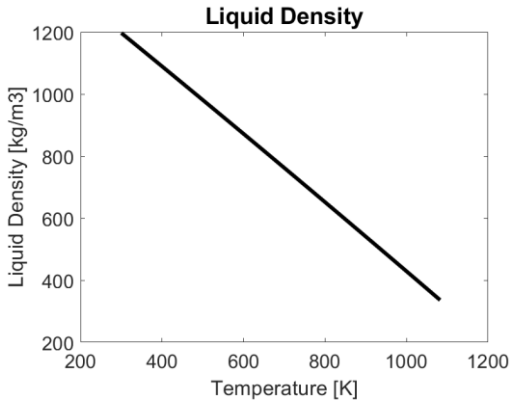

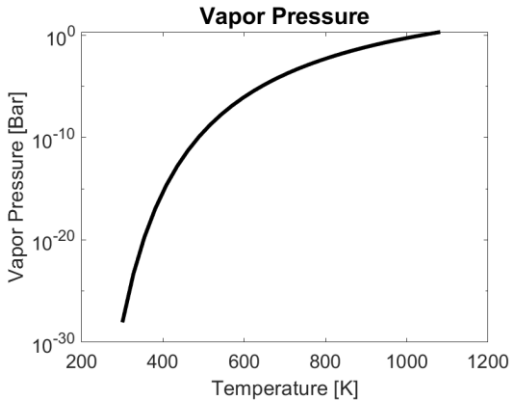

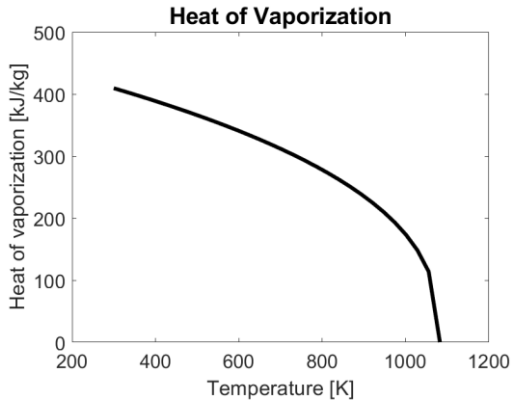

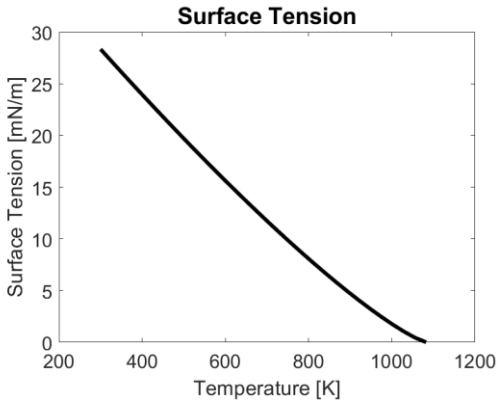

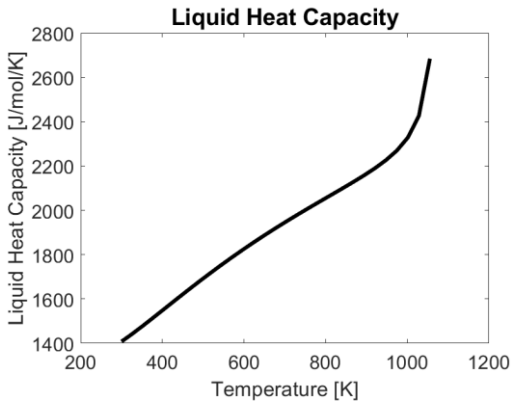

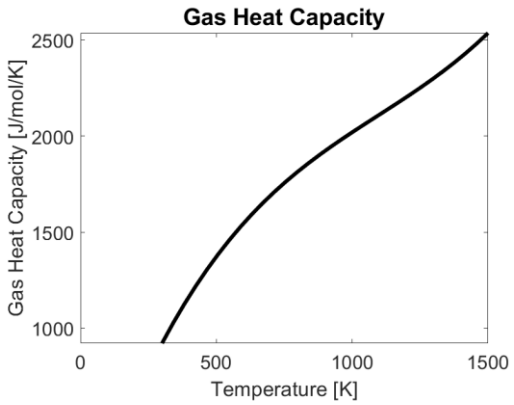

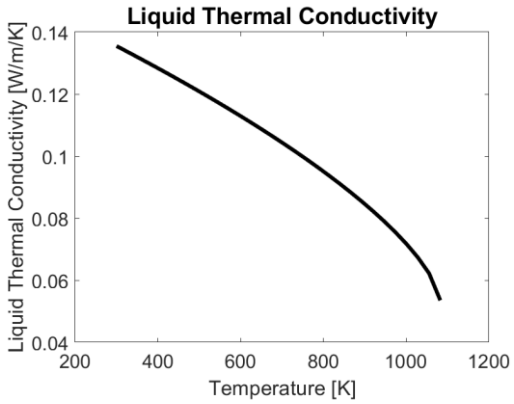
Liquid Thermal Conductivity
Liquid Thermal Conductivity [W/m/K]
0.14
0.12
0.1
0.08
0.06
0.04
200
400
600
800
1000
1200
Temperature [K]

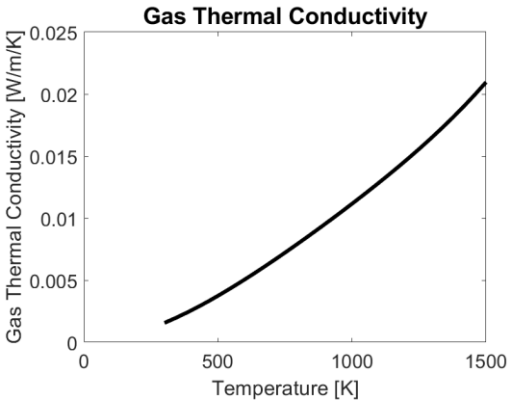
Gas Thermal Conductivity
Gas Thermal Conductivity [W/m/K]
0.025
0.02
0.015
0.01
0.005
0
0
500
1000
1500
Temperature [K]

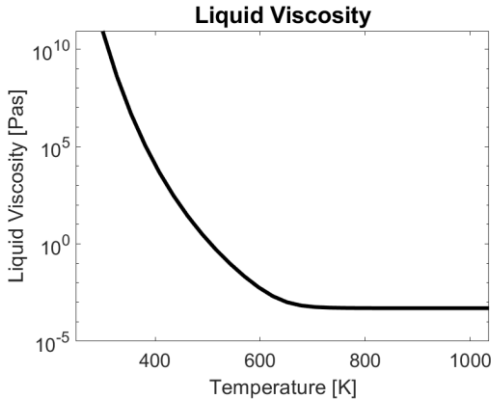
Liquid Viscosity
Liquid Viscosity [Pas]
10^{10}
10^{5}
10^{0}
10^{-5}
400
600
800
1000
Temperature [K]

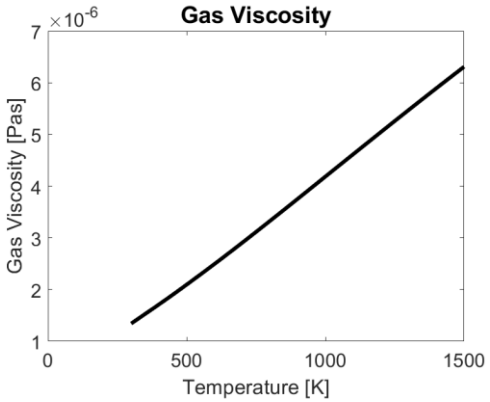
Gas Viscosity
$\times 10^{-6}$
Gas Viscosity [Pas]
7
6
5
4
3
2
1
0
500
1000
1500
Temperature [K]

Asph5

Property		
T_C	1097.2	[K]
P_c	3.21	[bar]
T_{NBP}	1013.9	[K]

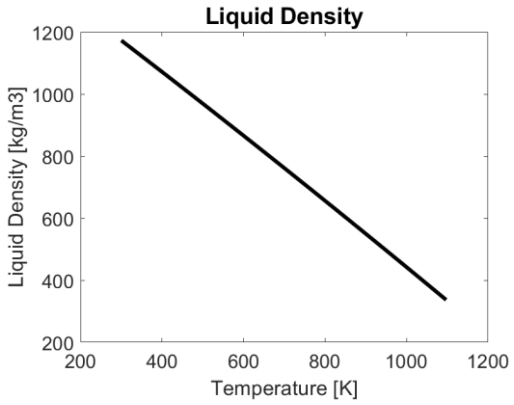

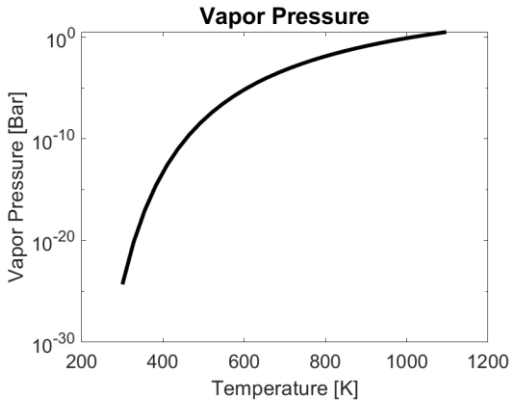

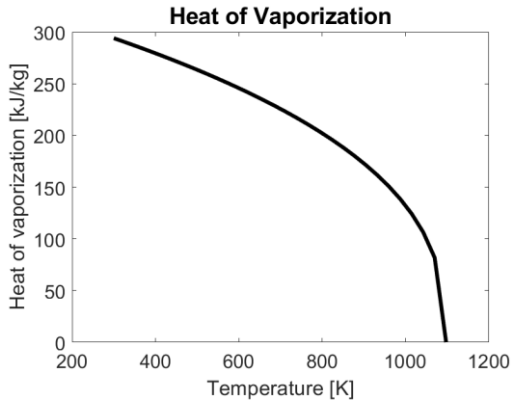

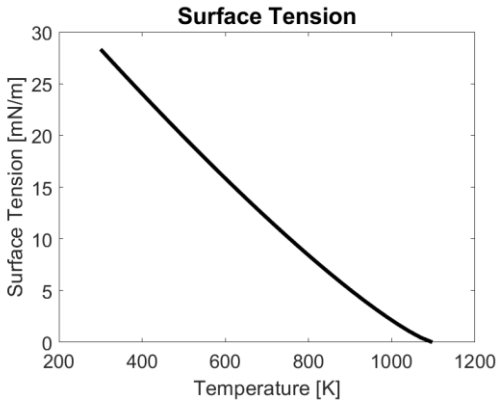

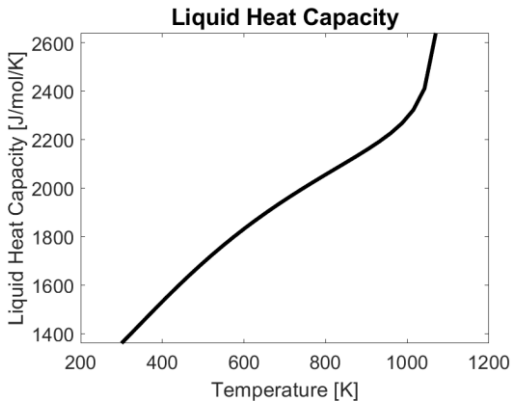

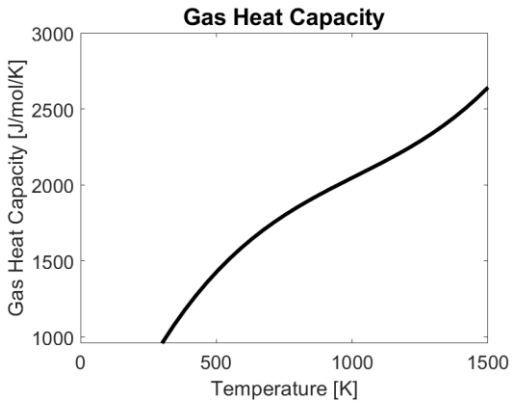

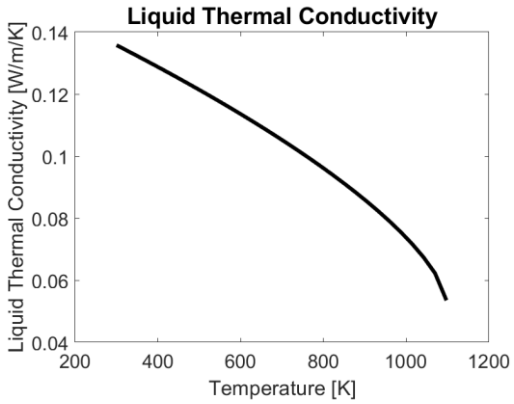
Liquid Thermal Conductivity
Liquid Thermal Conductivity [W/m/K]
0.14
0.12
0.1
0.08
0.06
0.04
200
400
600
800
1000
1200
Temperature [K]

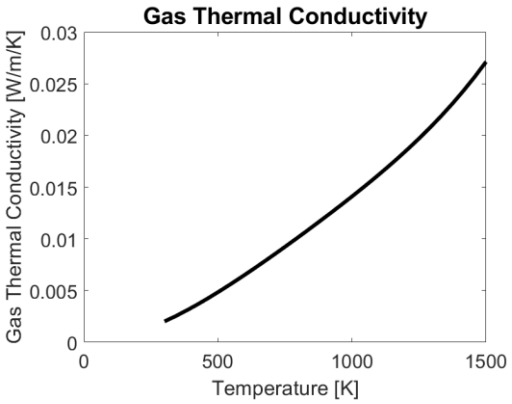
Gas Thermal Conductivity
Gas Thermal Conductivity [W/m/K]
0.03
0.025
0.02
0.015
0.01
0.005
0
0
500
1000
1500
Temperature [K]

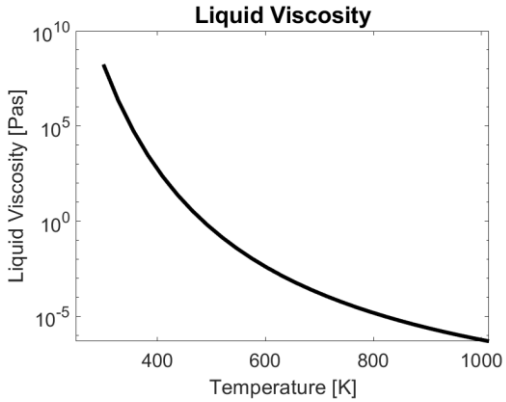
Liquid Viscosity
Liquid Viscosity [Pas]
10^10
10^5
10^0
10^-5
400
600
800
1000
Temperature [K]

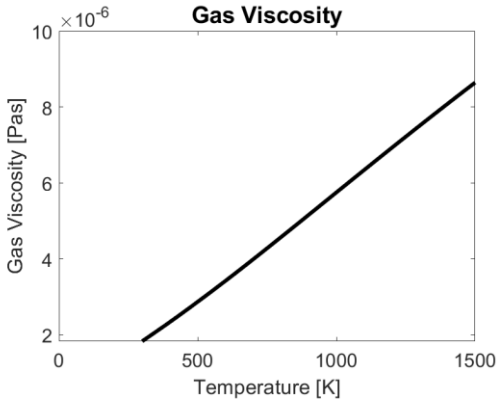
Gas Viscosity
×10^-6
Gas Viscosity [Pas]
10
8
6
4
2
0
500
1000
1500
Temperature [K]

9 Bibliography

[1] bp, "Statistical Review of World Energy," 2020.

[2] F. L. Dryer, "Chemical kinetic and combustion characteristics of transportation fuels," *Proceedings of the Combustion Institute,* vol. 35, pp. 117-144, 2015.

[3] E. Colombo, "LIQUID-PHASE PYROLYSIS OF HEAVY FUEL OILS," 2019.

[4] E. Colleoni, "Kinetic mechanism of heavy fuel oils liquid-phase pyrolysis," 2021.

[5] P. M. Rahimi and T. Gentzis, "The Chemistry Of Bitumen And Heavy Oil Processing," in *Practical Advances in Petroleum Processing,* Devon, Alberta, Canada, National Centre for Upgrading Technology, 2007, pp. 149 -179.

[6] R. H. McKee, F. Reitman, C. Schreiner, R. White, J. H. Charlap, T. P. O'Neil and K. O. Goyak, "The Toxicological Effects of Heavy Fuel Oil Category Substances," *International Journal of Toxicology,* vol. 33, no. 1, pp. 95-109, 2014.

[7] A. G. A. Jameel, Y. Han, O. Brignoli, S. Telalovic, A. M. Elbaz, H. G. Im, W. L. Roberts and S. M. Sarathy, "Heavy fuel oil pyrolysis and combustion: Kinetics and evolved gases investigated by TGA-FTIR," *Journal of Analytical and Applied Pyrolysis,* Vols. 183-195, p. 127, 2017.

[8] D. M. Jewell, E. W. Albaugh, B. E. Davis and R. G. Ruberto, "Ion-exchange, coordination, and adsorption chromatographic separation of heavy-end petroleum distillates," *Industrial & Engineering Chemistry Fundamentals,* vol. 13, no. 3, pp. 278-282, 1974.

[9] D. Stratiev, I. Shishkove, I. Tankov and A. Pavlova, "Challenges in characterization of residual oils. A review," *Journal of Petroleum Science and Engineering,* vol. 178, pp. 227-250, 2019.

[10] T. F. Yen, J. G. Erdman and S. S. Pollack, "Investigations of the Structure of Petroleum Asphaltenes by X-Ray Diffraction," *Analytical Chemisty,* vol. 33, no. 11, pp. 1587-1594, 1961.

[11] M. A. K. Barabat, T. M. Shimy and Y. M. Mostafa, "Mineralogy of Asphaltenes Separated From Crude Oils and Tar Polluttants by X-ray, Polarizing Microscope, IR and NMR Techniques," *Petroleum Science and Technology,* vol. 17, no. 7, pp. 667-691, 1999.

[12] M. A. Bestougeff and R. J. Byramjee, "Chemical Constitution of Asphaltenes," in *Development in Petroleum Science*, 1994, pp. 67-94.

[13] J. G. Speight, "Petroleum Asphaltenes - Part 1: Asphaltenes, Resins and the Structure of Petroleum," *Oil & Gas Science and Technology,* vol. 59, no. 5, pp. 467-477, 2004.

[14] M. M. Boduszynski, "Composition of heavy petroleums. 2. Molecular characterization," *Energy Fuels,* vol. 2, no. 5, pp. 597-613, 1988.

[15] F. M. Vargas and M. Tavakkoli, Asphaltene Deposition: Fundamentals, Prediction, Prevention, and Remediation, CRC Press, 2018.

[16] J. Knotnerus, "Constitution of Aliphatic Bitumen. Characterization of Bitumen by a Combination of Pyrolysis, Hydrogenation, and Gas-Liquid Chromatography," *Ind. Eng. Chem. Prod. Res. Dev.*, vol. 6, no. 1, pp. 43-52, 1967.

[17] R. L. Griffin, W. C. Simpson and T. K. Miles, "Influence of Composition of Paving Asphalt on Viscosity, Viscosity-Temperature Susceptibility, and Durability.," *J. Chem. Eng. Data,* vol. 4, no. 4, pp. 349-354, 1959.

[18] J. A. Koots and J. G. Speight, "Relation of petroleum resins to asphaltenes," *Fuel,* vol. 54, no. 3, pp. 179-184, 1975.

[19] A. E. Pomerantz, Q. Wu, O. C. Mullins and R. N. Zare, "Laser-Based Mass Spectrometric Assessment of Asphaltene Molecular Weight, Molecular

Architecture, and Nanoaggregate Number," *Energy & Fuels*, vol. 29, pp. 2833-2842, 2015.

[20] A. R. Hortal, P. Hurtado, B. Martinez-Haya and O. C. Mullins, "Molecular-weight Distributions of Coal and Petroleum Asphaltenes from Laser Desorption/Ionization Experiments," *Energy & Fuels*, vol. 21, no. 5, pp. 2863-2868, 2007.

[21] S. Badre, C. C. Goncalves, K. Norinaga, G. Gustanov and O. C. Mullins, "Molecular size and weight of asphaltene and asphaltene solubility fractions from coals, crude oils and bitumen," *Fuel*, vol. 85, pp. 1-11, 2006.

[22] B. Schuler, G. Meyer, D. Pena, O. C. Mullins and L. Gross, "Unraveling the Molecule of Asphaltenes by Atomic Force Microscopy," *Journal of the American Chemical Society*, vol. 137, pp. 9870-9876, 2015.

[23] O. C. Mullins, "The Modified Yen Model," *Energy Fuels*, vol. 24, no. 4, pp. 2179-2207, 2010.

[24] D. Xiaodong, Y. Shuanglin, Y. Yuan and L. Huanrong, "N, O, and S, functional groups in residue asphaltene before and after hydrotreating via X-ray technology," *Petroleum Science and Technology*, vol. 35, no. 10, pp. 988-992, 2017.

[25] H. M. Al-Attar, "Determination of the functional groups and the melting point of iraqui asphaltenes," *Petroleum Science and Technology*, vol. 37, no. 4, pp. 486-491, 2019.

[26] T. W. Mojelsky, T. M. Ignasiak, Z. Frakman, D. D. McIntrye, E. M. Lown, D. S. Montgomery and O. P. Strausz, "Structural Features of Alberta Oil Sand Bitumen and Heavy Oil Asphaltenes," *Energy & Fuels*, vol. 6, pp. 83-96, 1992.

[27] E. Ranzi, A. Frassoldati, A. Cuoci and G. Migliavacca, "Chemical Kinetics of Biomass Pyrolysis," *Energy & Fuels*, vol. 22, pp. 4292-4300, 2009.

[28] E. Ranzi, M. dente, A. Goldaniga, G. Bozzano and T. Faravelli, "Lumping procedures in detailed kinetic modeling of gasification, pyrolysis, partial oxidation

and combustion of hydrocarbon mixtures," *Progress in Energy and Combustion Science,* vol. 27, pp. 99-139, 2001.

[29] L. Jiang, A. M. Elbaz, P. Guida, S. M. Al-Noman, I. A. AlGhamdi, S. Saxena and W. L. Roberts, "Cenosphere Formation during Single-Droplet Combustion of Heavy Fuel Oil," *Energy Fuels,* vol. 33, pp. 1570-1581, 2019.

[30] C. L. Yaws, The Yaws Handbook of Physical Properties for Hydrocarbons and Chemicals, Knovel, 2015.

[31] "ChemSep," [Online]. Available: http://www.chemsep.org/. [Accessed 2020].

[32] M. R. Gray, G. Assenheimer, L. Boddez and W. C. McCaffrey, "Melting and Fluid Behavior of Asphaltene Films at 200-500°C," *Energy & Fuels,* vol. 18, pp. 1419-1423, 2004.

[33] L. Constantinou and R. Gani, "New Group Contribution Method for Estimating Properties of Pure Compounds," *AIChE Journal,* vol. 40, no. 10, pp. 1697-1710, 1994.

[34] F. Gharagheizi, A. Eslamimanesh, A. H. Mohammadi and D. Richon, "Use of Artificial Neural Network-Group Contribution Method to Determine Surface Tension of Pure Compounds," *Journal of Chemical & Engineering Data,* vol. 56, no. 5, pp. 2587-2601, 2011.

[35] Y. Nannoolal, J. Rarey and D. Ramjurgernath, "Estimation of pure component properties Part 2. Estimation of critical property data by group contribution," *Fluid Phase Equilibria,* vol. 252, pp. 1-27, 2007.

[36] Y. Nannoolal, J. Rarey, D. Ramjugerth and W. Cordes, "Estimation of pure component properties Part 1. Estimation of the normal boiling point of non-electrolyte organic compounds via group contributions and group interactions," *Fluid Phase Equilibria,* vol. 226, pp. 45-63, 2004.

[37] Y. Nannoolal, J. Rarey and D. Ramjurgernath, "Estimation of pure components properties Part 3. Estimation of the vapor pressure of non-electrolyte organic

compounds via group contributions and group interactions," *Fluid Phase Equilibria,* vol. 269, pp. 117-133, 2008.

[38] Y. Nannoolal, J. Rarey and D. Ramjurgernath, "Estimation of pure component properties. Part 4: Estimation of the saturated liquid viscosity of non-electrolyte organic compounds via group contributions and group interactions," *Fluid Phase Equilibria,* vol. 281, pp. 97-119, 2009.

[39] K. G. Joback and R. C. Reid, "Estimation of Pure-Component Properties from Group-Contributions," *Chemical Engineering Communications,* vol. 57, pp. 233-243, 1987.

[40] M. R. Riazi, Characterization and Properties of Petroleum Fractions, Philadelphia: ASTM, 2005.

[41] N. Gopinathan and D. N. Saraf, "Predict heat of vaporization of crudes and pure components Revised II," *Fluid Phase Equilibria,* vol. 179, pp. 277-284, 2001.

[42] B. I. Lee and M. G. Kesler, "A Generalized Thermodynamic Correlation Based on Three-Parameter Corresponding States," *AlChE Journal,* vol. 21, no. 3, pp. 510-527, 1975.

[43] C. Tsonopoulos, J. L. Heidman and S. Hwang, Thermodynamic and transport properties of coal liquids, 1987.

[44] P. Kontoulis, D. Kazangas, T. P. Doss and L. Kaiktsis, "Development and CFD Validation of an Integrated Model for Marine Heavy Fuel Oil Thermophysical Properties," *Journal of Energy Engineering,* vol. 144, no. 5, 2018.

[45] A. T. Holley, X. Q. You, E. Dames, H. Wang and F. N. Egolfopoulos, "Sensitivity of propagation and extinction of large hydrocarbons flames to fuel diffusion," *Proceeding of the Combustion Institute,* vol. 32, pp. 1157-1163, 2009.

[46] L. Monchick and E. A. Mason, "Transport Properties of Polar Gases," *Journal of Chemical Physics,* vol. 35, pp. 1676-1697, 1961.

[47] T. Liu, M. Long, W. Jiang, D. Chen, S. Yu, H. Duan, J. Sheng and C. Chen, "Variations in the True Density and Sulfur Removal Forms of Petroleum Coke during an Ultrahigh-Temperature Desulfurization Process," *Energy & Fuels,* vol. 31, pp. 7693-7699, 2017.

[48] C. Kuhnt, L. Edwards, M. Lubin and K. Harp, "Influence of Coke Calcining Level on Anode Real Density, LC and Other Properties Using a Constant Baking Cycle," in *Light Metals,* 2019.

[49] U. Im, J. Kim, B. Lee, D. Peck and D. Jung, "Manufacture of high density carbon blocks by self-sintering coke produced via a two-stage heat treatment of coal tar," *Heliyon,* vol. 5, no. 3, pp. 1-17, 2019.

[50] S. Mrozowski, "Mechanical Strength, Thermal Expansion and Structure of Cokes and Carbons," in *Proceedings of the Conference on Carbon*, 1954.

[51] E. W. J. Mardles, “Viscosity of Suspensions and the Einstein Equation,” *Nature,* vol. 145, p. 970, 1940.

[52] B. E. Poling, J. M. Prausnitz and J. P. O'Connell, The Properties of Gases and Liquids, McGraw-Hill, 2001.

[53] S. E. Quinones-Cisneros, C. K. Zeberg-Mikkelsen and E. H. Stenby, "The friction theory (f-theory) for viscosity modeling," *Fluid Phase Equilibria,* vol. 169, pp. 249-276, 2000.

[54] S. Mathur, P. K. Tondon and S. C. Saxena, "Thermal conductivity of binary, ternary and quaternary mixtures of rare gases," *Molecular Physics,* vol. 12, no. 6, pp. 569-579, 1967.

[55] F. Herning and L. Zipperer, “Calculation of the Viscosity of Technical Gas Mixtures from Viscosity of the individual Gases,” *Das Gas- und Wasserfach,* vol. 79, pp. 49-54, 1936.

[56] A. Cuoci, A. Frassoldati, T. Faravelli and E. Ranzi, "OpenSMOKE++: An object-oriented framework for the numerical modeling of reactive systems with detailed

kinetic mechanisms," *Computer Physics Communications,* vol. 192, pp. 237-264, 2015.

[57] A. Cuoci, M. Mehl, G. Buzzi-Ferraris, T. Faravelli, D. Manca and E. Ranzi, "Autoignition and burning rates of fuel droplets under microgravity," *Combustion and Flame,* vol. 143, pp. 211-266, 2005.

[58] J. H. Bae and C. T. Avedisian, "Nonane droplet combustion with and without buoyant convection: Flame structure, burning rate and extinction in air and helium," *Proceedings of the Combustion Institute,* vol. 32, pp. 2231-2238, 2009.

[59] S. Ando, Y. Wu, S. Nakaya and M. Tsue, "Droplet combustion behavior of oxidatively degraded methyl laurate and methyl oleate in microgravity," *Combustion and Flame,* vol. 214, pp. 199-210, 2020.

[60] A. Muelas, P. Remancha and J. Ballester, "Droplet combustion and sooting characteristics of UCO biodiesel, heating oil and their mixtures under realistic conditions," *Combustion and Flame,* vol. 203, pp. 190-203, 2019.

[61] M. Ikegami, G. Xu, K. Ikeds, S. Honma, H. Nagaishi, D. L. Dietrich and Y. Takeshita, "Distinctive combustion stages of single heavy oil droplet under microgravity," *Fuel,* vol. 82, pp. 293-304, 2003.

[62] A. Cuoci, A. E. Saufi, A. Frassoldati, D. L. Dietrich, F. A. Williams and T. Faravelli, "Flame extinction and low-temparature combustion of isolated fuel droplets of n-alkanes," *Proceedings of the Combustion Institute,* vol. 36, pp. 2531-2539, 2017.

[63] J. Wesselingh and R. Krishna, Mass transfer, West Sussex (England): John Wiley & Sons, 1990.

[64] M. A. Siddiqi and K. Lucas, "Correlations for Prediction of Diffusion in Liquids," *The Canadian Journal of Chemical Engineering,* vol. 64, pp. 839-843, 1986.

[65] T. Farouk and F. L. Dryer, "Microgravity droplet combustion: effect of tethering fiber on burning rate and flame structure," *Combustion Theory and Modelling,* vol. 15, no. 4, pp. 487-515, 2010.

[66] P. Somasundaran, Encyclopedia of Surface and Colloid Science, Volume 2, Taylor & Francis, 2006.

[67] G. Buzzi-Ferraris, Scientific C++: Building Numerical Libraries the Object-Oriented Way, New York: Addison Weseley/Longman, 1993.

[68] G. Buzzi-Ferraris and D. Manca, "BzzOde: a new C++ class for the solution of stiff and non-stiff ordinary differential equation systems," *Computers & Chemical Engineering,* vol. 22, no. 11, pp. 1595-1621, 1998.

[69] U. M. Ascher and L. R. Petzold, Computer Methods for Ordinary Differential Equations and Differential-Algebraic Equations, Philadelphia: SIAM, 1998.

[70] S. Beddu, M. M. Zainoodin, Z. C. Muda, D. Mohamad, F. M. Nazri, Z. Itam and S. N. Sadon, "Characteristic Study on Malaysia Power Plant Fly Ash Cenosphere," in *Proceedings of AICCE'19*, 2019.

[71] R. Krishna, "Uphill diffusion in multicomponent mixtures," *The Royal Society of Chemistry,* vol. 10, 2015.

[72] A. Slanciauskas and R. Kalpokaite, "Behavior of heavy fuel oil droplet on hot surface," *International Journal of Heat and Mass Transfer,* vol. 49, pp. 1050-1057, 2006.

[73] R. Villasenor and F. Garcia, "An experimental study of the effects of asphaltenes on heavy fuel oil droplet combustion," *Fuel,* vol. 78, pp. 933-944, 1999.

[74] J. Wang, X. Qiao, D. Ju, C. Sun and T. Wang, "Bubble nucleation, micro-explosion and residue formation in superheated jatropha oil droplet: The phenomena of vapor plume and vapor cloud," *Fuel,* vol. 261, 2020.

[75] V. Garaniya, D. McWilliam, L. GoldSworthy and M. Ghiji, "Extensive Chemical Characterization of a Heavy Fuel Oil".

[76] S. Goncalves, J. Castillo, A. Fernandez and J. Hung, "Absorbance and fluorescence spectroscopy on the aggregation behavior of asphaltene–toluene solutions," *Fuel*, vol. 83, pp. 1823-1828, 2004.

[77] S. S. Betancourt, G. T. Ventura, A. E. Pomerantz, O. VIloria, F. X. Dubost, J. Zuo, G. Monson, D. Bustamante, J. M. Purcell, R. K. Nelson, R. P. Rodgers, C. M. Reddy, A. G. Marshall and O. C. Mullins, "Nanoaggregates of Asphaltenes in a Reservoir Crude Oil and Reservoir Connectivity," *Energy & Fuels*, vol. 23, pp. 1178-1188, 2009.